IMPERIAL COLLEGE LONDON

USE OF MICROWAVES FOR THE DETECTION OF CORROSION UNDER INSULATION

by

Robin Ellis Jones

A thesis submitted to Imperial College London for the degree of

Doctor of Engineering

Department of Mechanical Engineering

Imperial College London

London SW7 2AZ

April 2012

Declaration of originality

The material presented in the thesis "Use of Microwaves for the Detection of Corrosion Under Insulation" was composed and originated entirely as a result of my own independent research under the supervision of Dr. Francesco Simonetti and Prof. Michael Lowe. All published or unpublished material used in this thesis has been given full acknowledgement.

Robin Ellis Jones

18th April 2012

Abstract

Corrosion Under Insulation (CUI) is a widespread problem throughout the oil and gas industry, and is a major cause of pipeline failure. CUI occurs on pipelines fitted with thermal insulation; the insulation itself is protected from the environment by a layer of metallic cladding and sealed to prevent water ingress. This cladding can deteriorate from age or become damaged, allowing the ingress of water into the insulation, which allows corrosion of the external pipe surface to initiate. This corrosion can proceed at an accelerated rate due to the elevated process temperature of the pipe, compromising the integrity of the pipeline. The detection of this type of corrosion is an ongoing problem for the oil and gas industry, as the insulation system conceals the condition of the pipe. Therefore, there is a requirement for a long-range, screening inspection technique which is sensitive to the first ingress of water into the insulation, in order to provide an early warning of areas of a pipeline at risk from CUI.

This thesis describes the development of a new inspection technique which employs guided microwaves as the interrogating signal. Such guided microwaves provide a means of screening the length of a pipeline for wet insulation, by using the structure of a clad and insulated pipeline as a coaxial waveguide to support the propagation of electromagnetic waves. Areas of wet insulation will create impedance discontinuities in the waveguide, causing reflections of the incident microwave signal, allowing the water patches to be detected and located. The performance of such a guided wave inspection system is intrinsically linked to the signal-to-coherent-noise ratio (SCNR) that can be achieved. Therefore, the value of the SCNR that the technique is capable of achieving is of central importance to this thesis. The excitation system is optimised to maximise the SCNR, whilst the effect of typical pipeline features such as bends, pipe supports and the various types of insulation which can be used, are studied to quantify the effect on the SCNR.

A wide variety of methods are employed throughout the development of the guided microwave technique described in this thesis. Theoretical methods are employed in

the initial stages to enable the development of a model to describe electromagnetic wave propagation in the large coaxial waveguides formed by pipelines. Numerical simulation techniques are employed when there are too many parameters to study for experimentation to be a viable option, and to study complex problems for which no analytical solution exists. Experiments are conducted in the laboratory using a model setup which employs metallic ducting to represent an insulated pipeline. These experiments are performed to demonstrate the practical feasibility of the technique, and to study pipeline features in a controlled environment. Finally, experiments are performed in the field on a section of real industrial pipeline, in order to validate the accuracy of the model experimental setup in representing conditions which exist on real pipelines.

The main findings of the thesis are that it is possible to excite a guided microwave signal in a large coaxial waveguide with a high SCNR. Experiments revealed that the technique is highly sensitive to the presence of water in the waveguide. Measurements of the effect of different types of insulation demonstrated that rockwool causes a very low attenuation of the microwave signal, while polyurethane foam insulation has a slightly higher attenuation coefficient. An investigation into the effect of bends determined that, whilst significant mode conversion occurs at a bend, the transmission coefficient of the TEM mode is high for typical bend angles and bend radii in small diameter pipes. The behaviour of the signal at a typical pipe support was also examined; the reflection from the support was minimal, whilst the transmission beyond the support remained relatively high. Whilst there is still further work to be done before this technique can be applied in the field, the major aspects of practical implementation that could affect the technique have been investigated here, and the results consistently indicate the feasibility of the technique for long-range screening of insulated pipelines for water.

Acknowledgements

There are many people I would like to thank for their contribution to this thesis. I am very grateful to Francesco Simonetti for his flawless supervision and insightful guidance, which, not only taught me so much, but made the whole process immensely enjoyable. My gratitude also goes to Mike Lowe and Ian Bradley, for their invaluable contributions at every stage of this project, and for their help in making things happen.

I would like to thank Chris Scruby for his wise counsel, and for offering me the EngD opportunity in the first place. I would like to express my appreciation of the accomplishment of Peter Cawley, Mike Lowe, and Fred Cegla in making the NDT research group such a stimulating and enjoyable environment within which to conduct research. I must also thank everyone who has ever helped me move awkward pieces of ducting around for my experiments: I think this must be almost everyone to have stepped into the lab over the past few years! My gratitude also goes to David Tomlin and Phil Wilson for their time and expertise in machining.

At BP, I would like to thank Simon Webster, Tom Knox, Danny Keck and Ian Bradley for their insights and suggestions at various stages of the project's development. I am also grateful to BP for their financial support of this project, in particular, investing in the experimental hardware. I would also like to acknowledge the financial support of EPSRC, through the Centre for Doctoral Training in Non-Destructive Evaluation.

On a less industrious note, I would like to thank Johnny, Dom, and Joe for their friendship and their belaying, and an excellent time exploring the Indian Himalayas; my compatriots in the 2007 EngD cohort: Sam, Kit, Gabriel, Keith, Chris, and Christiaan, for making our courses so enjoyable; and my colleagues in the NDT lab at Imperial, for countless intriguing discussions and good times at the conferences in the USA.

I would like to express my deepest gratitude to my family: my mum for being so

willing to listen to me talk about my work in gruesome detail; my dad for all of his invaluable solutions to practical problems, which were invariably spot-on; and Chris and Hannah for introducing me to my wonderful nephews Riley and Henry. Finally, I would like to thank Delphine for her unwavering support and generosity of spirit.

Contents

List of Figures

List of Tables

List of Symbols

α	Attenuation coefficient
$\bar{\beta}$	Phase constant normalised to that of vacuum
$\bar{F}$	Average of two cutoff frequencies
β	Phase constant
ΔF	Difference between two cutoff frequencies
δ	Skin depth
ϵ	Permittivity
ϵ_0	Vacuum permittivity
ϵ_∞	Infinite frequency relative permittivity
ϵ_r	Relative permittivity
ϵ_r'	Real part of permittivity
ϵ_r''	Imaginary part of permittivity
ϵ_s	Static relative permittivity
Γ	Reflection coefficient
γ	Ratio of inner and outer conductors of coaxial waveguide, a/b
κ	Thermal conductivity

λ	Wavelength
λ_0	Wavelength in vacuum
λ_m	Centre wavelength
$\lambda_r, \lambda_\theta$	Cylindrical components of wavelength
λ_{wg}	Wavelength inside a waveguide
μ_0	Vacuum permeability
μ_r	Relative permeability
ν_g	Group velocity
ν_p	Phase velocity
ω	Angular frequency
ϕ	Angular extent of a bend
ϕ_c	Bend angle of maximum mode conversion in cylindrical waveguide
ρ	Electrical resistivity
σ	Electrical conductivity
τ	Relaxation time of a polar molecule
$\mathbf{B}$	Magnetic flux density
$\mathbf{D}$	Electric flux density
$\mathbf{E}$	Electric field
$\mathbf{H}$	Magnetic field
$\mathbf{J}$	Conduction current density
$\mathbf{k}$	Wavenumber vector
ξ	Solution to Equation (3.3) or (3.4) for a mode (p, q)

a	Radius of outer conductor of coaxial waveguide
A_1, A_2	Amplitudes used to calculate attenuation coefficient
b	Radius of inner conductor of coaxial waveguide
c	Speed of light in a dielectric medium
c_0	Speed of light in vacuum
d	Annular distance of coaxial waveguide, $a - b$
f	Frequency
f_c	Cutoff frequency
f_m	Centre frequency
$F_{p,q}$	Cutoff frequency of the $T_{p,q}$ mode
h	Height of rectangular waveguide
j	Imaginary unit, $\sqrt{-1}$
J_p	Bessel function of first kind of order p
J'_p	Prime notation denotes differentiation of the Bessel function
k	Wavenumber
k_r, k_θ	Cylindrical components of wavenumber vector
k_x, k_y	Cartesian components of wavenumber vector
l	Length of coaxial waveguide
l_1, l_2	Lengths of coaxial waveguides used in simulations
n	Index of refraction
p	Modal order integer in x direction for rectangular waveguides, and in θ direction for coaxial waveguides

Q	Free charge density
q	Modal order integer in y direction for rectangular waveguides, and in r direction for coaxial waveguides
R	Radius of curvature of a bend
r, θ, z	Cylindrical coordinates
s	Average radius of coaxial waveguide, $(a + b)/2$
t	Time
$T_{p,q}$	A mode of the coaxial waveguide
w	Width of rectangular waveguide
x, y, z	Cartesian coordinates
X_p	A combination of Bessel functions, according to Equation (3.9)
Y_p	Bessel function of second kind of order p
Z_0	Characteristic impedance
Z_p	A combination of Bessel functions, according to Equation (3.12)

List of Abbreviations

CUI Corrosion Under Insulation

FIT Finite Integration Technique

IMR Impedance Matching Ratio

MWS Microwave Studio

NDE Non-destructive Evaluation

NPS Nominal Pipe Size

PEC Perfect Electrical Conductor

PTI Profile Technologies Incorporated

PUF Polyurethane Foam

QNDE Quantitative Non-destructive Evaluation, Review of progress in

SCC Stress Corrosion Cracking

SCNR Signal-to-Coherent-Noise Ratio

SMA Sub-Miniature version A

TE Transverse Electric

TEM Transverse Electromagnetic

TM Transverse Magnetic

Chapter 1

Introduction

At 12.30pm on Monday the 29th September 2008 a high-pressure gas pipeline ruptured at the Prudhoe Bay oil field in Alaska [1]. The pipeline burst, propelling two sections of pipe, 14 feet and 28 feet in length, 900 feet across the tundra [2, 3], as shown in Figure 1.1. The gas line was isolated and depressurised after about an hour, however, this allowed natural gas to be released into the atmosphere, which could have led to an explosion. No injuries to personnel were sustained in this incident, nor was there any spillage or fire or explosion, however, the potential for any of these to have occurred was great. The requirement to shut down production on a sector of the Prudhoe Bay oil field led to an economic impact in terms of lost production, in addition to the fact that a release of gas into the atmosphere can incur a hefty fine from the regulating bodies [1]. The cause of this failure was Corrosion Under Insulation (CUI).

Corrosion under insulation is a major problem throughout the oil and gas industry, but it is not only the petrochemical industry which is affected; CUI is also a problem for the power and manufacturing industries, but can occur wherever pipelines are fitted with thermal insulation. It is a problem which is not isolated to a particular geographical location; it occurs in facilities and on pipelines all over the world. This form of corrosion occurs on steel pipelines which have been fitted with thermal insulation, and as such it is inherently very difficult to detect, as the presence of corrosion

(a) The ruptured gas line

(b) One of the separated sections

Figure 1.1: On the 29th September 2008 a high pressure gas pipeline ruptured at Prudhoe Bay, causing a release of natural gas into the atmosphere, and launching two sections of pipe into the air to land 900 feet away from the incident [3].

is obscured by the insulation system. Because the corrosion develops undetected, it can lead to serious pipeline failures, which have several adverse consequences including the risk to the safety of site personnel, damage to the environment, and an economic impact in terms of the cost of cleaning up any spillage and lost production. Therefore, a significant proportion of the large maintenance budgets allocated by operating companies are spent on the inspection for, and mitigation of, CUI [4, 5].

1.1 Mechanism of Corrosion Under Insulation

Pipelines and vessels are thermally insulated primarily for two reasons. The first of which is for process reasons, specifically, to maintain the hot temperatures present in hot processes, and to maintain the cold temperatures of cold processes. The second reason is for personnel protection; site personnel can easily burn themselves on accidental contact with hot process pipework. The thermal insulation is protected from the environment by a layer of metallic weatherproofing cladding, which is intended to keep the insulation dry, as insulation loses much of its effectiveness once it becomes wet. The cladding material is usually galvanised steel, aluminium, aluminised steel or stainless steel, in sheet form with a thickness in the range of 0.5

to 1.25 mm [5, p.120]. Joints between the different layers and sections of cladding are typically sealed with mastic or silicon based sealants in order to prevent water ingress. However, these sealants degrade over time, through exposure to the environment, leading to the formation of a path for water ingress into the insulation. A section of wet insulation creates an area on the steel pipe's surface which is in contact with water and a plentiful supply of oxygen, both of which are required for corrosion to initiate. The corrosion rate of steel, assuming the presence of water and oxygen, is primarily controlled by temperature [4, p.174], with increasing temperatures causing increased rates of corrosion. The elevated temperature of the insulated pipe creates an environment in which corrosion can proceed at a rapid rate once water comes into contact with the steel of the pipe, with loss of wall thickness occurring at a rate ranging from 0.3 to 2.2 mm per year [6–8].

Different types of corrosion occur depending on the material of the pipe. On carbon steel (in which the primary alloying ingredient is carbon) and low-alloy steels (with a chromium alloying percentage of less than 11 % [5, p.33]) the problem is corrosion of the external surface of the pipe, leading to a loss in wall thickness and pitting. On austenitic stainless steel pipes, conventional corrosion is no longer the problem, rather it is chloride external Stress Corrosion Cracking, referred to as SCC. If chloride ions are present in the water which is in contact with the austenitic stainless steel pipe's surface, then SCC may initiate, causing a fine network of transgranular cracking to manifest, both on the surface and in the bulk of the material [4, p.175]. Chloride ions can be introduced into the insulation due to the testing of fire deluge systems that use seawater, or due to being located in a coastal or marine environment, or through the leaching of contaminants from the insulation materials themselves. In addition to the requirements for water and chloride ions, SCC requires tensile stresses to exist in the component, therefore if the tensile stress can be eliminated then SCC can be prevented [4, p.176]. Despite the distinct natures of the two main forms of corrosion under insulation that can occur on different pipeline materials, water is a necessary precursor to both forms of corrosion, therefore if water can be eliminated from the system then both forms of corrosion can be controlled.

The purpose of the weatherproofing barrier formed by the cladding is primarily to protect the insulation and to keep the insulation dry, however, it would be impractical to attempt to create a barrier which would prevent any contact of the air (and inherent water vapour) with the annular space occupied by insulation, as this would require seals equivalent to a pressure vessel [4, p.174]. Therefore, temperature changes (due to cyclic processes or variations in the environment) cause the cladding and insulation system to breathe, allowing the ingress of water vapour. The ingress of water is further hastened as the condition of the cladding degrades over time, through mechanical damage (primarily caused by foot traffic), and deterioration of the sealants.

The principal sources of water are deluge systems, rainwater, process liquid spillage and condensation of water vapour [5, p.2]. Sites which are commonly reported to be locations of CUI problems are mid-span insulation joints and saddle supports, with joints at saddles leading to an even higher incidence of CUI. Vertical risers are also problematic, as they shed water which tends to collect at insulation joints at the bottom of the riser. Another situation which is very likely to lead to CUI problems is an area of exposed pipe on an insulated line, which can occur due to improper reinstatement of insulation following inspection or maintenance procedures, as this will readily allow water ingress into the exposed insulation [9, p.18]. Other sites which are problematic are those areas of pipelines which are subject to cyclic temperatures, with the lowest temperature at a value below the dew point, varying to temperatures above the ambient [4, p.174]. This causes water to condense on the pipe during the low temperature phase, which then allows corrosion to initiate as the temperature increases. The rate of the corrosion reaction will increase as the temperature of the pipeline increases to its maximum operating value. Even if this maximum temperature is sufficiently high to bake off the water inside the insulation, there still exists a transition period within which the pipe is both warm and wet, providing ideal conditions for CUI to occur. For corrosion of carbon and low-alloy steels, the range of temperatures of piping within which the majority of all CUI cases occur is from $-4\,^{\circ}\mathrm{C}$ to $120\,^{\circ}\mathrm{C}$ [10], although pipes with operating temperatures down to $-18\,^{\circ}\mathrm{C}$ can suffer from CUI if they have intermittent flow resulting in

a high proportion of time spent in the CUI temperature range [11]. Likewise, pipes with operating temperatures significantly above 120 °C can have metal temperatures low enough to be within the CUI temperature range if the insulation is damaged or humid conditions prevail, therefore the temperature range within which CUI can occur on pipes is given as being from −18 °C to 175 °C in [5, p.3]. For austenitic stainless steels, the temperature range which is problematic for SCC is from 50 °C to 175 °C [5, p.29].

1.2 Non-Destructive Evaluation Techniques for the Detection of CUI

One of the main difficulties of tackling the problem of CUI is the inability to easily detect those areas of pipe that are suffering from CUI. To this end, several diverse Non-Destructive Evaluation (NDE) techniques exist which can be deployed to inspect for CUI.

The first inspection technique should be an external visual inspection without the removal of any insulation. This can be beneficial as it will highlight areas which are at obvious risk of CUI: breaks and discontinuities in the cladding; insulation which has been left exposed after maintenance work; and cladding which is sagging under the weight of wet insulation. Beyond these very obvious signs, however, external visual inspection is very limited. The next stage for visual inspection would be to cut windows in the cladding and insulation to be able to examine the surface of the pipe itself. While this will reveal areas of corrosion at the location of the window, it is a sampling technique and therefore can easily miss serious cases of CUI or lead to an inaccurately favourable impression of the pipe's condition. In addition the windows themselves can be a source of water ingress, leading to corrosion problems where, previously, there were none. Complete visual inspection of the surface of the pipe is the most comprehensive method for detecting CUI, however, this requires the cladding and insulation to be completely removed along the entire length of the

pipe, and then subsequently reinstated, a process which is prohibitively expensive and time consuming [5, p.47].

Pulse-echo ultrasonic measurements can be made to determine the wall thickness at a point. This either requires complete removal of the insulation or requires cutting inspection windows, both of which are to be avoided for reasons previously stated. The advantage of this technique is that it gives the remaining wall thickness accounting for both external and internal corrosion, but the disadvantage is the difficulty of getting a reading on a corroded surface thus requiring significant surface preparation [5, p.47].

Several radiographic techniques exist, such as: profile radiography, digital radiography, flash radiography and real-time radiography. These are all techniques which use either x-rays or gamma rays to image the profile of the pipe or to provide information about the wall thickness of the internal pipe. Their main advantage is the ability to perform the inspection without the need to remove the insulation, and can be used with the pipe in-service. The main disadvantages are the strict safety requirements associated with ionising radiation, and the small area of inspection leading to slow rates of coverage or, if a sampling approach is adopted, the risk of missing problem areas [5, p.49].

A technique which can be used to comprehensively and rapidly inspect long lengths of pipeline around the entire circumference from a single inspection position is the guided wave ultrasonic technique. This technology involves fitting a ring-array of transducers around the pipe at one position. These transducers excite the propagation of low-frequency ultrasonic signals down the length of the pipeline. Any defects, such as cracks or corrosion, give rise to reflections of the incident signal, which return to the transducer array, allowing the detection of these defects. Several commercially available guided wave inspection systems have been developed [12, 13]. The advantages of guided ultrasonic waves include the ability to inspect long lengths of pipeline (25 m in each direction from a single array position [14]) about the entire circumference of the pipe, which is preferable to the spot testing of other techniques such as conventional ultrasound or radiographic methods. Another advantage is that

this technique inspects the pipeline with the insulation still in place, with the exception of a small length required to fit the transducer array. However, the technique requires an existing loss in wall thickness due to corrosion, before it can highlight areas which are at risk from CUI.

Pulsed eddy current inspection is another means of inspecting for corrosion under insulation; it is a method that is designed to measure the remaining wall thickness of the pipe with the cladding and insulation in place. This technique uses a direct current in a coil placed onto the cladding to create a stable magnetic field within the pipe under the insulation. The current in the coil is then switched off, creating eddy currents within the pipe. The time taken for these eddy currents to dissipate is related to the thickness of the metal and can therefore be used to measure the average remaining wall thickness in that area. The advantages are that it can be used without altering the insulation system in any way, and with the pipeline in-service. The disadvantages are the limited inspection area, and an inability to detect localised corrosion, and it is restricted by an inability to inspect a pipe through steel cladding [5, p.135].

A technique which takes an indirect approach to tackling the problem of CUI is that of the neutron backscattering technique. This method uses high energy neutrons emitted by a radioactive source to inspect the insulation, through the cladding, for the presence of water. Water will attenuate the energy of the neutrons, therefore the reflected neutrons will be of a lower energy if there is water present. The detection of low energy neutrons indicates the presence of water at that position, with the number of low energy neutrons detected being proportional to the amount of water present [10]. The advantages include the ability to perform the inspection with the pipeline in-service, and without removing any insulation; but the disadvantages include the safety requirements of the radioactive source, the limited inspection area, and the requirement to confirm corrosion with an additional inspection method such as x-ray or gamma radiography [5, p.50].

Another technique which detects water instead of the corrosion itself is infrared thermography. The premise is to use a thermographic camera to inspect the pipeline,

and areas of wet insulation will appear hotter than areas of dry insulation due to the reduced effectiveness of the wet insulation resulting in hot-spots on the pipeline. The increased safety and the speed of coverage of this technique eliminates the major disadvantages of neutron backscattering, however, the sensitivity and accuracy of the technique suffer, since only significant water volumes are detectable, and hot-spots can be caused through other means besides wet patches [5, 10].

1.3 The Premise for the Use of Microwaves for the Detection of CUI

As discussed in Section 1.2, the infrared thermographic and neutron backscattering techniques are distinct from the other inspection methods in that they aim to detect the water which causes the corrosion rather than the presence of active corrosion itself. This is an advantageous approach as it gives a much earlier indication of areas of a pipe that are likely to suffer from CUI, allowing sufficient time to mitigate the problem. However, the two techniques that are currently in use and capable of detecting water have serious limitations as discussed in Section 1.2; therefore, it would be beneficial to be able to use a long-range screening technique to monitor a length of pipeline for the first ingress of water into the insulation. This would provide an early warning of the likely occurrence of CUI and prompt remedial action to reseal the cladding, thereby preventing corrosion from initiating.

Microwave frequency techniques are seeing increased application in the field of NDE. A common use is to determine the strength of concrete structures by measuring the material properties using microwaves, including the water-to-cement ratio and the presence of Sodium Chloride [15–20]. Another application is that of the inspection of metallic surfaces for thin cracks using microwave probes [21–25]. A third area in which microwaves are being successfully used is that of the inspection for disbonds in layered dielectric composite materials [26–30]. However, the inspection technique

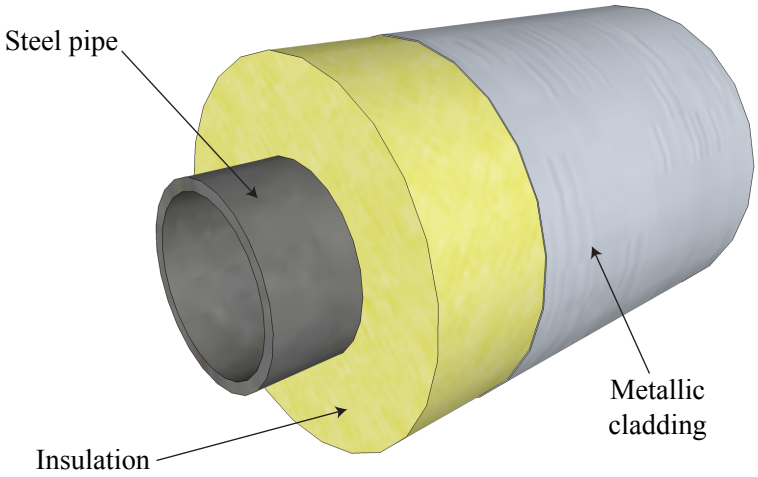

Figure 1.2: The structure of a clad and insulated pipeline can be used as a large coaxial waveguide to support the propagation of electromagnetic waves. The microwave regime is of particular interest due to the sensitivity of these frequencies to the presence of water, raising the possibility of being able to detect the first ingress of water into the insulation, allowing the initiation of corrosion to be prevented.

described in this thesis takes a fundamentally different approach to other forms of microwave NDE.

The technique which is the subject of this thesis is based on the premise that a pipeline which has been fitted with thermal insulation and metallic cladding is effectively a scaled-up version of a coaxial cable, with the inner conductor formed by the pipeline, the outer conductor formed by the cladding, and the thermal insulation layer acting as the dielectric within the coaxial cable, as shown in Figure 1.2. In this manner, the pipeline can be used as a coaxial waveguide to support the propagation of electromagnetic waves [31]. The premise for the technique is to excite microwave propagation down the length of the pipeline with the use of an antenna-based excitation system inserted into the insulation. If the cladding has become damaged and allowed the ingress of water, then this patch of wet insulation will give rise to a reflection of the incident microwave signal. The reflected signal returns to the exciting antenna, where it is received, and used to detect the presence of water

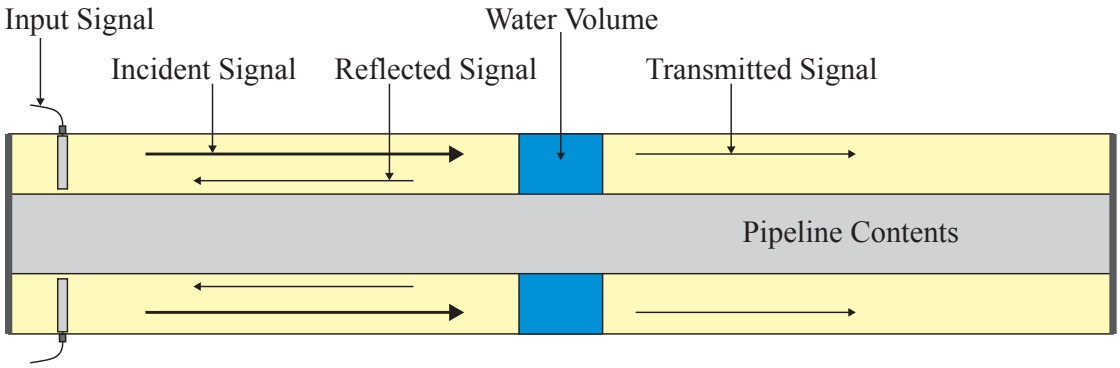

Figure 1.3: Antennas are inserted into the insulation layer, exciting microwave propagation down the length of the pipeline. Water volumes in the insulation act as impedance discontinuities, giving rise to a partial reflection of the incident signal which can be used to detect and locate wet sections of insulation along the length of the pipeline.

within the waveguide, and also to determine its position. This process is illustrated in Figure 1.3.

One of the reasons why microwave frequencies are of particular interest is the transparency of the insulation material to electromagnetic waves at these frequencies, so the inspection signal will experience very little attenuation. A second reason for considering electromagnetic waves in the microwave regime is the high value of the relative permittivity of water at these frequencies [32, p.315]. A high value for the relative permittivity is beneficial as it means that water will affect the impedance of the waveguide to a greater extent thus giving rise to a stronger reflection. This is because the characteristic impedance, Z_0, of a coaxial waveguide is given by the equation

$$Z_0 = \frac{1}{2\pi} \ln\left(\frac{a}{b}\right) \sqrt{\frac{\mu_0 \mu_r}{\epsilon_0 \epsilon_r}}, \tag{1.1}$$

where a and b are the radii of the outer and inner conductors respectively, and the material properties of the medium filling the waveguide are given by: the vacuum permeability, μ_0; the relative permeability, μ_r; the vacuum permittivity, ϵ_0; and the relative permittivity, ϵ_r [33, p.198]. It can be seen from this equation that the characteristic impedance varies with the relative permittivity of the material as $Z_0 \propto 1/\sqrt{\epsilon_r}$. We can assume that dry insulation has a relative permittivity equivalent to air, $\epsilon_r = 1$, (the validity of this assumption will be discussed in Section 3.1.1)

and we can take the value of the relative permittivity of water to be $\epsilon_r = 79.7$ at 1 GHz according to values given in [34]. A typical example of a pipeline specification would be a 6" Nominal Pipe Size (NPS), equivalent to an outer diameter of 6.625" = 168.2 mm, giving a value for the inner radius of $b = 84.1$ mm. Typically, this pipeline would be fitted with thermal insulation with a thickness of 3", giving an outer radius of $a = 160.3$ mm. We can calculate the impedance of this pipeline when dry to be $Z_{0_{dry}} = 38.7\,\Omega$, and if water has saturated the insulation across the entire cross-section then the impedance will be $Z_{0_{wet}} = 4.33\,\Omega$. The reflection coefficient, Γ, experienced by a signal incident on such a boundary between wet and dry insulation can be obtained with the simple analytical relationship [35, p.29] given by

$$\Gamma = \frac{Z_{0_{\text{wet}}} - Z_{0_{\text{dry}}}}{Z_{0_{\text{wet}}} + Z_{0_{\text{dry}}}} = \frac{\sqrt{\epsilon_{r_{\text{dry}}}} - \sqrt{\epsilon_{r_{\text{wet}}}}}{\sqrt{\epsilon_{r_{\text{dry}}}} + \sqrt{\epsilon_{r_{\text{wet}}}}}, \tag{1.2}$$

which gives $\Gamma = -0.80$. Therefore, if water breaches the cladding and fully saturates the insulation, then the boundary between the dry section of insulation and the wet patch will cause a reflection of 80 % of the incident signal back to the excitation antenna. Whilst a fully saturated insulation cross-section is not unusual, the first sign of water ingress will be the presence of water collecting at the 6 o'clock position within the cladding and gradually saturating the lower portion of the insulation, therefore presenting a smaller impedance discontinuity, and thus causing a smaller reflection. Chapter 6 of this thesis will discuss the sensitivity of the technique to the presence of water, including a measurement of the minimum cross-sectional extent of water that can be detected.

1.4 Similar Techniques

The principle of using the structure of the pipeline as a coaxial waveguide to support electromagnetic wave propagation was first proposed by Burnett and Frost, who developed a technique that is now marketed by Profile Technologies Incorporated (PTI). The general approach is described in patents [36,37] and the paper [38]. These indicate that the technique propagates electromagnetic waves in the radiowave

regime within the coaxial waveguide. However, the literature does not explain the details of how the technique operates, how the excitation system functions, nor does it provide sufficient quantitative evidence to determine the practical feasibility of the method. One potential disadvantage of the PTI implementation of the coaxial waveguide idea is that operating at the low frequencies of the radiowave regime is likely to lead to poor spatial resolution of waveguide features. The lack of data available to assess the feasibility of the PTI technique, its advantages and disadvantages, and its boundaries of operation, means that very little can be gained from the existence of such a technique in terms of scientific contributions to the development of a higher frequency guided microwave technique.

1.5 Outline of the Thesis

The objective of this thesis is to determine the feasibility of using guided microwaves to inspect the insulation layer of clad and insulated pipelines for the presence of water. This fundamental goal will be divided into subsidiary objectives, which will be covered as separate chapters within the thesis.

In order to provide some context for the scientific discussion within this thesis, the theoretical background to this work is discussed in Chapter 2. This will include the use of Maxwell's equations, and the analytical solution for electromagnetic waves propagating in rectangular waveguides. This represents a much simpler situation than a coaxial waveguide and is therefore ideal for introducing the properties of guided waves, such as dispersion and modal field distributions. This chapter will also introduce the numerical modelling technique which is used throughout this work to support the theoretical and experimental research.

The first objective of the thesis will be determining which modes propagate in the large coaxial waveguides formed by insulated pipelines and whether they can be used for inspection. This will be covered in Chapter 3 by examining the dispersion properties of the coaxial waveguide. This will include a description of the analytical model used to describe propagation in coaxial waveguides, and the results obtained

from this model; specifically the dispersion properties of the propagating modes and their modal field distributions.

Chapter 4 will discuss the development of the design of the antenna array used to excite guided microwave propagation in insulated pipelines. This will include a discussion of the significance of impedance matching at the antenna array, and a review of potential methods of improving the impedance match. The chapter will present a numerical study to optimise the antenna design in order to maximise energy transmission into the various coaxial waveguide dimensions formed by pipelines of typical industrial specifications.

Experimental validation of the guided microwave technique, and the optimised excitation system, is sought in Chapter 5. The experimental setup used in the laboratory to model insulated pipelines is described. This model experimental setup is also used to measure the effect on the microwave signal of some of the types of insulation that are commonly fitted to pipelines. Finally, this chapter will present results from a field test, which was conducted to validate the use of the model experimental setup in representing real pipeline conditions.

An issue of central importance to the performance of the guided microwave technique is the sensitivity with which it can detect water volumes within the waveguide. Chapter 6 describes an investigation to assess this sensitivity using numerical simulations and experiments in the laboratory. In addition, the chapter presents results from a realistic inspection scenario conducted during a field test on a section of real industrial pipeline.

Bends are a common feature on industrial pipelines. As such, the value of an inspection technique will be dependent on its ability to maintain its performance in the presence of common features such as bends. Chapter 7, therefore, presents numerical work to understand the behaviour of guided microwaves at bends. Experimental results are obtained to validate the numerical findings.

Another common feature of pipelines are pipe supports. Chapter 8 describes an investigation to quantify the reflection and transmission properties of pipe supports

in order to determine whether the guided microwave technique can be used to inspect beyond typical pipe supports.

A review of the thesis is provided in Chapter 9, followed by a summary of the main findings of the research. The thesis concludes with a discussion of some potential areas for future work, which would bring the technique closer to field application.

Chapter 2

Theoretical Background

The introductory chapter described the motivation for this project including the mechanism of corrosion under insulation. The current NDE techniques for the detection of CUI were reviewed including the reasons why this form of corrosion continues to be such a significant and ongoing problem. The premise for the use of guided microwaves to inspect the insulation layer of pipelines for the presence of water was described including the use of the structure of a clad and insulated pipeline as a coaxial waveguide to support electromagnetic wave propagation.

In order to understand the importance of several aspects of guided wave propagation, this section will present some of the relevant background theory. This will begin with Maxwell's equations, followed by the boundary conditions which exist at the walls of a waveguide, which allow them to guide electromagnetic waves. Before dealing with coaxial waveguides, the relatively simple case of a rectangular waveguide will be presented, including introducing the use of dispersion curves and concepts such as modes of propagation and field distributions.

In addition, this section will explain the necessity for numerical techniques to study complex problems and introduce the particular numerical technique which was used throughout this project. Following on from this, the theory for the method of signal analysis for locating impedance contrasts in a transmission line will be introduced,

accompanied by the manner in which the resolution of features in the waveguide can be optimised.

2.1 Maxwell's Equations

Maxwell's equations form the basis for the background theory describing the propagation of electromagnetic waves in waveguides. The equations are given by

$$\begin{aligned} \boldsymbol{\nabla} \cdot \mathbf{D} &= Q \\ \boldsymbol{\nabla} \cdot \mathbf{B} &= 0 \\ \boldsymbol{\nabla} \times \mathbf{E} &= -\frac{\partial \mathbf{B}}{\partial t} \\ \boldsymbol{\nabla} \times \mathbf{H} &= \frac{\partial \mathbf{D}}{\partial t} + \mathbf{J}, \end{aligned} \tag{2.1}$$

where $\mathbf{D}$ is the electric flux density; Q is the free charge density; $\mathbf{B}$ is the magnetic flux density; $\mathbf{E}$ is the electric field; $\mathbf{H}$ is the magnetic field; and $\mathbf{J}$ is the conduction current density. $\mathbf{D}$ is related to $\mathbf{E}$ by $\mathbf{D} = \epsilon_0 \epsilon_r \mathbf{E}$, where ϵ_0 and ϵ_r are the vacuum and relative permittivities of the dielectric material, respectively; whilst $\mathbf{B}$ is related to $\mathbf{H}$ by $\mathbf{B} = \mu_0 \mu_r \mathbf{H}$, where μ_0 and μ_r are the vacuum and relative permeabilities of the dielectric material, respectively. Maxwell's equations can be used to describe the propagation of uniform plane electromagnetic waves in a simple medium within which there are no free charges and currents, therefore $Q = 0$ and $\mathbf{J} = 0$ [39, p.132]. If we assume a sinusoidal time variation of the form $e^{j\omega t}$, where ω is the angular frequency and t is time, then we can write $\partial/\partial t = j\omega$. This gives us Maxwell's equations in the form given in [33, p.118] as

$$\begin{aligned} \boldsymbol{\nabla} \cdot \mathbf{D} &= 0 \\ \boldsymbol{\nabla} \cdot \mathbf{B} &= 0 \\ \boldsymbol{\nabla} \times \mathbf{E} &= -j\omega \mathbf{B} \\ \boldsymbol{\nabla} \times \mathbf{H} &= j\omega \mathbf{D}. \end{aligned} \tag{2.2}$$

A point-source of electromagnetic waves in free-space will create waves propagating in all directions, as such the intensity on this spherical wavefront will attenuate

according to the inverse-square law. In order to achieve transmission with lower attenuation, it is possible to confine the waves to travel in a particular direction with the use of a guiding physical structure. Such a guiding structure is known as a *waveguide*, and for electromagnetic waves, these usually take the form of an interface between a conductor and a dielectric. One example of an electromagnetic waveguide is the rectangular waveguide, which consists of a hollow metallic tube with a rectangular cross-section. The electromagnetic waves are confined by the metallic walls of the waveguide and are able to propagate with relatively low attenuation. It is the boundary conditions that exist at the interface between the conductor and the dielectric that allow these structures to guide the passage of electromagnetic waves.

The first boundary condition of a conductor-dielectric interface is that the tangential component of the electric field is continuous across the boundary, and since $\mathbf{E} = 0$ inside a perfect conductor, the electric field inside the dielectric must be perpendicular to the interface between the dielectric and the conductor. The second boundary condition is that the normal component of the magnetic flux density is continuous across the boundary. From the third of Maxwell's equations in (2.2), and since $\mathbf{E} = 0$ inside a perfect conductor, it can be seen that $\mathbf{B} = 0$ inside a perfect conductor. Therefore, the normal component of $\mathbf{B}$, and hence $\mathbf{H}$, inside the dielectric must be zero at the interface. As a consequence of these two conditions, in proximity to the surface of the conductor, the electric field within the dielectric must be oriented in a direction normal to the surface, and similarly the magnetic field must be oriented in a direction that is tangential to the surface.

These are the only boundary conditions required to solve Maxwell's equations for the case of a rectangular waveguide, however, for the more complex case of the coaxial waveguide, an additional condition exists. Due to the circular nature of this waveguide, the electric and magnetic fields at θ and $\theta + 2\pi$ must be equal, as this is the same point in space.

2.2 Analytical Solution for the Rectangular Waveguide

Before looking at the complex case of coaxial waveguides, it is beneficial to first study the relatively simple case of electromagnetic wave propagation in a rectangular waveguide.

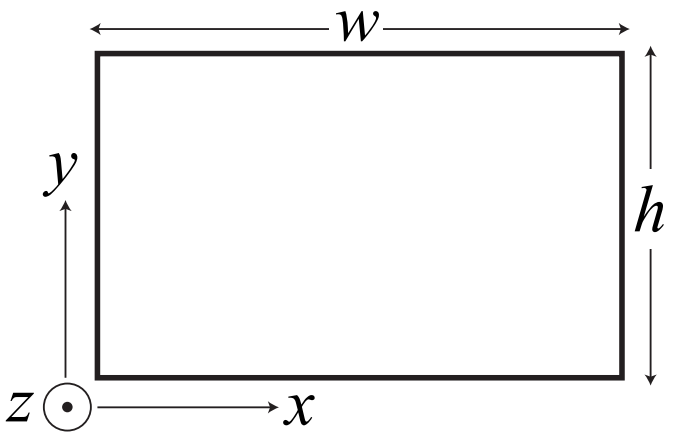

Figure 2.1: Cross-sectional view of a rectangular waveguide. The dimensions of the waveguide are denoted by w for the width, and h for the height.

The rectangular waveguide case has greater simplicity because the characteristic equation, which describes how the wave propagates, is explicit; characteristic equations are usually implicit and often difficult to solve. The characteristic equation for the rectangular waveguide is given by

$$\beta^2 = \omega^2 \epsilon_0 \mu_0 \epsilon_r \mu_r - \frac{p^2\pi^2}{w^2} - \frac{q^2\pi^2}{h^2}, \tag{2.3}$$

where β is the phase constant of the guided wave; ω is the angular frequency and is related to the frequency, f, by $\omega = 2\pi f$; w and h are the width and height of the waveguide, respectively, as shown in Figure 2.1; and p and q are integers. By assigning integer values to p and q in the characteristic equation, all the permitted values of β can be found. Each combination of p and q refers to a distinct mode of propagation within the waveguide [33, p.212].

If β^2 is positive, then there are two real roots given by $\pm\beta$, with the sign indicating the direction of propagation relative to the z-axis. If β^2 is negative, then there are

two imaginary roots at $\pm j\beta$; such imaginary phase constants are said to be cutoff, with the resultant wave being referred to as an evanescent wave. Evanescent waves are not capable of propagating; their amplitude decays exponentially with z. The one remaining possibility is for $\beta^2 = 0$. The frequency at which this occurs is known as the cutoff frequency, f_c, and is dependent on the dimensions of the waveguide and the p and q values of the particular mode. The cutoff frequency for rectangular waveguide modes is given by

$$f_c = \sqrt{\frac{1}{4\epsilon_0\mu_0\epsilon_r\mu_r}}\left(\frac{p^2}{w^2} + \frac{q^2}{h^2}\right). \tag{2.4}$$

For any given mode in a particular waveguide, at frequencies below the cutoff frequency β^2 is negative and the mode is evanescent, whereas as the frequency increases above the cutoff, β^2 becomes positive and the mode begins to propagate within the waveguide. The mode whose cutoff occurs at the lowest frequency is said to be the *lowest mode*, with modes that begin to propagate at higher frequencies being referred to as *higher order modes*.

There are two velocities of significance when dealing with the propagation of waves; these are the phase velocity, ν_p, and the group velocity, ν_g. The phase of the wave travels at the phase velocity; for example, the tip of a particular peak in a wavepacket will travel at this speed. The phase velocity is often much greater than the speed of light. The group velocity refers to the speed at which the envelope of the wave travels; this is the speed at which information is carried by the wave, and does not exceed the speed of light. The expressions for the phase and group velocity are

$$\nu_p = \frac{\omega}{\beta} \tag{2.5}$$

$$\nu_g = \frac{\partial\omega}{\partial\beta}. \tag{2.6}$$

The characteristic equation in (2.3) can be used in conjunction with the expressions in (2.5) and (2.6) to plot the relationship between the wave velocities and the frequency; these are known as dispersion curves. Figure 2.2 displays the dispersion curves of the phase and group velocities, normalised to the speed of light in vacuum, c_0, for some of the lower modes in a rectangular waveguide.

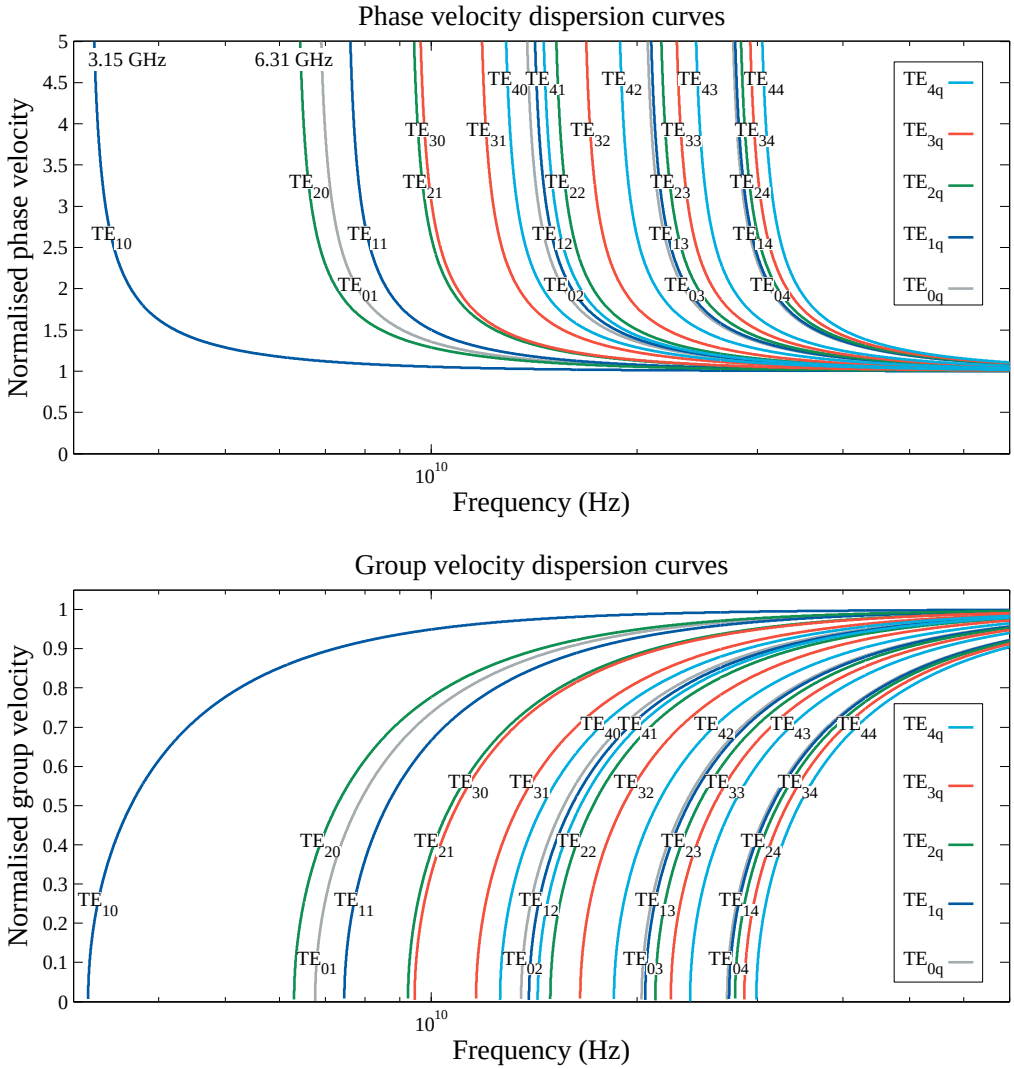

Figure 2.2: Phase and group velocity dispersion curves, normalised to the speed of light in vacuum, for some of the lower modes in a G band rectangular waveguide (dimensions of $w = 47.5\,\text{mm}$ and $h = 22.1\,\text{mm}$ and a frequency range of 3.95 to 5.85 GHz bandwidth).

Each of the curves in Figure 2.2 represents a separate mode of propagation within the waveguide, and they are labelled according to the standard mode nomenclature for rectangular waveguides. There are in fact two series of modes, referred to as: Transverse Magnetic (TM) modes, with $H_z = 0$; and Transverse Electric (TE) modes, with $E_z = 0$. However, for the rectangular waveguide, the phase constant of a TM mode is equal to the phase constant of the equivalent TE mode, therefore only the TE modes are plotted in Figure 2.2. Waldron [33] prefers to refer to the TE and TM modes as H and E modes, respectively, however, the TE and TM notation

is the one that is used predominantly in the field [35, 39–41]. The numbers in the subscript of the mode refer to the p and q values for that mode, i.e. TE_{pq} and TM_{pq}, and denote the periodicity of the variation of the field in the x and y directions respectively. It can be seen that all of the modes are highly dispersive, with their phase and group velocities being highly dependent on the frequency. The phase velocities are always greater than the speed of light in the medium, c, whilst the group velocities are always less than c, but both are asymptotic to c. It can be shown that the phase and group velocities are related by the expression

$$\nu_g \leq \frac{c}{\sqrt{\epsilon_r \mu_r}} \leq \nu_p, \tag{2.7}$$

or, in another form

$$\nu_p \nu_g = \frac{c^2}{\epsilon_r \mu_r}. \tag{2.8}$$

In order to maximise the performance of an inspection system, it is necessary to maximise the signal-to-coherent-noise ratio (SCNR). Coherent noise refers to any deterministic signals that corrupt the signal of interest and cannot be removed by temporal averaging. One aspect of using guided waves for inspection, which has an adverse effect on the SCNR, is the fact that modes propagating within waveguides often undergo dispersive propagation. It was seen in Figure 2.2 that all of the modes are highly dispersive. This has the effect that a wavepacket will undergo temporal spreading as it propagates, due to each of the frequency components inside the wavepacket travelling at different phase velocities. This temporal spreading causes a reduction in the amplitude of the signal, which adversely effects the SCNR.

Another aspect of guided wave propagation which can adversely effect the SCNR is the fact that a waveguide is capable of supporting an infinite number of modes of propagation. If there are multiple modes propagating, each of the modes will travel at a different group velocity, and undergo varying degrees of dispersion. Consequently, the propagating modes will become out-of-phase with each other and undergo complicated interference processes. The result will be a signal which is impossible to interpret due to the multitude of reflections and the high level of coherent noise due to interference effects. It is for this reason that it is desirable to excite

a signal within the waveguide which contains only a single mode; this is known as pure mode excitation.

From Figure 2.2 it can be seen that there is a narrow frequency range within which there is only the TE_{10} mode that is capable of propagating, before the TE_{20} begins to propagate, i.e. from 3.15 to 6.31 GHz. Rectangular waveguides come in a range of standard sizes, which are referred to as R band, D band, S band, etc. The dimensions of these standard rectangular waveguides are strictly controlled in order to gain maximum utility from this pure mode region, and hence each waveguide has a defined operating frequency range. Figure 2.2 displays the dispersion curves for a G band rectangular waveguide, which has an operating frequency range of 3.95 to 5.85 GHz. The lower limit of the operating frequency range (3.95 GHz) is somewhat higher than the cutoff frequency of the TE_{10} mode (3.15 GHz), this is in order to operate the waveguide in the region of the dispersion curve which is flattest and hence least dispersive. The upper limit of operating frequency range 5.85 GHz is also slightly lower than the cutoff frequency of the TE_{20} mode (6.31 GHz), and this is in order to avoid interference from the evanescent TE_{20} mode, an effect which becomes greater the closer the operating frequency is to the cutoff frequency.

For comparison, the phase velocity dispersion curves of an R band and an S band rectangular waveguide are plotted in Figure 2.3. It can be seen that as the size of the waveguide decreases, the cutoff frequencies of the various modes increase, and consequently the waveguide can be used for operations in a higher frequency range.

It is very useful to be able to visualise the distribution of the electric and magnetic fields within the waveguide for each of the modes which are capable of propagating. Equations known as the field components of the waveguide allow the Cartesian components of the electric and magnetic fields to be calculated. Waldron [33, p.224]

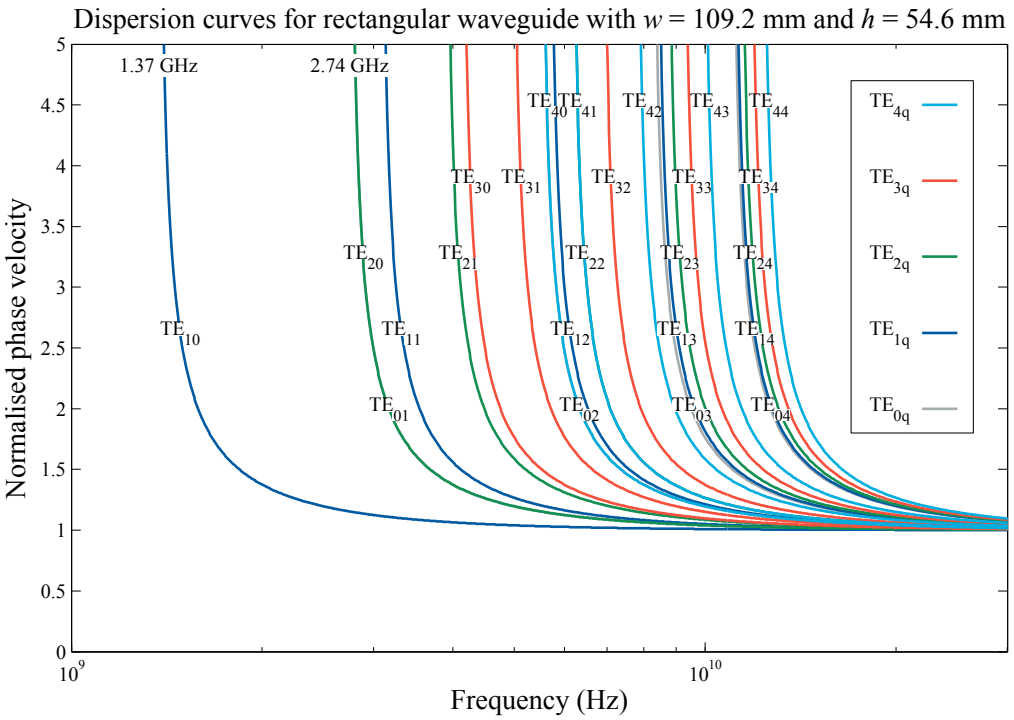

(a) R band waveguide (1.7 - 2.6 GHz)

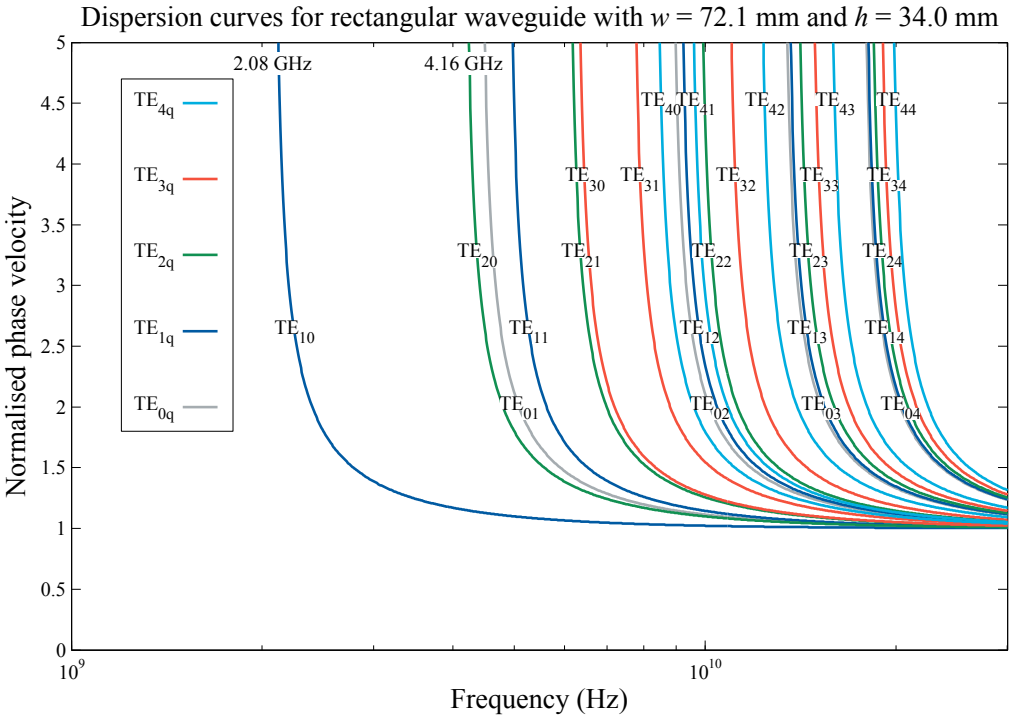

(b) S band waveguide (2.6 - 3.95 GHz)

Figure 2.3: Phase velocity dispersion curves for two standard sizes of rectangular waveguide. It can be seen that each waveguide is capable of supporting the propagation of only the TE_{10} mode within its operating frequency range.

gives the field components for TM modes in rectangular waveguide as

$$
\begin{aligned}
E_x &= \frac{p\lambda_0^2}{w\sqrt{wh\epsilon_r}}\sqrt{\frac{2\bar{\beta}\sqrt{\mu_0/\epsilon_0}}{\epsilon_r\mu_r-\bar{\beta}^2}}\cos k_x x \sin k_y y \\
E_y &= \frac{q\lambda_0^2}{h\sqrt{wh\epsilon_r}}\sqrt{\frac{2\bar{\beta}\sqrt{\mu_0/\epsilon_0}}{\epsilon_r\mu_r-\bar{\beta}^2}}\sin k_x x \cos k_y y \\
E_z &= \frac{j2\sqrt{2}\lambda_0}{\sqrt{wh\epsilon_r}}\sqrt{\frac{\epsilon_r\mu_r-\bar{\beta}^2}{\bar{\beta}\sqrt{\epsilon_0/\mu_0}}}\sin k_x x \sin k_y y \\
H_x &= \frac{-q\lambda_0^2}{h\sqrt{wh}}\sqrt{\frac{2\epsilon_r\sqrt{\epsilon_0/\mu_0}}{\bar{\beta}\left(\epsilon_r\mu_r-\bar{\beta}^2\right)}}\sin k_x x \cos k_y y \\
H_y &= \frac{p\lambda_0^2}{w\sqrt{wh}}\sqrt{\frac{2\epsilon_r\sqrt{\epsilon_0/\mu_0}}{\bar{\beta}\left(\epsilon_r\mu_r-\bar{\beta}^2\right)}}\cos k_x x \sin k_y y \\
H_z &= 0,
\end{aligned}
\tag{2.9}
$$

where the Cartesian components of the wavenumber vector are given by $k_x = p^2\pi^2/w^2$, and $k_y = q^2\pi^2/h^2$; and $\bar{\beta}$ is the phase constant normalised to that of vacuum, i.e. if λ_0 and λ_{wg} are the wavelengths in vacuum and inside the waveguide respectively, then $\bar{\beta} = \lambda_0/\lambda_{wg} = \lambda_0\beta/2\pi$. The field components for TE modes are

$$
\begin{aligned}
E_x &= \frac{-q\lambda_0^2}{h\sqrt{wh}}\sqrt{\frac{2\mu_r\sqrt{\mu_0/\epsilon_0}}{\bar{\beta}\left(\epsilon_r\mu_r-\bar{\beta}^2\right)}}\cos k_x x \sin k_y y \\
E_y &= \frac{p\lambda_0^2}{w\sqrt{wh}}\sqrt{\frac{2\mu_r\sqrt{\mu_0/\epsilon_0}}{\bar{\beta}\left(\epsilon_r\mu_r-\bar{\beta}^2\right)}}\sin k_x x \cos k_y y \\
E_z &= 0 \\
H_x &= \frac{-p\lambda_0^2}{w\sqrt{wh\mu_r}}\sqrt{\frac{2\bar{\beta}\sqrt{\epsilon_0/\mu_0}}{\epsilon_r\mu_r-\bar{\beta}^2}}\sin k_x x \cos k_y y \\
H_y &= \frac{q\lambda_0^2}{h\sqrt{wh\mu_r}}\sqrt{\frac{2\bar{\beta}\sqrt{\epsilon_0/\mu_0}}{\epsilon_r\mu_r-\bar{\beta}^2}}\cos k_x x \sin k_y y \\
H_z &= \frac{j2\sqrt{2}\lambda_0}{\sqrt{wh\mu_r}}\sqrt{\frac{\epsilon_r\mu_r-\bar{\beta}^2}{\bar{\beta}\sqrt{\mu_0/\epsilon_0}}}\cos k_x x \cos k_y y.
\end{aligned}
\tag{2.10}
$$

These field components allow the field distributions to be plotted across a cross-section of the rectangular waveguide for each of the modes. Figure 2.4 displays the electric and magnetic field distributions for nine of the lowest modes in rectangular waveguides. These are in good agreement with the field distributions plotted in [33, 39, 41, 42].

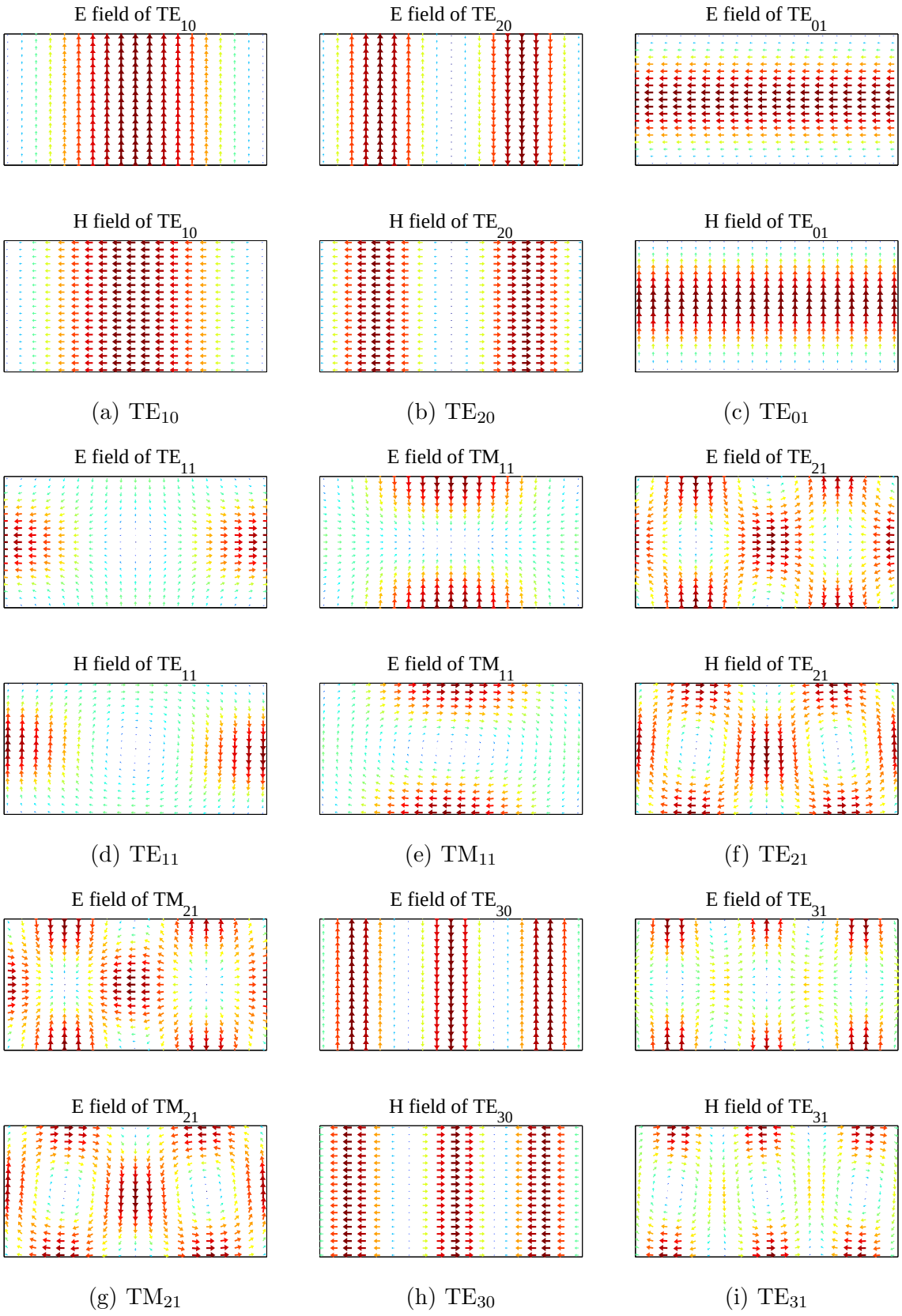

(a) TE_{10} (b) TE_{20} (c) TE_{01}

(d) TE_{11} (e) TM_{11} (f) TE_{21}

(g) TM_{21} (h) TE_{30} (i) TE_{31}

Figure 2.4: Field patterns for the nine lowest modes that exist in a rectangular waveguide with $w/h = 2$.

As previously mentioned, it can be seen that the p and q values in the TE_{pq} and TM_{pq} nomenclature describe the periodicity in the variation of the field across the x and y directions of the waveguide cross-section, respectively. For example, the TE_{21} mode displays two half-cycles of variation from one side of the waveguide to the other, along the x-axis, whilst also displaying a single half-cycle of variation along the y-axis, from the top of the waveguide to the bottom.

2.3 Numerical Techniques to Study Complex Problems

The development of this guided microwave inspection technique requires studying problems of a complex nature, such as the reflection from a non-axisymmetric patch of wet insulation in the waveguide, or investigating how the transmissive properties of an array of antennas behave as the design of the antennas is varied. Whilst an analytical solution could be found in some of the simpler circumstances (for example, the case of a single probe antenna exciting a rectangular waveguide [43, p.471]), the time taken to do so, coupled with the complexity of such a solution, and its applicability to only one type of problem are factors which render this approach unappealing. Modern computing power has reached the point where numerical techniques can be used to quickly and accurately simulate problems of great complexity.

There are a variety of numerical techniques that are employed for simulating electromagnetic problems, with some specialising in their own area of application. Of the more versatile methods which exist, some of the most widely used include: the finite element method, the finite-difference time-domain technique, and the method of moments. The software package that was used to study the complex problems that arose in the development of this guided microwave technique was the commercially available Microwave Studio (MWS) from the company Computer Simulation Technology. This software uses the Finite Integration Technique (FIT), which was first proposed by Weiland in 1977 [44]. Once the structure has been meshed, the

FIT technique is unique in that it solves the integral form of the full set of Maxwell's equations, rather than the differential form [45]. The method calculates all six vector components of electric field strength and magnetic flux density at each of the elements in the meshed structure. The FIT technique has the advantages of being computationally efficient, accurate, easy to use, and less prone to late-time instability than other techniques [44, 46, 47]. MWS offers a variety of different solvers, including both a time-domain solver and a frequency-domain solver. The simulations performed in the development of this technique require a wide bandwidth, therefore the time-domain solver represents the most appropriate choice, due to its computational efficiency in simulating wide bandwidths.

2.4 Synthetic Time-Domain Reflectometry

The objective of this guided microwave technique is to develop an inspection system capable of detecting and locating areas of impedance contrast in a waveguide. This is a common objective, particularly in the telecommunications industry, within which detecting and locating faults in cables is vitally important. Traditionally, this has been achieved by sending a step function into the cable and using the reflections to determine the position, and impedance of the reflecting feature, a method known as Time-Domain Reflectometry (TDR). An alternative approach, which is more widely used nowadays, is to launch individual frequency components into the cable, and use the magnitude and phase of the reflected signal to obtain the reflection coefficient as a function of frequency. The inverse Fourier transform can then be applied to view the trace in the time-domain, producing a result which is analogous to both the original step function method and an ultrasonic A-scan (the one-dimensional data trace of amplitude against time that is received when an ultrasonic transducer is placed on a sample). As this method of reflectometry uses the frequency-domain it is sometimes referred to as frequency-domain reflectometry [48, p.238], but more recently as synthetic Time-Domain Reflectometry [49, 50]. Whilst the resultant synthetic TDR signal is similar to the conventional TDR signal, the former has a number of advantages over the latter, including [48, 51]: improved signal-to-noise

ratio; reduction in zero-level drift and zero ambiguity; the flexibility to employ any desired excitation signal; and the option to use time gating to separate the responses due to multiple features. Synthetic TDR was used throughout this project to obtain both experimental and simulated results, but the abbreviation TDR will be used throughout the thesis to refer to synthetic TDR.

The value of a guided wave inspection system is intrinsically related to the resolution with which it can see features in the waveguide. Good resolution leads not only to the ability to resolve reflections from two closely spaced features, but also to higher accuracy in locating features, and greater ease in interpreting signals. Using TDR, the resolution that is achieved is related to the bandwidth of frequencies comprising the input signal, according to the equation

$$\Delta f \propto \frac{1}{\Delta t} = \frac{\nu_g}{2\Delta z}, \tag{2.11}$$

where Δf is the frequency bandwidth of the signal ($\Delta f = f_{\max} - f_{\min}$), Δt is the temporal resolution, Δz is the axial resolution, and ν_g is the group velocity at the centre frequency. It can be seen from Equation (2.11) that the temporal, and hence axial, resolution is optimised by maximising the bandwidth of the signal. Therefore, the wider the range of frequencies that can be used in the inspection, the sharper and clearer the resultant signal will be.

2.5 Summary

The theory of guided wave propagation has been presented, beginning with Maxwell's equations, followed by a discussion of the boundary conditions which exist in electromagnetic waveguides. The analytical solution for electromagnetic waves propagating within rectangular waveguides has been reviewed, including the use of dispersion curves to analyse the dispersion properties of waveguide modes, and the merits of non-dispersive propagation. In addition, the field distributions for rectangular waveguide modes were displayed, and the advantages of pure-mode excitation were highlighted.

The necessity for the use of simulating complex problems with numerical techniques was stated, followed by the method and advantages of the FIT technique, which was used during this project.

The method of synthetic TDR was introduced, and its advantages over conventional TDR were listed. The relationship between the resolution that can be achieved with TDR and the frequency bandwidth of the signal was stated, highlighting the need to maximise the bandwidth of operation of the guided microwave technique in order to obtain sufficient spatial resolution of waveguide features for the technique to be a practicable inspection tool.

Chapter 3

Coaxial Waveguide Theory

Chapter 2 presented Maxwell's equations and the boundary conditions that exist on the walls of a waveguide. Before looking at the complex case of coaxial waveguide propagation, the theory describing propagation within rectangular waveguides was discussed, including introducing the characteristic equation and field component equations. The use of these equations in calculating dispersion curves and field distributions was described. Also described in the previous chapter was the manner in which the information from these figures is used to optimise the signal-to-noise ratio of a guided wave inspection system through suitable choice of mode in order to minimise undesirable dispersion effects and through careful choice of frequency range in order to achieve pure-mode excitation.

A pipe which has been thermally insulated and clad forms a large coaxial waveguide. Many of the concepts from rectangular waveguide propagation are analogous for the case of coaxial waveguides. This chapter is concerned with the development of a model to describe the propagation of electromagnetic waves in coaxial waveguides, thereby enabling the design of a guided microwave inspection system. This will involve presenting the relationships that are used to calculate the dispersion curves for coaxial waveguides, and displaying the resultant dispersion curves for various typical industrial pipeline specifications. In addition, the field component equations

for coaxial waveguides will be presented, and the resultant field distributions for several coaxial waveguide modes of propagation will be displayed.

3.1 Assumptions Made by the Model

Two assumptions are made in order to develop the model used to describe electromagnetic wave propagation in coaxial waveguides; these will be discussed in detail in the following two subsections. The first of these is the assumption that the insulation material has a negligible effect on the propagation, and the second assumption is that the walls of the waveguide formed by the pipeline have an electrical conductivity that is sufficiently high for it to be considered infinite.

3.1.1 Transparent Insulation

The large coaxial waveguide formed by an insulated pipeline can be used to support the propagation of electromagnetic waves of any frequency, not just microwave frequencies. However, it is the microwave frequency range which is of particular interest, for two main reasons. Firstly, the insulation material which fills the annulus of the coaxial waveguide is a dielectric and as such should be relatively transparent to microwave frequencies. The second reason is that water, which is the feature that the technique aims to detect, interacts strongly with electromagnetic waves in the microwave frequency range (a fact that is well known due to the use of this effect in the microwave heating of food), and hence should be readily distinguishable from the dielectric insulation. The interaction of electromagnetic waves with water is discussed in more detail in Section 6.1.

The material property of a dielectric which describes how it interacts with electric fields is known as its permittivity, ϵ. The permittivity of a material is the product of the vacuum permittivity, $\epsilon_0 = 8.854 \times 10^{-12}\,\mathrm{F\,m^{-1}}$ and the relative permittivity of the material, ϵ_r, so that: $\epsilon = \epsilon_0\epsilon_r$. The relative permittivity is a complex quantity

which depends on the frequency

$$\epsilon_r(\omega) = \epsilon'_r(\omega) - j\epsilon''_r(\omega), \tag{3.1}$$

with the real part, ϵ'_r, governing the extent to which a material is capable of storing energy, whilst the imaginary part, ϵ''_r, describes the energy dissipation within the material [52, p.162].

Materials which are used for insulation generally owe their low thermal conductivity values, κ, to the fact that their physical structure predominantly consists of trapped air; it is the air which has a low thermal conductivity value of $\kappa = 0.0241\,\mathrm{W\,m^{-1}\,K^{-1}}$ at 273 K [52, p.94]. Air has a relative permittivity of $\epsilon_r = 1.000536$ [52, p.170], which is sufficiently close to 1 that air is considered to be electromagnetically identical to vacuum. As insulation materials are comprised primarily of air, it is expected that they will have relative permittivity values very close to 1. As an example of this, rockwool, which is one of the most commonly used insulation materials in the UK, is said to have a relative permittivity of $\epsilon_r = 1.4$ in [53], whilst rigid Polyurethane Foam (PUF), which is the predominant type of insulation used in Alaska, is said to have a relative permittivity of $\epsilon_r \approx 1.3$ in [54]. It is important to note, however, that these insulation materials are manufactured in a wide range of densities, and that the relative permittivity is dependent on the volume fraction of air, with less dense insulations having values for ϵ_r closer to 1. Therefore, it is more useful to specify the intrinsic relative permittivity for the materials that the insulation is formed from. Obtaining these intrinsic permittivity values requires some estimation and extrapolation from known values and densities. It is estimated that rockwool has an intrinsic relative permittivity of $\epsilon_r \approx 6$ [55], whilst polyurethane, in a solid rather than foamed state, has an intrinsic relative permittivity of $\epsilon_r \approx 3$ [56].

Due to this similarity to air, it is expected that the dissipation of energy within the insulation materials will be minimal. As such, the effect of the insulation material is neglected from the model used in this chapter, by using a relative permittivity of $\epsilon_r = 1$ throughout. The validity of this assumption will be assessed in Section 5.4 when the effect of different types of insulation materials are experimentally measured.

Table 3.1: Table listing the values of the resistivity and conductivity of typical pipeline materials. Pipes are typically formed from carbon or stainless steel, whilst cladding can be stainless steel, galvanised carbon steel or aluminium. Kaye and Laby [52, p.150] provided these values.

Material	Resistivity, ρ $(1 \times 10^{-8}\,\Omega\,\mathrm{m})$		Conductivity, σ $(1 \times 10^{6}\,\mathrm{S\,m^{-1}})$	
	273 K	373 K	273 K	373 K
Carbon steel	17.0	23.2	5.88	4.31
Stainless steel	55.0	63.4	1.82	1.58
Aluminium	2.42	3.57	41.3	28.0

3.1.2 Perfectly Conducting Waveguide

The pipe and the cladding act as the inner and outer conductors of the coaxial waveguide. During electromagnetic wave propagation, the changing magnetic field within the waveguide excites surface currents on the interior metallic surfaces of the waveguide. If the electrical resistivity, ρ, of the metal of the walls is high, then these currents will experience resistance to their flow. The result of this effect is an attenuation of the passage of the electromagnetic waves. The inner pipe is typically formed from either carbon steel or stainless steel, whilst the outer cladding can be formed from carbon steel, stainless steel or aluminium. The resistivities and conductivities, $\sigma = 1/\rho$, for these three materials are given in Table 3.1, from which it can be seen that the electrical conductivities all take very high values, sufficiently high to validate the assumption that the waveguide walls have infinite conductivity and are, therefore, perfectly conducting.

In order to ensure that nothing on the outside of the cladding can affect the waves propagating inside the waveguide, it is worth considering the skin depth, δ, of the surface currents induced by microwave propagation in the waveguide. The skin depth equates to the depth at which the current density within a conductor decreases to

$1/e$ of its surface value, and is given by the relationship

$$\delta = \sqrt{\frac{2}{\omega\mu_0\mu_r\sigma}}, \tag{3.2}$$

which can be found in [32, p.220], therefore the higher the frequency, the shallower the skin depth. Consequently the maximum penetration would occur at the lowest frequencies that will be used, which are 10 MHz with this technique. The maximum penetration depth of electric current within a conductor is generally accepted to be 3δ, which will take a maximum value of $3\delta = 355\,\mu\text{m}$ for the case of a 10 MHz frequency in stainless steel, the lowest conductivity material. The cladding will have a minimum thickness of 500 µm which is comfortably greater than the maximum penetration depth of the surface currents.

3.2 The Analytical Solution Used by the Model

A coaxial waveguide consists of two cylindrical conductors that are aligned coaxially along the z-axis, forming an annular space between them which is filled with a material with permittivity, ϵ, and permeability μ. The radius of the outer conductor is denoted by a, whilst the radius of the inner conductor is given by b. This arrangement is shown in Figure 3.1.

For a complete discussion of the analytical solution to coaxial waveguide propagation, refer to Chapter IV in Waldron [33, p.204]. This section is limited to the results which enable the development of a model to describe the dispersion characteristics and field distributions of coaxial waveguide modes. The characteristic equations for the modes which propagate in coaxial waveguides are given by

$$J_p(k_r a)Y_p(k_r b) - J_p(k_r b)Y_p(k_r a) = 0 \tag{3.3}$$

$$J'_p(k_r a)Y'_p(k_r b) - J'_p(k_r b)Y'_p(k_r a) = 0, \tag{3.4}$$

where k_r is the radial wavenumber, J_p is a Bessel function of first kind of order p, and Y_p is a Bessel function of second kind (also known as a Neumann function) of order p [33, p.246]. The prime notation in J'_p and Y'_p denotes differentiation, where

$$J'_p(\xi) = \frac{1}{2}\left(J_{p-1}(\xi) - J_{p+1}(\xi)\right) \tag{3.5}$$

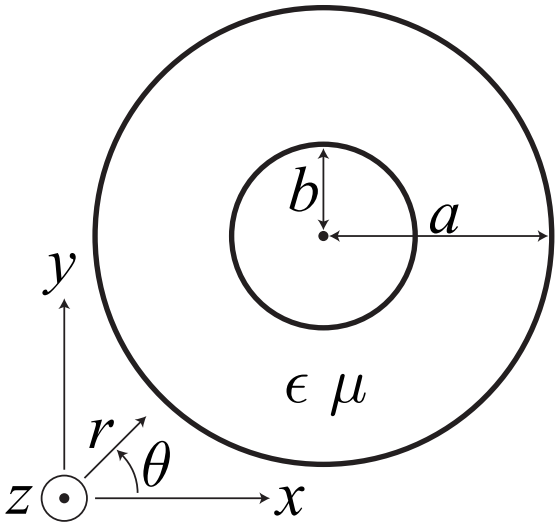

Figure 3.1: Schematic diagram of the cross-section of a coaxial waveguide. The radius of the outer conductor is referred to as a, whilst the radius of the inner conductor is b.

is a relationship which can be used to obtain the derivative of either of the functions J_p or Y_p [33, p.32]. Contrary to the case of the rectangular waveguide, the Transverse Magnetic (TM) and Transverse Electric (TE) series of modes have distinct dispersion curves. Equation (3.3) is the characteristic equation for TM modes, whilst Equation (3.4) is the characteristic equation for TE modes. In the discussion of rectangular waveguides in Chapter 2 it was seen that the integers p and q are used to describe the distinct modes of propagation. This is also the case here, for coaxial waveguides, with the two series of modes having their own set of p and q modes: TM_{pq} and TE_{pq}.

The Equations (3.3) and (3.4) are implicit, and they can only be solved numerically. For each particular mode, the p and q values are input into either (3.3) or (3.4) depending on the mode series, with p determining the order of the Bessel functions, and q indicating the number of the zero (the position on the x-axis where the function crosses and the y value becomes equal to zero) of the Bessel function corresponding to the solution of the characteristic equation for that particular mode. Therefore in order to solve the characteristic equations for any mode (p, q) which exists in the coaxial waveguide, it is necessary to be able to determine the position of the q^{th} zero of any Bessel function, or its derivative, of order p. If we take $\xi = kb$ and define $\gamma = a/b$ then $ka = \gamma\xi$ which can be substituted into Equation (3.3) or (3.4) and

solved to give ξ as the q^{th} zero of the Bessel function of order p, for a particular combination of p and q. Then the phase constant, β becomes

$$\beta = \left(\frac{2\pi}{\lambda}\right)\sqrt{1 - \frac{\xi^2\lambda^2}{4\pi^2 b^2}}. \tag{3.6}$$

The phase and group velocities in a coaxial waveguide adhere to the same relationship with the phase constant as for the rectangular waveguide and are therefore given in (2.5) and (2.6). Using these, the phase and group velocity dispersion curves can be plotted for any of the TM_{pq} and TE_{pq} modes. However, there is one mode which is fundamentally different to the TM and TE modes and did not exist in the rectangular waveguide: it is the Transverse Electromagnetic (TEM) mode, also referred to as the transmission-line mode. Whilst the transverse electric modes lack a longitudinal electric field component and the transverse magnetic modes lack a longitudinal magnetic field component, the TEM mode lacks both longitudinal components. The phase constant for the TEM mode, assuming that $\epsilon_r = 1$, is given by

$$\beta = \frac{2\pi}{\lambda_0} = \omega\sqrt{\epsilon_0\mu_0} = \frac{\omega}{c}. \tag{3.7}$$

It can be seen from the relationships in (2.5) and (3.7) that for the TEM mode $\omega/\beta = \nu_p = c$, therefore the TEM mode has a phase velocity equal to the speed of light at all frequencies, and is therefore non-dispersive. Similarly from (2.6) it can be seen that $\nu_g = \partial\omega/\partial\beta = c$, demonstrating that the group velocity is also non-dispersive and equal to the speed of light at all frequencies. The phase and group velocity dispersion curves, normalised to c, for many of the lowest modes in both the TE and TM series are plotted in Figure 3.2.

It can be seen from the dispersion curves in Figure 3.2 that the majority of the modes are highly dispersive, with the TEM mode being the only exception. These dispersion curves are plotted for a coaxial waveguide with dimensions of $a = 157.5\,\text{mm}$ and $b = 80\,\text{mm}$, which is approximately equivalent to a 6" pipe with 3" insulation, though, as mentioned in Section 3.1, the permittivity of the medium within the waveguide is assumed to be equal to that of vacuum. From Figure 3.2 it becomes apparent that the modes are divided into distinct families, defined by the value of the integer q, so that there is a TE_{p1} mode family on its own spread over the lower

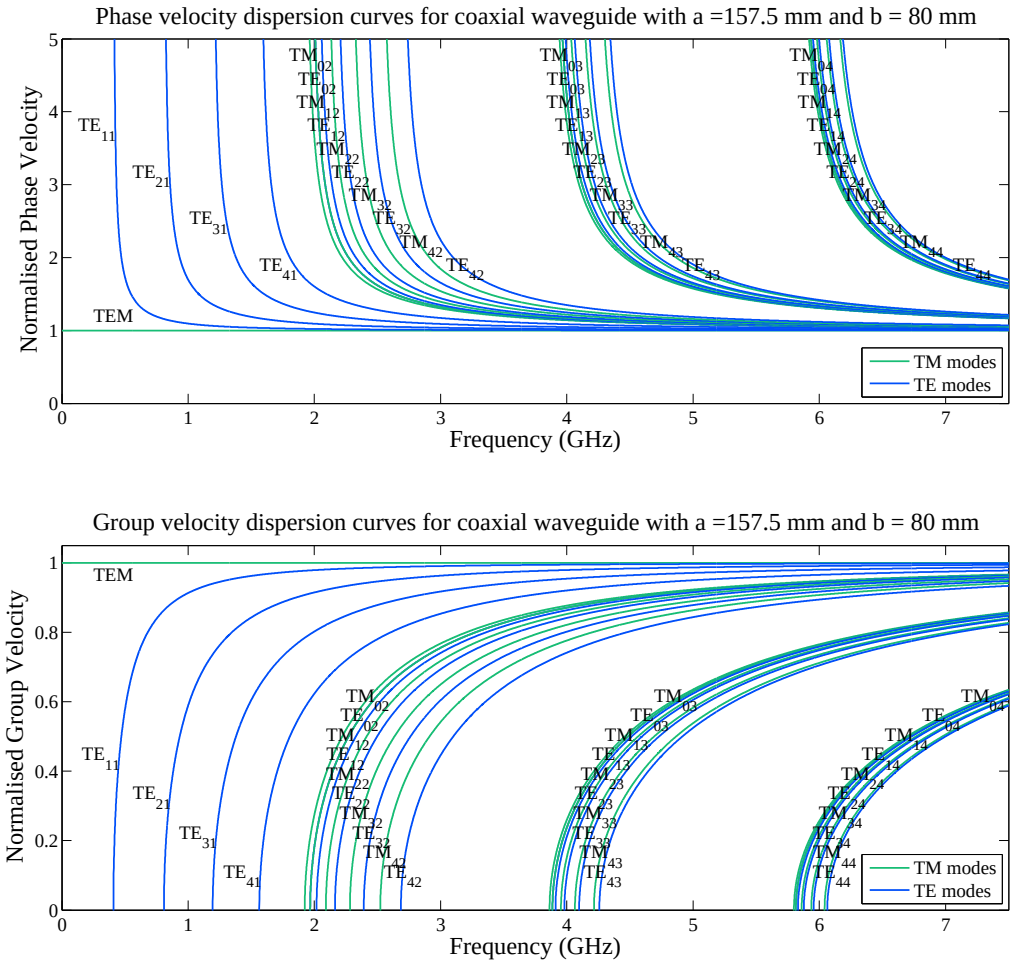

Figure 3.2: Phase and group velocity dispersion curves, normalised to the speed of light in vacuum, for some of the lower modes in a coaxial waveguide with dimensions of $a = 157.5\,\text{mm}$ and $b = 80\,\text{mm}$. Only the modes up to TM_{44} and TE_{44} are plotted, for clarity.

frequencies, and above this the TE_{p2} and TM_{p2} families overlapping each other. The explanation for this separation of the mode families is facilitated by the plots of the modal field distributions, which will be presented later in this section.

The purpose of developing this model allowing the calculation of these dispersion curves is to assess the feasibility of using these insulated pipelines as coaxial waveguides. To this end, Figure 3.3 displays the dispersion curves for six different pipeline specifications. The three plots in the left-hand column show the effect on the dispersion curves of increasing the pipe diameter from 6" to 60" whilst keeping the

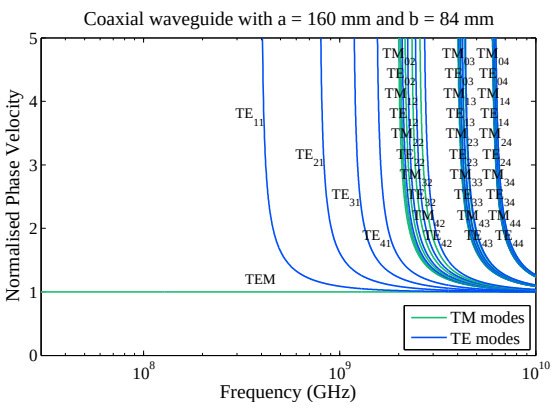

(a) 6” pipe with 3” insulation

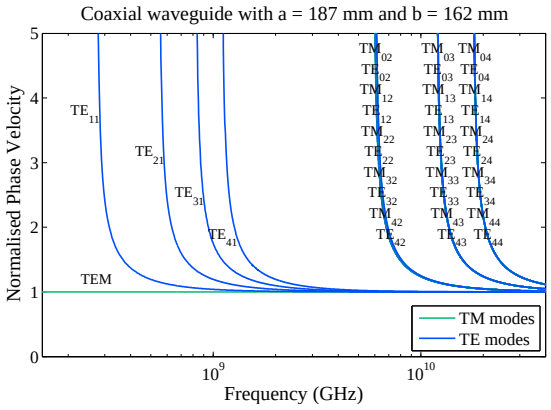

(b) 12” pipe with 1” insulation

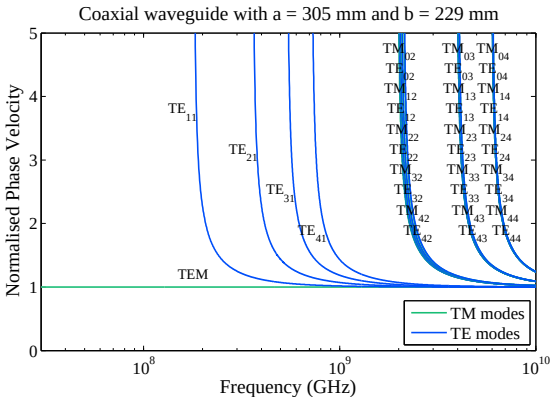

(c) 18” pipe with 3” insulation

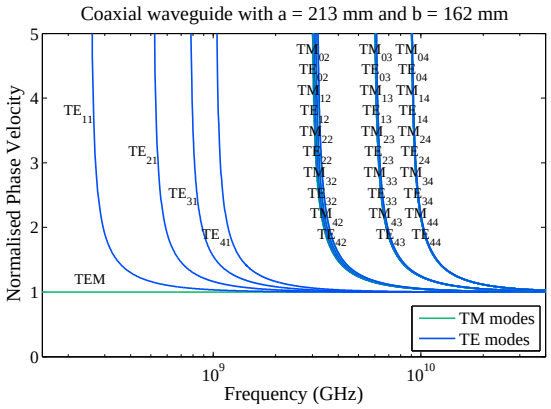

(d) 12” pipe with 2” insulation

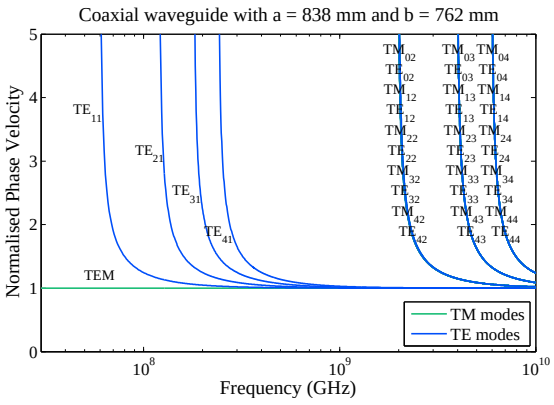

(e) 60” pipe with 3” insulation

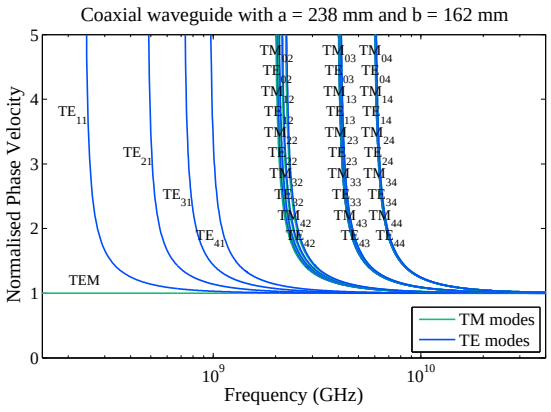

(f) 12” pipe with 3” insulation

Figure 3.3: Phase velocity dispersion curves for the lowest modes in coaxial waveguides. Figures (a), (c), and (e) show the effect of increasing the radius of the inner pipe, whilst (b), (d), and (f) show the effect of increasing the thickness of the insulation.

thickness of the insulation constant at 3". It can be seen that the TE_{p1} mode family moves towards lower frequencies as the pipe diameter increases, with the cutoff frequency of the lowest TE_{11} mode occurring at 400 MHz, 180 MHz, and 60 MHz for the 6, 18, and 60" pipes, respectively. However, the cutoff frequency of the lowest non-TE_{p1} mode, the TM_{02} mode, occurs at approximately the same frequency of 1.97 GHz in each case. The three plots in the right-hand column show the effect of increasing the insulation thickness whilst keeping the pipe diameter constant at 12". It can be seen that the TE_{p1} mode family does not move with respect to frequency as the insulation thickness increases from 1" to 3", with the cutoff frequency of the lowest TE_{11} mode occurring at approximately the same frequency of 250 MHz for each of the three insulation thicknesses plotted. However, the modes of all the other mode families do vary with respect to frequency; they move towards lower frequencies as the thickness of the insulation is increased. The cutoff frequency of the lowest non-TE_{p1} mode, TM_{02}, occurs at 5.9 GHz, 2.9 GHz, and 2.0 GHz for insulation thickness of 1", 2", and 3", respectively.

In order to gain sufficient understanding of the modes of propagation in coaxial waveguides to be able to effectively design the guided wave inspection system, the modal field distributions are required. The field component equations were derived from expressions given in [33] to give the relationships required to plot the field distributions for TM modes, TE modes and the special case of the TEM mode. For

TM modes, the field components for modes for which $p \neq 0$ are given by

$$\begin{aligned}
E_r &= \frac{2\lambda_0}{\omega\pi\epsilon_0\epsilon_r}\frac{X'_p(kr)\sin p\theta}{\sqrt{a^2X'^2_p(\gamma\xi) - b^2X'^2_p(\xi)}} \\
E_\theta &= \frac{2\lambda_0 p}{\omega\pi\epsilon_0\epsilon_r kr}\frac{X_p(kr)\cos p\theta}{\sqrt{a^2X'^2_p(\gamma\xi) - b^2X'^2_p(\xi)}} \\
E_z &= \frac{j2\lambda_0 k}{\omega\pi\epsilon_0\epsilon_r\beta}\frac{X_p(kr)\sin p\theta}{\sqrt{a^2X'^2_p(\gamma\xi) - b^2X'^2_p(\xi)}} \\
H_r &= -\frac{2\lambda_0 p}{\pi\beta kr}\frac{X_p(kr)\cos p\theta}{\sqrt{a^2X'^2_p(\gamma\xi) - b^2X'^2_p(\xi)}} \\
H_\theta &= \frac{2\lambda_0}{\pi\beta}\frac{X'_p(kr)\sin p\theta}{\sqrt{a^2X'^2_p(\gamma\xi) - b^2X'^2_p(\xi)}} \\
H_z &= 0,
\end{aligned} \tag{3.8}$$

where

$$\begin{aligned}
X_p(kr) &= J_p(kr)Y_p(ka) - J_p(ka)Y_p(kr) \\
X'_p(kr) &= J'_p(kr)Y_p(ka) - J_p(ka)Y'_p(kr).
\end{aligned} \tag{3.9}$$

However the TM modes for which $p = 0$ (TM_{0q}), have field components given by

$$\begin{aligned}
E_r &= \frac{2\lambda_0}{\omega\pi\epsilon_0\epsilon_r}\frac{X'_0(kr)}{\sqrt{a^2X'^2_0(\gamma\xi) - b^2X'^2_0(\xi)}} \\
E_\theta &= 0 \\
E_z &= \frac{j2\lambda_0 k}{\omega\pi\epsilon_0\epsilon_r\beta}\frac{X_0(kr)}{\sqrt{a^2X'^2_0(\gamma\xi) - b^2X'^2_0(\xi)}} \\
H_r &= 0 \\
H_\theta &= \frac{2\lambda_0}{\pi\beta}\frac{X'_0(kr)\sin p\theta}{\sqrt{a^2X'^2_0(\gamma\xi) - b^2X'^2_0(\xi)}} \\
H_z &= 0.
\end{aligned} \tag{3.10}$$

The field components for the TE modes are given by the following set of equations

$$
\begin{aligned}
E_r &= -\frac{2\lambda_0 p}{\pi\beta kr}\frac{Z_p(kr)\sin p\theta}{\sqrt{a^2-\frac{p^2}{k^2}Z_p^2(\gamma\xi)-b^2-\frac{p^2}{k^2}Z_p^2(\xi)}}\\
E_\theta &= -\frac{2\lambda_0}{\pi\beta}\frac{Z_p'(kr)\cos p\theta}{\sqrt{a^2-\frac{p^2}{k^2}Z_p^2(\gamma\xi)-b^2-\frac{p^2}{k^2}Z_p^2(\xi)}}\\
E_z &= 0\\
H_r &= \frac{2\lambda_0}{\omega\pi\mu_0\mu_r}\frac{Z_p'(kr)\cos p\theta}{\sqrt{a^2-\frac{p^2}{k^2}Z_p^2(\gamma\xi)-b^2-\frac{p^2}{k^2}Z_p^2(\xi)}}\\
H_\theta &= -\frac{2\lambda_0 p}{\omega\pi\mu_0\mu_r kr}\frac{Z_p(kr)\sin p\theta}{\sqrt{a^2-\frac{p^2}{k^2}Z_p^2(\gamma\xi)-b^2-\frac{p^2}{k^2}Z_p^2(\xi)}}\\
H_z &= \frac{j2\lambda_0 k}{\omega\pi\mu_0\mu_r\beta}\frac{Z_p(kr)\cos p\theta}{\sqrt{a^2-\frac{p^2}{k^2}Z_p^2(\gamma\xi)-b^2-\frac{p^2}{k^2}Z_p^2(\xi)}},
\end{aligned}
\tag{3.11}
$$

where

$$
\begin{aligned}
Z_p(kr) &= J_p(kr)Y_p'(ka)-J_p'(ka)Y_p(kr)\\
Z_p'(kr) &= J_p'(kr)Y_p'(ka)-J_p'(ka)Y_p'(kr).
\end{aligned}
\tag{3.12}
$$

The TEM mode has a unique set of field components, which are given by

$$
\begin{aligned}
E_r &= \frac{\lambda_0\sqrt{\beta}}{r\sqrt{2\omega\pi\epsilon_0\ln(\frac{a}{b})}}\\
E_\theta &= 0\\
E_z &= 0\\
H_r &= 0\\
H_\theta &= \frac{\omega\epsilon_0\epsilon_r\lambda_0}{r\sqrt{2\beta\omega\pi\epsilon_0\ln(\frac{a}{b})}}\\
H_z &= 0.
\end{aligned}
\tag{3.13}
$$

The relationships in (3.8), (3.10), (3.11), and (3.13) can be used to plot the modal field distributions for any of the modes which propagate in coaxial waveguides. Figure 3.4 displays the electric and magnetic field distribution on a cross-section of a coaxial waveguide with $\gamma = a/b = 4$ for fifteen of the lowest modes capable of propagating in coaxial waveguides.

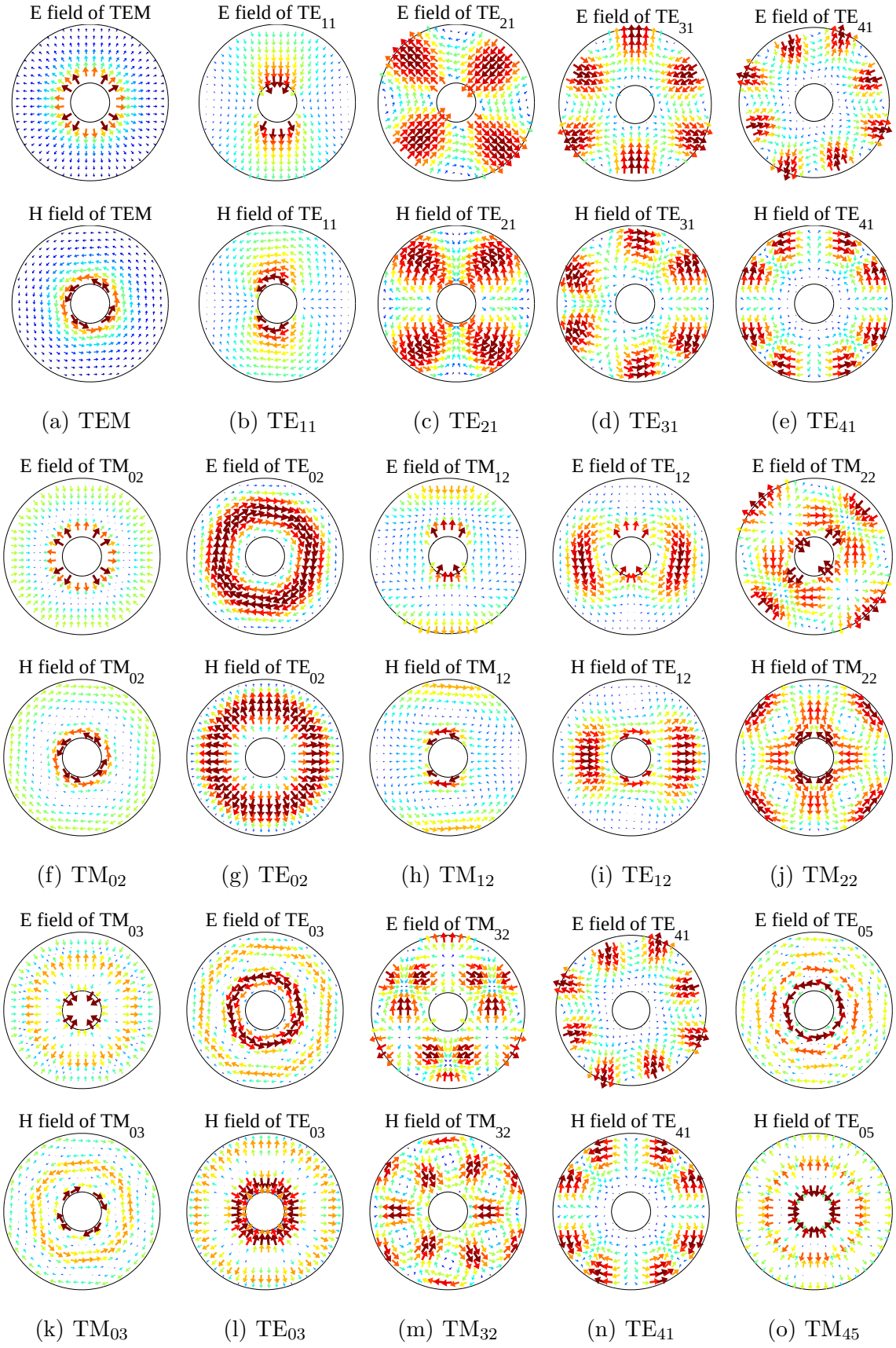

Figure 3.4: Field patterns for fifteen of the modes that exist in coaxial waveguides.

It is apparent from Figure 3.4 that there is a relationship between the p and q values of a mode and the field distribution, which is analogous to that demonstrated by the rectangular waveguide. The value of the p integer corresponds to the number of cycles of variation of the field about the circumference of the waveguide, whilst the q integer relates to the number of half-cycles of variation in the radial direction, from the inner conductor to the outer. This is intuitive if a coaxial waveguide is considered to be a rectangular waveguide that has been stretched along the x-axis and wrapped around onto itself. However, whilst the q integer directly relates to the number of cycles along the y-axis in the rectangular waveguide, for coaxial waveguide mode nomenclature, it is the quantity $q-1$ that corresponds to the number of half-cycles in the radial direction. This discrepancy in the mode nomenclature is corrected with the notation used by Waldron in [33], however, the TM and TE nomenclature is the one which has persisted.

It was noted earlier in this section, in reference to Figure 3.2, that the dispersion curves of the modes tend to group together into mode families. With an understanding of the periodicity in the field distributions of the modes, this grouping behaviour can be explained. The TEM mode propagates at all frequencies and thus does not have a cutoff frequency, therefore it is the TE_{11} mode which is the mode with the lowest cutoff frequency. The cutoff frequency is directly related to the physical size of the space within which the field distribution must be accommodated. This is because, at the cutoff frequency, the wavenumber vector, $\mathbf{k}$, is contained in the plane of the cross-section of the coaxial waveguide, thus must match the spatial constraints of the waveguide. A diagram illustrating how the wavenumber vector would look if the annulus of the coaxial waveguide were unwrapped, is displayed in Figure 3.5.

In order to understand the behaviour of the cutoff frequencies of the modes in coaxial waveguides as a function of variables such as pipe diameter, and insulation thickness, we begin by looking at the wavenumber vector. The magnitude of $\mathbf{k}$ is given by

$$|\mathbf{k}| = \frac{2\pi f}{c} = \frac{2\pi}{\lambda}, \tag{3.14}$$

where λ is the wavelength in an infinite medium with material properties equal to those of the medium filling the waveguide. The wavenumber vector has radial and

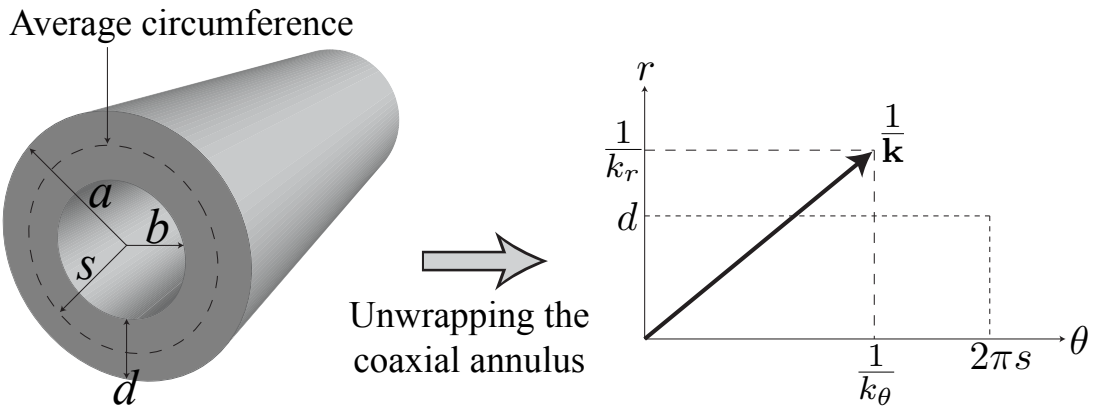

Figure 3.5: Diagram illustrating the unwrapping of the coaxial annulus. The average radius of the coaxial waveguide is denoted by s, giving a circumference of $2\pi s$, and the annular distance is denoted by d. The wavenumber vector, $\mathbf{k}$, has radial and circumferential coordinates given by k_r and k_θ. At the cutoff frequency of a mode, the wavenumber vector is contained in the plane of the cross-section of the waveguide, and the two dashed boxes in the Figure will coincide.

circumferential components, as shown in Figure 3.5, which are related according to

$$|\mathbf{k}|^2 = k_r^2 + k_\theta^2. \tag{3.15}$$

Converting wavenumbers into wavelengths using (3.14) and cancelling the 2π factor, gives

$$\left(\frac{1}{\lambda}\right)^2 = \left(\frac{1}{\lambda_r}\right)^2 + \left(\frac{1}{\lambda_\theta}\right)^2, \tag{3.16}$$

where λ_r and λ_θ are the radial and circumferential components of the wavelength. Considering a mode $T_{p,q}$; it has already been described that there are p full-cycles of oscillation circumferentially, and $q-1$ half-cycles of oscillation radially. Therefore it can be seen that

$$\lambda_r = \frac{2d}{q-1} \qquad \text{and} \qquad \lambda_\theta = \frac{2\pi s}{p}. \tag{3.17}$$

Thus, for the $T_{p,q}$ mode, the cutoff frequency, $F_{p,q} = c/\lambda$, is given by

$$\left(\frac{F_{p,q}}{c}\right)^2 = \left(\frac{q-1}{2d}\right)^2 + \left(\frac{p}{2\pi s}\right)^2. \tag{3.18}$$

If we compare two cutoff frequencies $F_{p,q}$ and $F_{p+1,q}$, we obtain

$$\frac{F_{p,q}^2}{c^2} = \left(\frac{q-1}{2d}\right)^2 + \frac{p^2}{4\pi^2 s^2} \tag{3.19}$$

$$\frac{F_{p+1,q}^2}{c^2} = \left(\frac{q-1}{2d}\right)^2 + \frac{p^2+1+2p}{4\pi^2 s^2}. \tag{3.20}$$

Subtracting (3.19) from (3.20), we find

$$\frac{F_{p+1,q}^2 - F_{p,q}^2}{c^2} = \frac{1+2p}{4\pi^2 s^2}. \tag{3.21}$$

Rewriting this using the difference of two squares, and taking the difference between these two cutoff frequencies to be $\Delta F = F_{p+1,q} - F_{p,q}$, and taking the average of the two cutoff frequencies to be $\bar{F} = \frac{1}{2}(F_{p+1,q} + F_{p,q})$ gives

$$\Delta F = \frac{c^2(1+2p)}{2\pi^2 s^2 \bar{F}}. \tag{3.22}$$

From (3.22), we can draw certain conclusions which explain the trends in the cutoff frequencies of the modes in the plots in Figure 3.3. As the value of q increases, (3.18) indicates that the cutoff frequency will increase; thus, $\bar{F}$ will also increase. Consequently, this causes a decrease in ΔF, according to (3.22). This is the reason why the dispersion curves of the mode families tend to overlap each other more closely at higher values of q, a trend which can be seen by comparison of the TM_{p2}, TM_{p3}, and TM_{p4} mode families in Figure 3.3(a).

From (3.18) it can be seen that as the thickness of the insulation, s, increases, $\bar{F}$ decreases, thus, the separation between the cutoff frequencies of the modes widens as ΔF increases. This can be seen by comparison of the TM_{p2} mode family in Figures 3.3(b), (d), and (f).

Finally, we know that as the pipe diameter increases, the average radius of the waveguide, s, increases, and from (3.22) it can be seen that this causes ΔF to decrease. This is a trend which is observed during comparison of the TM_{p2} mode family in Figures 3.3(a), (c), and (e); the dispersion curves of the mode family become more closely overlapping as the pipe diameter increases.

Close comparison of Figure 3.4(a) with Figures 3.4(b),(c),(d), and (e) reveals a fundamental difference in the symmetry between the TEM mode and the modes of

the TE_{p1} mode family. Whilst the TEM mode is axisymmetric, with no variation in its field distribution about the circumference of the waveguide, the modes of the TE_{p1} mode family are non-axisymmetric with p cycles of variation about the circumference of the waveguide. There are many other modes which display the same axisymmetric field distribution as the TEM mode, in fact any mode with $p = 0$ will be axisymmetric, however, they begin to propagate at higher frequencies than the first few modes of the TE_{p1} mode family.

3.3 Design of a Guided Wave Inspection System

With the coaxial waveguide model fully developed, allowing the dispersion curves and field distribution of any mode of propagation to be plotted, the guided microwave inspection system can be designed appropriately to take full advantage of the properties of the coaxial waveguide modes and the frequency bandwidth available. There are several factors to consider during the design of the inspection system, which will be discussed in turn in this section.

3.3.1 Non-Dispersive Propagation

The disadvantages of dispersive wave propagation were mentioned in Section 2.2 in relation to the rectangular waveguide. A wavepacket typically consists of a spectrum of frequencies; during dispersive propagation, each of these frequency components will propagate at a different group velocity. As a result the wavepacket spreads out in time as it propagates causing a loss of amplitude and an undesired increase in the duration of the wavepacket. Therefore, it is advantageous to perform an inspection using a mode that is capable of non-dispersive propagation. It is ideal, therefore, that the coaxial waveguide is capable of supporting the TEM mode, as this mode is non-dispersive and represents the ideal mode with which to perform the inspection.

3.3.2 Mode Purity

The requirement for mode purity was discussed in Section 2.2. The propagation of a signal containing multiple modes leads to interference between the modes and a high level of coherent noise in the signal, leading to an inability to perform an effective inspection. Therefore, it is desirable to propagate only a single mode. As the TEM mode is non-dispersive it is the ideal mode with which to perform the inspection, therefore our excitation of the waveguide would seek to excite only the TEM mode. Pure mode excitation of the TEM mode would provide an inspection signal which is non-dispersive and should give a good signal-to-coherent-noise ratio.

3.3.3 Frequency Bandwidth

An important consideration when selecting a frequency range for the inspection is the interaction of water with electromagnetic waves of those frequencies. It has already been noted in Section 1.3 that the amplitude of the reflection from water is dependent on the relative permittivity of water. Grant [34] gives a figure of $\epsilon_r = 79.7$ at 1 GHz. Jackson [32, p.315] displays a figure plotting the index of refraction of water, n, as a function of frequency, which is reproduced as Figure 6.1 in Section 6.1, in which the electromagnetic wave interaction with water is discussed. From this figure it can be seen that the index of refraction has a high value of $n = 9$ from low frequencies up to 10 GHz, with the value dropping off at higher frequencies. The relative permittivity is related to the index of refraction by $\epsilon_r = n^2$, therefore $\epsilon_r = 81$ in this frequency range, which is in agreement with the value given by Grant. In order to maximise the sensitivity of the technique it would be beneficial to operate in the frequency range within which the relative permittivity of water has a high value: at frequencies below 10 GHz.

Time-Domain Reflectometry was discussed in Section 2.4, from which Equation (2.11) revealed that the broader the bandwidth of the inspection signal, the better the resolution of waveguide features would be. Therefore, from this information, we would seek to maximise the upper frequency limit of the excitation signal, with the

lower frequency limit being determined by the microwave generation hardware to be 10 MHz.

3.4 Use of an Array of Antennas

We have determined that we wish to propagate a non-dispersive mode, and ideally achieve excitation of only a single mode. These requirements can be met by exciting only the TEM mode. However, the difficulty arises when we try to meet the requirements for the bandwidth of the signal. In order to achieve pure mode excitation with a single antenna or a horn, only frequencies up to the cutoff of the TE_{11} mode can be used, which imposes a severe restriction on the bandwidth of the signal. For example, the cutoff frequency of the TE_{11} mode for a 60" pipe occurs at 60 MHz, which would result in a minimum resolvable distance of 2.5 m (assuming $\Delta f = 1/\Delta t$). Such a resolution would adversely affect the performance and value of the inspection technique and is therefore unacceptable.

The approach that was adopted to overcome this problem, was to use a frequency range up to the cutoff frequency of the TM_{02} mode, giving a bandwidth of 2 GHz (this would be the minimum bandwidth available based on the lowest cutoff frequency of the TM_{02} mode which occurs with 3" insulation). A bandwidth of 2 GHz would lead to an axial resolution of 75 mm [57], which would deliver good spatial resolution of features within the waveguide. This approach means that some of the lower modes of the TE_{p1} mode family are capable of propagating, therefore the excitation system needs to be designed to achieve pure-mode excitation of the TEM mode. The method employed here aims to remove the spurious modes of the TE_{p1} mode family by means of an array of antennas distributed regularly about the circumference of the waveguide. If the field produced by the antenna array does not match the mode shape of the selected mode, the input energy will be distributed across other, spurious modes, therefore the array needs to be designed such that the antenna array field matches that of the TEM mode. The basic principle of this method is

already in use in guided ultrasonic waves [12, 58, 59], wherein the excitation system exploits the characteristics of the mode shapes of different guided waves.

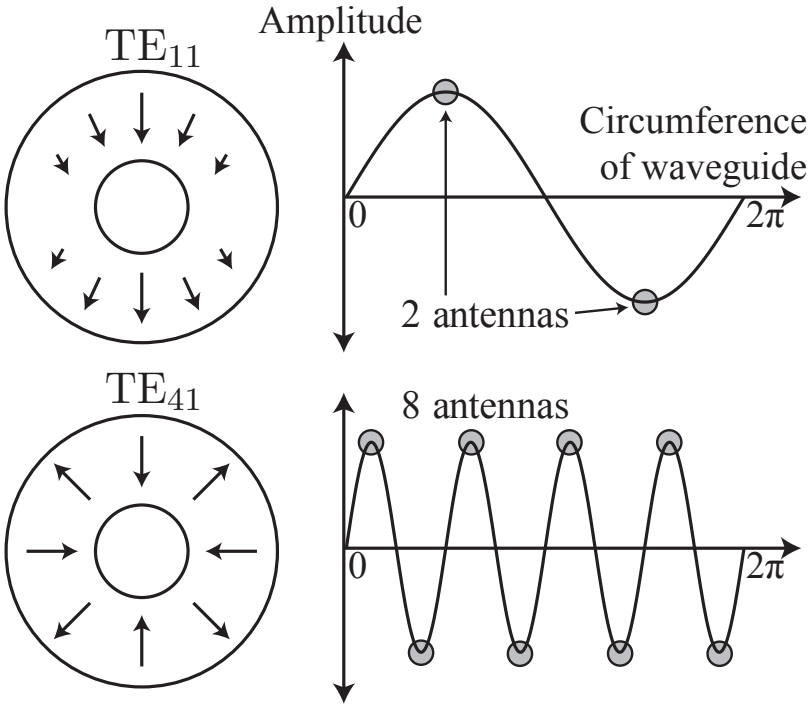

Figure 3.6: Diagram illustrating the use of an antenna array to suppress non-axisymmetric modes. The diagrams on the left represent the mode structures of the modes: TE_{11} and TE_{41}. The diagrams on the right provide an unwrapped representation of how the electric field of these modes varies about the circumference of the waveguide; the TE_{11} mode has one cycle of variation, whilst the TE_{41} has four cycles of variation about the circumference. With two antennas per cycle, any positive electric field amplitude is cancelled by the corresponding signal measured by the next antenna positioned a half cycle around the circumference.

The difference in the symmetry of the axisymmetric TEM mode and the non-axisymmetric TE_{p1} modes has already been mentioned. This difference in symmetry can be used as a differentiating factor to suppress only the TE_{p1} modes. If P takes the p value of the highest propagating member of the TE_{p1} mode family within the excited bandwidth, then the ring-array will require $2P$ antennas, which will be arranged at regular intervals about the circumference. This number of antennas is sufficient to suppress all of the propagating non-axisymmetric modes, with no adverse effect on the TEM mode. For instance, considering the reception problem, it

will be sufficient to take the signals received by each antenna and add them in phase as illustrated in Figure 3.6. By employing two antennas per cycle of circumferential variation of non-axisymmetric modes, the amplitude of the positive electric field due to a non-axisymmetric mode that is detected by any antenna is exactly cancelled by an equal negative amplitude detected by a corresponding antenna in the array. On the other hand, the TEM mode is reinforced when summing the signals, as it has a mode structure that is axisymmetric and all the signals are added coherently. By reciprocity the cancellation of higher order modes also occurs when the array is used to excite the waveguide, leading to pure TEM excitation. Each of the antennas in the array is supplied with an identical signal by employing a splitter component, which splits a single channel into the required number of channels to supply the array. The splitter is designed to preserve the equality of the magnitude and phase across all of the channels of the array, in order to ensure that the summation process is able to accurately cancel out the non-axisymmetric modes. Clearly, this array approach cannot be applied to filter the TM_{02} and TE_{02} modes as they are axisymmetric and whose cutoff frequencies, therefore, determine the maximum bandwidth that can be achieved with the antenna array. A complete discussion of the factors affecting the design of the antenna array will be given in Chapter 4.

3.5 Summary

In this chapter, the theory describing electromagnetic wave propagation within coaxial waveguides has been described, leading to the development of a model allowing the calculation of the dispersion curves and field distributions for any mode of propagation in the coaxial waveguides formed by insulated pipelines of various realistic dimensions.

The assumptions made by the model are covered, followed by introducing the characteristic equations for the two series of modes that can propagate. The field components for the modes are given, and the field distributions of several of the lower modes are plotted. The behaviour of the modes in the dispersion curves is explained,

with several sets of dispersion curves plotted for varying pipeline sizes and insulation thicknesses.

The design of a guided wave inspection system is discussed, including the topics of dispersive propagation, mode purity and the effect of frequency bandwidth. The chapter concludes with an evaluation of the feasibility of using the large coaxial waveguides formed by industrial pipelines to support the propagation of guided microwaves capable of inspecting for the presence of water. Whilst the conventional approach to achieving mode purity, of working below the cutoff frequency of the lowest mode, will not be feasible, an alternative approach involving the use of an array of antennas is devised.

Chapter 4

Antenna Array Design

The previous chapter focussed on the development of a model to describe electromagnetic wave propagation in coaxial waveguides. The dispersion characteristics of the modes of propagation were studied, along with their field distributions, in order to assess the feasibility of using insulated pipelines as a waveguide to enable the inspection of the insulation layer for the presence of water. It was found that for such coaxial waveguides, the frequency range within which only the TEM mode is capable of propagating is severely limited, which would have an adverse effect on the spatial resolution of the inspection technique. Therefore, an approach involving the use of an antenna array was devised. If the array is populated with a number of antennas that is at least twice the number of circumferential cycles of variation in the field distribution of the highest order mode capable of propagating in the excited frequency range, then all of the higher-circumferential-order spurious modes will be suppressed, resulting in pure-mode excitation of the TEM mode.

This chapter will discuss the factors that affect the design of the antenna array, including the type of antenna used, results from a preliminary experiment to assess practical feasibility, methods to improve the impedance match at the antenna, and how the array design will vary with different pipeline specifications. The antenna array approach is presented in a paper in the *Journal of Nondestructive Evaluation*

[P4], and the results from the preliminary experiment are covered in a paper in the QNDE 2009 conference proceedings [P1].

4.1 Monopole Antennas

A common problem in the field of microwave engineering is that of transferring the microwave signal from a coaxial cable into a waveguide. The simplest example of this type of problem is the excitation of a rectangular waveguide with a coaxial cable. Reich [40, p.324] states that this can be achieved with a probe antenna, formed from an extension of the inner conductor of the coaxial cable, oriented parallel to the electric field and located near a point of maximum electric field strength. The probe should be placed a quarter-wavelength from the end of the waveguide, where the end is terminated in a short-circuit, as shown in Figure 4.1, so that waves reflecting from this termination will reinforce the direct waves. Balanis [60, p.384] and Pozar [35, p.208] give further descriptions of this probe antenna technique, whilst Collin [43, p.471] provides an analytical solution to the problem.

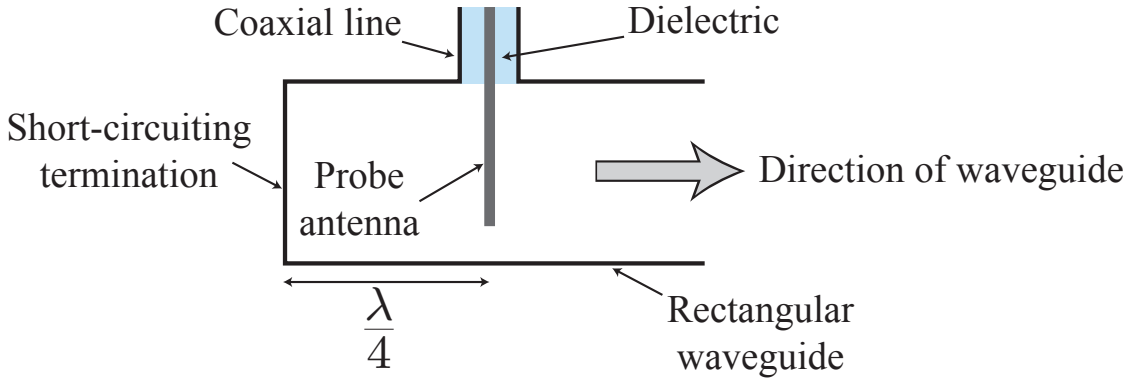

Figure 4.1: Diagram of a junction between a coaxial line and a rectangular waveguide using a probe antenna to couple the electric fields.

The description of simple antennas in Demarest [61, p.595] indicates that this type of probe antenna, formed from an extension of the inner conductor is termed a monopole antenna. Monopole antennas are a form of dipole antenna, in which half of the length of the dipole has been removed and replaced by a ground plane, as shown

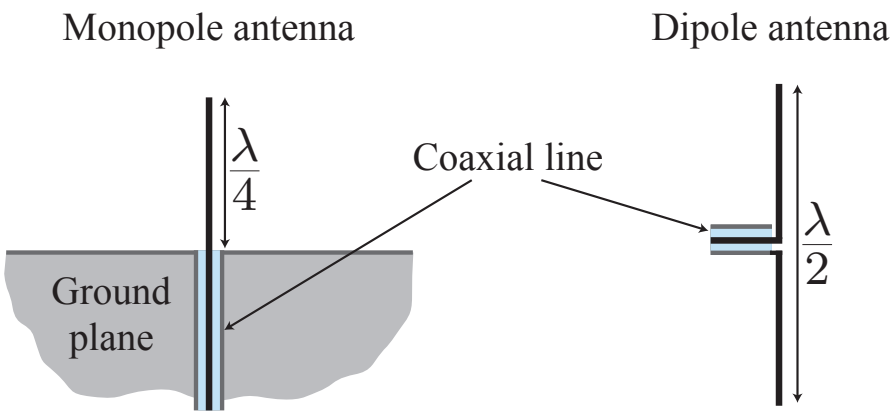

Figure 4.2: Diagram of a monopole antenna and a dipole antenna, which have identical radiation patterns.

in Figure 4.2. Considering the case of a probe antenna in a rectangular waveguide coupling to the electric field, the outer conductor of the coaxial line connects to the wall of the waveguide, forming the ground plane, whilst the inner conductor extends into the waveguide creating a monopole antenna. Monopole antennas are resonant when their length is equal to a quarter-wavelength, therefore it would be expected that a probe antenna in a waveguide would become most effective when its length equals a quarter-wavelength, however, spatial constraints within waveguides may render this resonant length impossible to achieve.

4.2 Preliminary Antenna Array Design

After the initial theoretical feasibility study was conducted, in which the model of coaxial waveguide propagation was developed, a preliminary experiment was performed to determine how well the technique would work in practice. In order to perform this preliminary experiment, an excitation system was required. This excitation system is in the form of an array, for reasons discussed in Chapter 3. As it is the approach set out in the microwave engineering literature (e.g. Reich [40, p.324]), the array was formed from monopole antennas created by extending the inner conductors of the coaxial cables radially towards the inner conductor of the coaxial

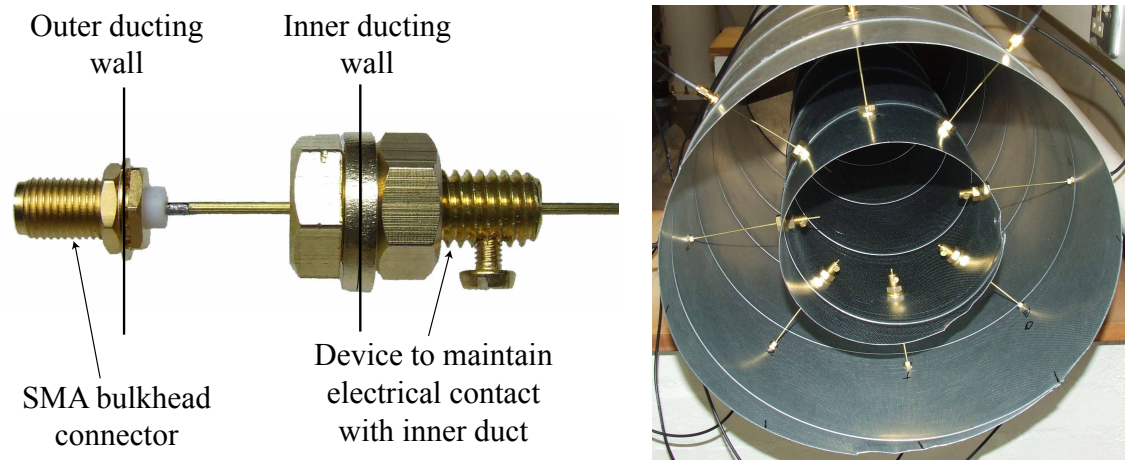

(a) A single preliminary antenna (b) Preliminary antenna array

Figure 4.3: (a) Photograph of the design employed for the preliminary antennas. (b) Photograph of the full array of eight antennas.

waveguide. Reich also states [40, p.326] that the probe is more effective if the antenna is extended fully across the rectangular waveguide, making electrical contact with the other side. Therefore, for the application of this coaxial waveguide array, this approach was adapted by extending the antennas radially across the full annular distance, with an additional device fitted to the inner ducting to maintain good electrical contact of the distal end of the antenna with the inner duct. The antennas were formed by soldering a brass rod with a radius of 0.6 mm to the inner conductor of an SMA bulkhead connector. A photograph of one of these antennas is displayed in Figure 4.3(a), with the complete array displayed in Figure 4.3(b).

Full details of the experimental setup which was used throughout the development of this guided microwave technique will be provided in Chapter 5, therefore, only a minimal description of the setup will be provided here. A Vector Network Analyser (VNA) was used to generate the microwave signal. In order to supply each of the antennas in the array with a microwave signal, a splitter component was used to divide the single channel output from the VNA into the eight channels required for the array. This setup is displayed in a schematic diagram in Figure 4.4; the length of the waveguide used in this experiment was 6 m.

The signal obtained from this setup is shown in Figure 4.5. The x-axis of the data

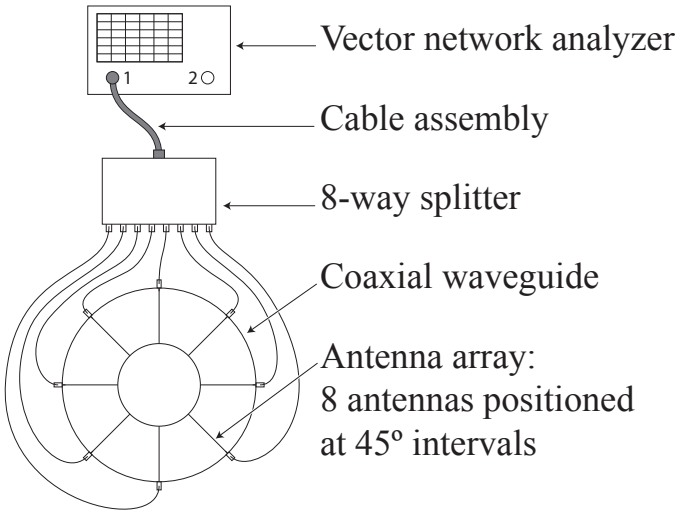

Figure 4.4: Diagram of the experimental setup used in the preliminary experiment. The VNA is connected to the 8-way splitter that divides the signal into the eight channels required to feed the array of eight antennas.

from the TDR calculations performed by the VNA is time; this is converted to the distance travelled by the microwave signal by multiplying by the speed of light in vacuum, c, which is the velocity of propagation of the TEM mode. As the measurements are taken in a reflectometry mode, the distances are also divided by two, so that the x-axis corresponds directly to the position of waveguide features. The small peak at 0 m represents the signal leaving the VNA; the signal with four peaks at approximately 1 m is due to reflections from within the splitter. At 3 m, there is a reflection with a very large amplitude, which is due to the point at which the signal encounters the antenna array within the waveguide. The large reflection is due to the impedance mismatch at this point, which results in significantly reduced transmission of the microwave signal into the waveguide. The peak 6 m later, at 9 m, represents the reflection from the short-circuit termination at the end of the waveguide. The region of noise between 4.5 and 5.5 m has a higher amplitude because it is a reverberation of the splitter signal; it was subsequently found that such reverberations could be removed by suitable calibration of the VNA. Whilst the results from this preliminary experiment indicated the practical feasibility of the method, the signal has a coherent noise level which is too high for it to be used effectively for inspection. The reason for the low SCNR value of 14 dB is the

impedance mismatch at the antenna array, which has the effect of reflecting the incident energy back into the feeding cable system, and only allowing a minority of the energy into the waveguide. This has the combined effect of reducing the amplitude of the desirable signal, and increasing the amplitude of the coherent noise, as the reflected energy reverberates in the feeding cable system. As an indication of the extent of the impedance mismatch, the VNA has an intrinsic impedance of $50\,\Omega$, as do all the coaxial cables used to convey the microwave signal from the VNA to the antennas, whilst the impedance of the coaxial waveguide formed by an insulated pipeline can vary from $62\,\Omega$ down to $4\,\Omega$. A means of quantifying the extent of the effect of the impedance mismatch is to take the amplitude of the reflection from the antennas relative to the amplitude of the reflection from the end of the waveguide, the latter of which is equivalent to the amplitude of the transmitted TEM mode. This Impedance Matching Ratio (IMR) takes a value of 5.67 for this preliminary array. As a consequence of these preliminary results, the need to address the problem of impedance matching was recognised. Therefore, an investigation was conducted into possible methods of matching the impedance of the antenna array to the coaxial cables feeding the array.

4.3 Impedance Matching

4.3.1 Potential Impedance Matching Methods

There are many diverse methods of improving the impedance match between one system and another; some are more suited to certain applications than others. For instance, a method known as *lumped element matching* involves connecting reactive components (capacitors or inductors) either in series with, or in parallel to, the load impedance, in an effort to match the imaginary parts of the impedance [35, p.223]. However, this is a technique which is designed for use in microwave circuit applications, and could not be applied here.

Another technique that can be used is that of the *quarter-wave transformer* [62,

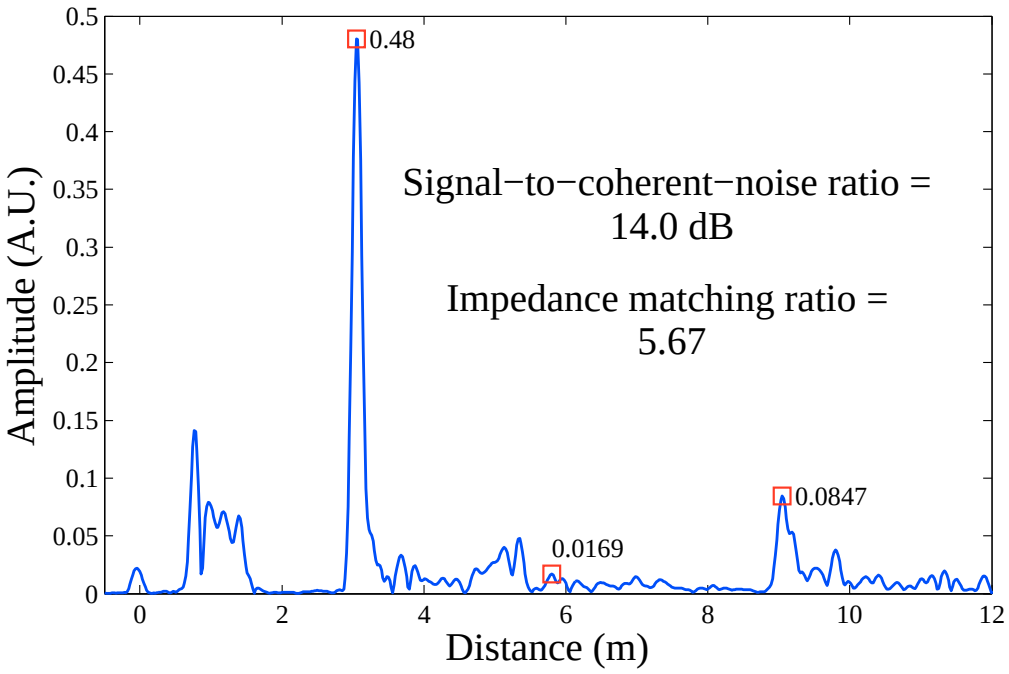

Figure 4.5: The signal from the preliminary antenna design. The signal has a low SCNR due to the poor impedance match at the antennas, which prompted an investigation into possible methods of matching the impedance of the antenna array to the coaxial cables feeding the array.

p.53]. This is used to match a section of transmission line with an impedance, Z_1, to a second section with an impedance, Z_2, by installing an intermediate section of transmission line with a length equal to a quarter-wavelength, and an impedance of $\sqrt{Z_1 Z_2}$. This technique is inherently narrowband, as the length of the matching section is related to the wavelength, and whilst there are more complicated variations on this technique which achieve more broadband matching, none are suited to this application as the presence of the antennas makes our application more complex than simply matching two lengths of transmission line.

A technique which could potentially be used in our application is referred to as *waveguide reactive elements* in [63, p.339]. The method involves introducing metallic elements, in the form of diaphragms, apertures and rods, into the waveguide, which contribute a reactive component to the impedance at that point. However, the reluctance of pipeline operators to permit such intrusions and the complexity of installing such components in the field, renders this technique unfeasible.

Two techniques were unsuccessfully tested in the laboratory. These were *port-matching* and *triple-stub tuners*. Port-matching [64, 65] is a software feature of the VNA which allows the effect of reactive circuit components (capacitors and inductors, as in the lumped element method described above) to be mathematically embedded into the frequency domain responses measured by the instrument. Calibration of the instrument at the ends of the cable which connects to the antenna moves the reference plane of the VNA to this point, allowing these matching elements to be embedded next to the antenna, facilitating the matching process. The second technique which was tested was the use of a triple-stub tuner [63, p.317], which is a piece of hardware that is comprised of three lengths of transmission line (stubs) and is connected in between the coaxial line and the antenna. The lengths of the three stubs can be varied to adjust the reactive contributions from each of the stubs in order to achieve an impedance match. Both techniques were tested experimentally, for a range of bandwidths about a constant centre frequency of 955 MHz. In both cases it was found that the techniques were able to achieve a good impedance match when the frequency range was narrow, but the performance of the techniques suffered drastically as the bandwidth was increased to the 2 GHz required by this guided microwave technique. Therefore, an alternative impedance matching method was sought.

4.3.2 Impedance Matching with Antenna Design

Reich [40, p.325] warns of the difficulty of matching the impedance of the coaxial line to the rectangular waveguide over a wide frequency range, but suggests that the impedance mismatch problem can be somewhat alleviated through proper choice of probe length, and position relative to the closed waveguide termination; with the optimum arrangement most readily determined through experimentation. Reich also states that the impedance match can be improved by adjusting the radius of the probe antenna to an optimum value relative to the width of the rectangular waveguide. Achieving an impedance match through the design of the antenna itself would be the ideal solution to this problem, as it would not require any additional

components in the setup or any additional intrusions through the pipeline cladding into the insulation.

The potential of this technique to improve the impedance match of an antenna in a waveguide was investigated initially with simple experiments involving a single probe antenna exciting a rectangular waveguide, full details of which can be found in Appendix A. The experimental results demonstrated that the technique was very effective in improving the impedance match at the antennas, achieving a reduction in the IMR from 470 to 0.22, by finding the optimum length and radius for the antenna rod. The results were compared to simulations performed in Microwave Studio, and were found to be in very good agreement. This provides validation for the accuracy of the software in simulating the behaviour of antennas radiating within waveguides, which is crucial for the continued use of the software in the development of an antenna array for the excitation of large coaxial waveguides.

4.4 Simulations to Optimise Antenna Array

Experiments with a single antenna in a rectangular waveguide demonstrated the effectiveness of impedance matching through the design of the antenna. In order to use this method of impedance matching on the coaxial waveguide antenna array, a method of obtaining the optimum antenna design is required. An experimental approach would require fabricating eight antennas of each design, which would be prohibitively time-consuming. Consideration of an analytical approach to calculating the optimum design highlights the complexity of the excitation of large coaxial waveguides with a monopole antenna, particularly in the near-field where evanescent modes have to be considered. Relevant literature [66, 67] only studies the case of a single antenna in the waveguide. The situation becomes increasingly complicated with the introduction of additional antennas into the array, due to mutual coupling between antennas. Due to this complexity analytical solutions cannot be relied upon for optimising the antenna design. Therefore, as the performance of the simulation software has been validated by comparison with the experimental

results in rectangular waveguide, numerical simulations will be performed to study the effect of varying antenna parameters on the impedance match at the array, in order to optimise the antenna design.

4.4.1 Methods for Using MWS to Simulate an Antenna Array

The Microwave Studio software employs a hexahedral grid to mesh the structure, with the planes of this grid aligned along the Cartesian axes. The simulation of a coaxial waveguide involves components with circular cross-sections, not easily described by a hexahedral mesh. It might be expected that this would lead to inaccurate simulations, however, this is not the case, as the software is capable of implementing a perfect boundary approximation [68] of curved surfaces. Using this perfect boundary approximation, the hexahedral mesh does not attempt to conform to a curved surface, instead, sub-cellular information from partially filled elements is taken into account in order to accurately simulate the curved surface.

In MWS, the source of the simulation excitation is defined by setting waveguide ports on the face of a component. The software determines the field distributions of the modes that can exist for the cross-section of the component at which the waveguide port was created. The user selects the mode that will be input into the model, and this field distribution is then used, in conjunction with the user-supplied frequency range, to calculate the excitation signal to be applied at the waveguide port. The use of a hexahedral grid imposes a limitation on these waveguide ports: they have to be aligned with a Cartesian axis plane. This causes difficulties when modelling an array of antennas. An array with two or four antennas can achieve suitable alignment, however, arrays with six or more antennas cannot be aligned in this manner. This difficulty was overcome by creating additional cable components feeding each antenna to enable a 90° bend to be introduced, thus allowing all waveguide ports to be aligned with the x-y plane, as shown in Figure 4.6, which displays an array with six antennas; the lowest number that requires this approach

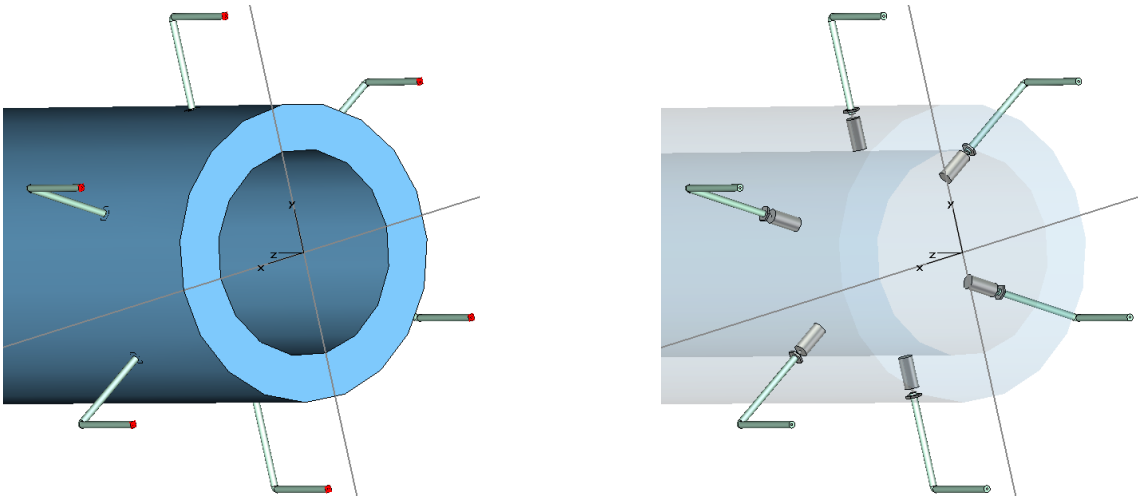

(a) Waveguide and feeding cables (b) Antenna array

Figure 4.6: Model of a six-antenna array used to excite a large coaxial waveguide formed from an annular vacuum component in blue within a perfectly electrically conductive background material. The feeding cables incorporate a 90° bend in order to align the waveguide ports (red squares) with the x-y plane.

for the model to function. Simulations were performed to ensure that the bends in the feeding cables did not effect the results.

The simulation software enables the user to define the background material. For all simulations, the Perfect Electrical Conductor (PEC) material was chosen as the background material. Most models involved creating components from vacuum material, as this has electromagnetic properties which are effectively identical to air. For example, to model the large coaxial waveguide formed by a pipe, the background material is set to PEC, and then a single annular component is constructed from vacuum with its inner and outer radii defining the dimensions of the annular space occupied by the pipe's insulation. The use of PEC makes the assumption that the conductivity of the pipe and cladding materials is sufficiently high that it can be considered to be infinite, whilst the use of vacuum to model the insulation's annulus makes the assumption that the insulation has a relative permittivity, $\epsilon_r = 1$, and is not lossy. These are the same assumptions used in the development of the coaxial waveguide model, discussed in Section 3.1. The results from this software were carefully validated against published work [69, 70], and experimental results, at all

stages, to ensure that the assumptions made in the choice of material properties were not leading to inaccurate simulations.

4.4.2 Optimisation of Antenna Design

To optimise the design of the antennas in an array exciting a waveguide with dimensions of $a = 157.5\,\text{mm}$ and $b = 80\,\text{mm}$, the approach that was adopted initially was to perform a parameter sweep of the length of the antenna rod, to find the optimum length. Subsequently, a parameter sweep of the radius of the rod was conducted, to find the optimum radius. However, it became apparent that this method would not lead to the overall optimum design as the two parameters affect each other. Therefore, a two-dimensional parameter sweep was conducted of antenna length and radius. The IMR calculated for each of these designs was plotted as a surface, as shown in Figure 4.7(a). Further parameter sweeps focussing on a narrower region of interest were conducted to fine-tune the optimum design, resulting in an optimum length of 0.89 of the annular distance, equal to 63.8 mm, and an optimum radius of 5.57 mm.

The disadvantage of performing a two-dimensional parameter sweep is the high computational cost, the plot in Figure 4.7(a) required the simulation of 420 different models, with each model taking approximately 23 min. As the optimum antenna design is dependent on the pipeline specification, in order to determine the optimum design for each of these specifications, a more efficient approach was required. The surface plotted in Figure 4.7(a) has a smooth gradient, with no local minima, as such it lends itself to the use of the pattern search optimisation algorithm [71]. An example of the results of running the algorithm to find the optimum antenna design for a waveguide with the same dimensions of $a = 157.5\,\text{mm}$ and $b = 80\,\text{mm}$ is displayed in Figure 4.7(b). The algorithm required only 99 simulations to converge on the minimum of the IMR, a significant saving (5 days) in computational expense. This approach has the additional advantage of resulting in a more accurate optimum design than a two-dimensional parameter sweep, as the accuracy of the latter approach is limited by the sampling discretisation of the parameters.

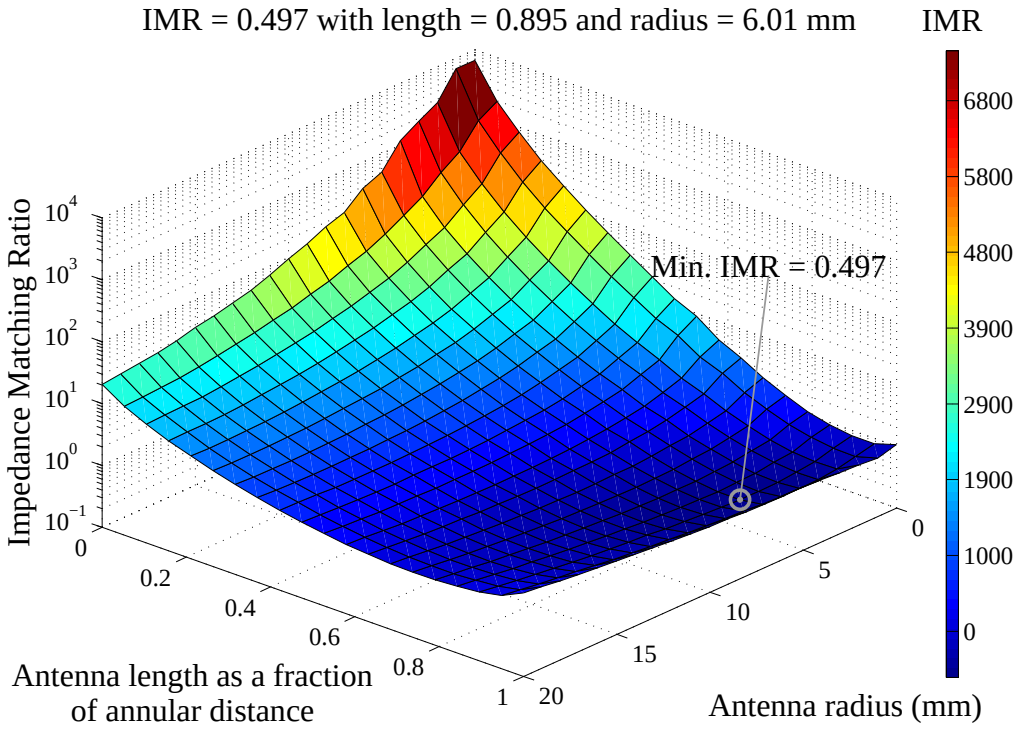

(a) Two dimensional parameter sweep

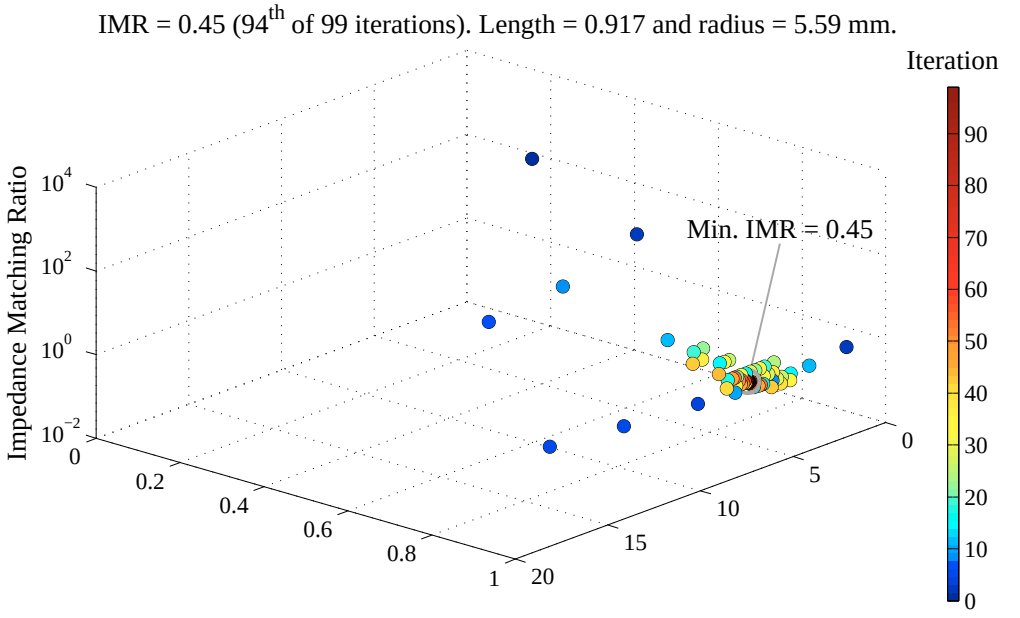

(b) Optimisation routine

Figure 4.7: Methods used to optimise the design of the antenna array: (a) displays the results of the initial approach, a two dimensional parameter sweep; (b) displays the results using the pattern search optimisation algorithm, which yields more accurate results and a 76 % saving in time.

4.5 Array Designs for Various Pipeline Specifications

In order to use the technique on the wide variety of pipeline specifications that are used industrially, the optimum antenna design would need to be known for each specification. The pipeline diameters of interest are listed in Table 4.1 in terms of their nominal pipe size, and the actual outer diameter that this corresponds to in inches. In addition, the third column displays the number of antennas required in the array to achieve pure-mode excitation of the TEM mode in a waveguide formed by a pipeline with this diameter. For each of these pipe diameters, insulation thicknesses of 1, 2, 3, and 4" were investigated, by performing an optimisation of the antenna design for that pipeline specification, with the number of antennas in the array determined by the pipe diameter, as described in Table 4.1. The optimum designs for each pipe diameter and insulation thickness are specified in Table 4.2 and plotted in Figure 4.8.

From Figure 4.8, it can be seen that there are clear trends in the optimum length and optimum radius of the antenna rods. For each insulation thickness, the optimum length and radius appears to be relatively constant as the pipe diameter is

Table 4.1: Table listing the pipeline diameters for which optimum antenna designs were obtained, accompanied by the number of antennas required in each case.

Pipe Diameter (NPS)	Pipe Diameter (")	Number of antennas required
4	4.5	6
6	6.625	8
8	8.625	10
12	12.75	14
18	18	20
24	24	24

Table 4.2: Table giving the optimum antenna designs, in terms of the optimum length (as a fraction of the annular distance), optimum radius, and resultant IMR, for pipes with diameters of 4, 6, 8, 12, 18, and 24" and insulation thicknesses of 1, 2, 3, and 4".

Pipe diameter (")	Insulation thickness (")	a (mm)	b (mm)	Z_0 (Ω)	Optimum length (fraction)	Optimum radius (mm)	IMR
4.5	1	82.55	57.15	22.05	0.9864	5.680	0.2448
4.5	2	107.95	57.15	38.13	0.9981	3.548	0.5009
4.5	3	133.35	57.15	50.80	0.8785	6.516	0.4560
4.5	4	158.75	57.15	61.26	0.8321	8.473	0.4835
6.625	1	109.54	84.14	15.82	0.9933	5.969	0.2957
6.625	2	134.94	84.14	28.32	0.9929	2.061	0.5514
6.625	3	160.34	84.14	38.66	0.8902	6.395	0.5030
6.625	4	185.74	84.14	47.48	0.7994	8.469	0.5884
8.625	1	134.94	109.54	12.50	0.9943	4.504	0.2407
8.625	2	160.34	109.54	22.85	0.9910	3.902	0.5158
8.625	3	185.74	109.54	31.66	0.8814	6.620	0.5892
8.625	4	211.14	109.54	39.35	0.8044	8.438	0.5386
12.75	1	187.33	161.93	8.74	0.9900	5.969	0.2048
12.75	2	212.73	161.93	16.36	0.9900	4.125	0.5993
12.75	3	238.13	161.93	23.12	0.8531	7.688	0.6392
12.75	4	263.53	161.93	29.20	0.8238	8.464	0.6130
18	1	254.00	228.60	6.32	0.9857	4.953	0.2686
18	2	279.40	228.60	12.03	0.9935	2.426	0.5648
18	3	304.80	228.60	17.25	0.8727	5.773	0.7043
18	4	330.20	228.60	22.05	0.7940	11.031	0.7075
24	1	330.20	304.80	4.80	0.9934	4.992	0.2288
24	2	355.60	304.80	9.24	0.9989	3.242	0.5665
24	3	381.00	304.80	13.38	0.8473	8.279	0.6988
24	4	406.40	304.80	17.25	0.7594	9.938	0.6805

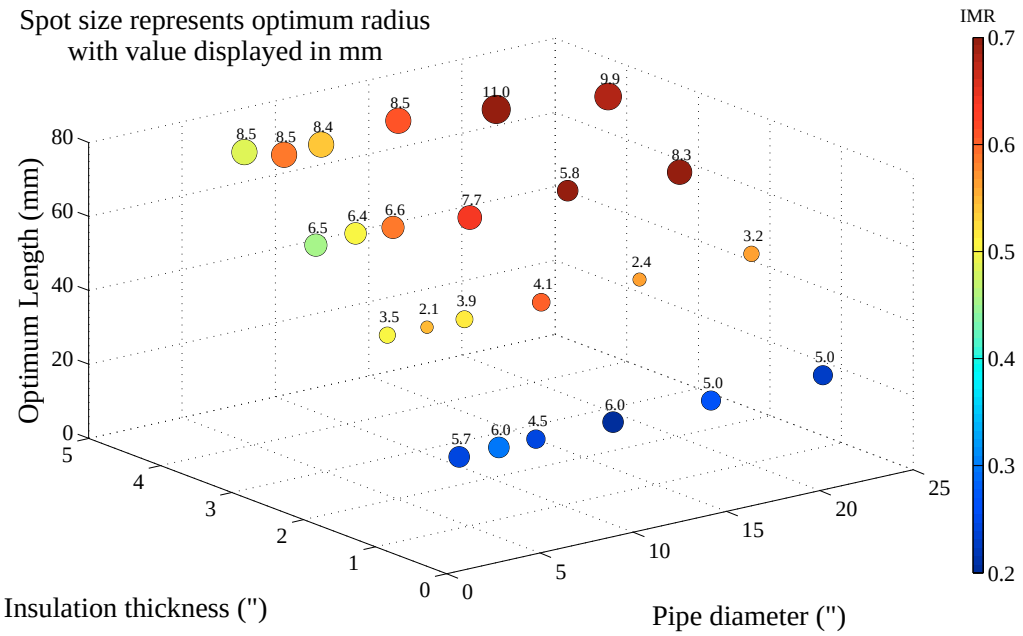

Figure 4.8: Figure displaying the optimum antenna designs for pipe diameters of 4, 6, 8, 12, 18, and 24" and insulation thicknesses of 1, 2, 3, and 4". The optimum length is displayed on the z-axis, the optimum radius is denoted by the size of the spot, with the value given in mm above the spot, and the IMR of the antenna is given by the colour of the spot.

increased. This is beneficial for the practical implementation of the technique, as it means that a different antenna design is only required for each different insulation thickness. Therefore, a facility which uses 1, 2, 3, and 4" insulation thicknesses on its pipes, would require only four different antenna designs, with the diameter of the pipe determining the number of antennas (as specified in Table 4.1) to be installed. Whilst greatly simplifying the implementation of this technique, such an approach would involve a compromise in the efficiency of the excitation arrays, as they would no longer be optimally matched for each individual situation. Whether the compromise can be tolerated without experiencing excessive adverse effects on the excitation array, in order to benefit from this simpler installation approach would require further simulation work.

4.6 Summary

In the previous chapter, the use of an array of antennas was proposed in order to achieve pure-mode excitation of the TEM mode. In this chapter, the array of antennas was designed. This design process began with a review of the type of antennas that are used for this type of application, followed by the fabrication of an array based on an adaption of antennas described in the literature for a preliminary experiment to test the excitation of a large coaxial waveguide.

Whilst this preliminary experiment indicated the practical feasibility of the technique, the SCNR was low due to the impedance mismatch at the antennas, resulting in only a sixth of the incident signal energy being transmitted into the waveguide. This prompted an investigation into potential methods of improving the impedance match. Some of these methods were discounted due to their inapplicability to this situation. Two methods were assessed experimentally, and whilst they managed to improve the impedance match at narrow bandwidths, they were both incapable of impedance matching when the bandwidth was increased to that required by this technique.

Subsequently, a test was conducted of a method of impedance matching through altering the design of the antenna itself, by performing simulations and experiments of the simple case of a single antenna exciting a rectangular waveguide. The results demonstrated that the length and diameter of the antenna had a very significant effect on the impedance match, therefore, this method was investigated for the more complicated situation of the antenna array exciting a large coaxial waveguide. Simulations were performed to optimise the length and diameter of the antenna rods in the array. It was found that the pattern search optimisation routine could be employed to find the optimum design with greater speed and accuracy than with a two-dimensional parameter sweep of length and radius.

The optimisation routine was then employed to find the optimum antenna designs for a wide variety of pipeline specifications (pipe diameters and insulation thicknesses). It was found that the same antenna design could be used for a particular

insulation thickness irrespective of the diameter of the pipe (although more antennas are required for larger pipes), which simplifies the practical implementation of this guided microwave technique.

Chapter 5

Experimental Validation of the Technique

The previous chapter presented results which were obtained from a preliminary experiment to assess the practical feasibility of this guided microwave technique. Whilst the results confirmed the feasibility of the approach, the transmission of energy from the antenna array into the waveguide was poor. This was due to a significant impedance mismatch at the antennas. The chapter discussed the use of the simulation software to optimise the design of the antenna to improve the impedance match between the coaxial feeding cables and the antennas within the coaxial waveguide. The results demonstrated that the length and diameter of the metallic rod forming the antenna had a very significant effect on the impedance match. By simultaneously varying both of these parameters in a simulation of the antenna array in a coaxial waveguide, the optimum design of the antenna for various typical pipeline specifications was obtained.

This chapter begins with a description of the experimental setup used throughout the development of this technique. The first experiments performed with this setup were to validate the simulated results for optimum antenna designs, by using these designs to excite propagation in two waveguides of different sizes. The experimental setup was also used to validate the approach of using an antenna array by comparing

the signal obtained from exciting only a single antenna with the signal obtained from exciting the full array of eight antennas. In addition, experiments were performed to measure the attenuation of the microwave signal due to the presence within the waveguide of different types of insulation that are commonly used in industry. Finally, in order to have confidence that the model experiments performed in the laboratory are representative of the conditions which exists on industrial pipelines, validation is sought by performing a field test on a section of real industrial insulated piping.

The validation of the simulated optimum antenna designs was reported in the QNDE 2010 conference proceedings [P2], and in a paper in the *Journal of Nondestructive Evaluation* [P4]; the latter of which also discussed the validation of the array approach. The field test validation of the model laboratory experiments will be presented in a paper submitted to the journal *Insight* [P6].

5.1 Experimental Setup

The experimental setup used throughout the development of this technique employed ventilation ducting to represent a 6" pipe with 3" insulation, as shown in Figure 5.1. This ducting was formed from spirally wound galvanised steel sheet, and was purchased from Lindab [72]. The outer duct had a diameter of 315 mm, and the inner duct had a diameter of 160 mm, with wall thicknesses of 0.6 mm and 0.5 mm, respectively. These ducting dimensions produce a coaxial waveguide with $a = 157.5$ mm and $b = 80$ mm. The length of the waveguide formed by this ducting was 3 m, and each end of the waveguide was terminated in a short-circuit formed by a metallic end-cap. From an electromagnetic point of view, a coaxial waveguide formed from ducting should be almost identical to that formed by a real pipeline, as the thickness of the conductors is irrelevant due to the extremely small skin depth at microwave frequencies, as discussed in Section 3.1.2. Initial experiments were conducted with no insulation in the annular volume between the pipe and the cladding,

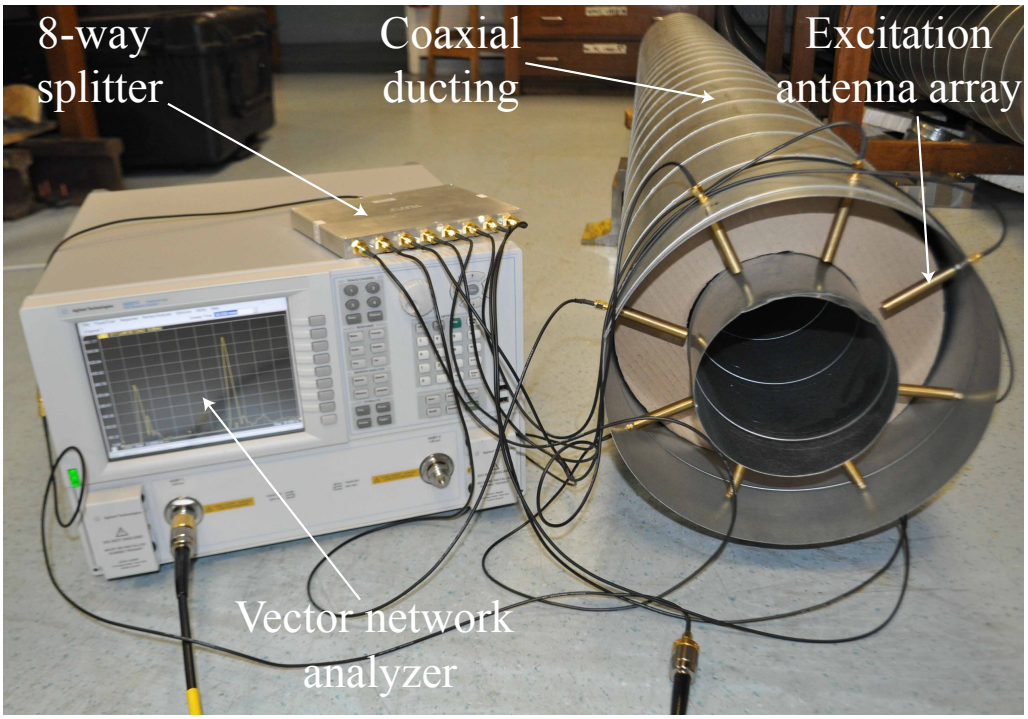

Figure 5.1: Photograph of the experimental setup used in the laboratory. Coaxially aligned lengths of ventilation ducting with $a = 157.5\,\text{mm}$ and $b = 80\,\text{mm}$ are used to represent a 6" pipe with 3" insulation.

however, the effect of insulation is investigated experimentally in Section 5.4. A Vector Network Analyser (VNA) from Agilent (model E8361C with a frequency range from 10 MHz to 67 GHz) was used to generate the microwave frequency signal. The VNA has 2 ports and can be used to record the 2-port scattering parameter matrix as a function of frequency, although only 1 port is used for the type of pulse-echo measurements conducted here. From this frequency-domain data, TDR is used to calculate the signals in the time-domain. The VNA is capable of performing these TDR calculations in real-time, so that the position of features within the waveguide can be monitored in real-time. For the waveguide dimensions formed by the ducting, the cutoff frequency of the TM_{02} mode occurs at 1.923 GHz, and it is this cutoff frequency that defines the upper limit of the frequency range, as explained in Section 3.4. Consequently, a maximum operating frequency of 1.9 GHz is selected, whilst the minimum operating frequency is defined by the minimum frequency of the VNA: 10 MHz. Within this operating frequency range, there are four modes of the TE_{p1} mode family capable of propagating, therefore eight antennas are required for the

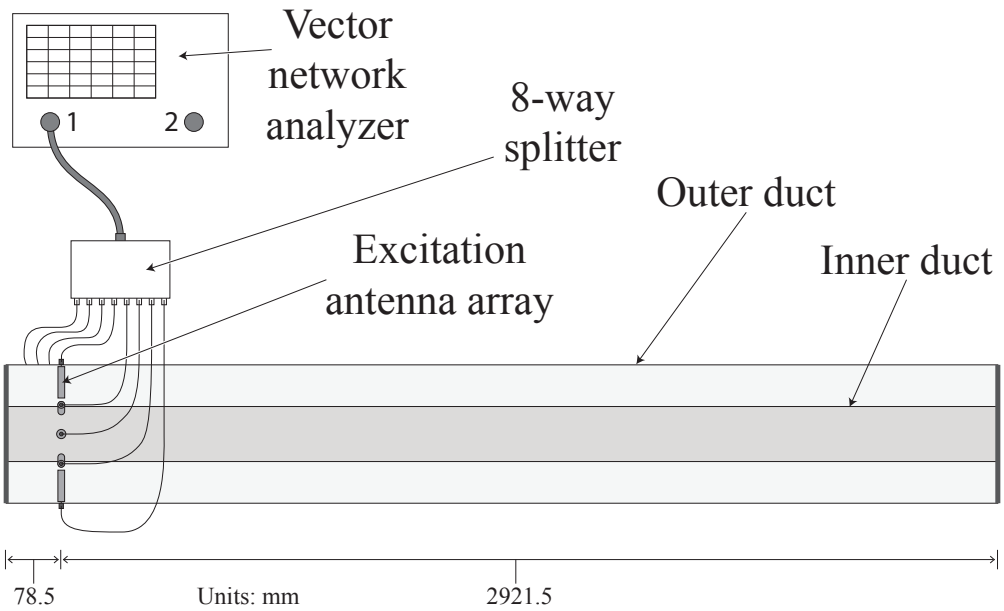

Figure 5.2: Schematic diagram of the experimental setup used in the laboratory. The waveguide is formed from an inner duct aligned coaxially within the outer duct, both with a length of 3 m, and with short-circuiting metallic end-caps fitted to both ends. A vector network analyser generates the microwave signal; an 8-way splitter divides the single channel into the eight required for the array; eight cables of equal length (in order to preserve equality of phase) connect the splitter outputs with the antennas of the array. The antennas are positioned $\lambda_m/4 = 78.5\,\text{mm}$ from the proximal short-circuiting termination, for constructive interference.

array to be effective. The array employed in the experiment was configured with these eight antennas arranged about the circumference at 45° intervals, as shown in Figure 5.1. To admit the antennas, holes were drilled in the appropriate positions in the outer ducting. An 8-way splitter was required in order to split the single channel from port 1 of the VNA into the eight channels required to excite each antenna in the array, and also to recombine the reflected signals. The splitter used was obtained from ETL systems (model COM08L1P-2508). The splitter was connected to the antennas by means of eight SMA cables of equal length, in order to preserve equality of phase in each of the channels. The antenna array was positioned a quarter-wavelength from the short-circuiting end-cap for constructive interference in the desired direction of propagation. Wavelength is frequency dependent ($\lambda = c/f$), therefore, the centre frequency, $f_m = 955\,\text{MHz}$, is used, giving a centre wavelength

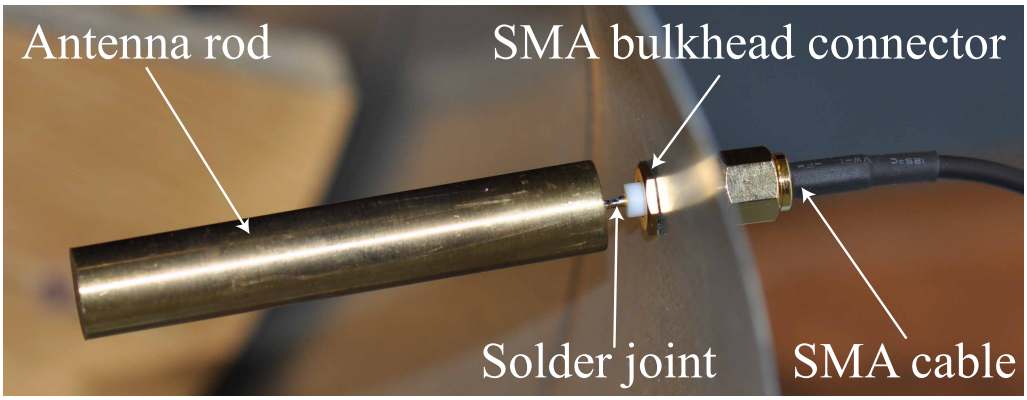

Figure 5.3: Photograph of the antenna fabricated according to the simulated optimum design for a coaxial waveguide with $a = 157.5\,\text{mm}$ and $b = 80\,\text{mm}$.

of $\lambda_m/4 = 78.5\,\text{mm}$. A schematic diagram of this experimental setup is displayed in Figure 5.2.

The optimum antenna design for a coaxial waveguide with $a = 157.5\,\text{mm}$ and $b = 80\,\text{mm}$ was obtained from simulations, as described in Section 4.4.2. The optimum design was a length of 0.89 of the annular distance, equal to 63.8 mm, and a radius of 5.57 mm. A photograph of one of these antennas is displayed in Figure 5.3. The antenna rods were fabricated from brass, which was machined to the appropriate dimensions; this antenna rod was then soldered to the SMA bulkhead connector.

An additional coaxial waveguide was set up to represent a pipe with thinner insulation; this was formed from the same type of ducting as in the first setup, with the same inner duct with a diameter of 160 mm, but a different outer duct with a diameter of 280 mm. This arrangement gives cross-sectional dimensions for this coaxial waveguide of $a = 140\,\text{mm}$ and $b = 80\,\text{mm}$, approximately equivalent to a 6" pipe with 2" insulation. The optimum design for this waveguide was determined to be a length of 0.993 of the annular distance, equal to 44.6 mm, and a radius of 4.5 mm. The type of antenna which is used throughout the development of this guided microwave technique is a prototype design, which is required to be installed from the inside of the cladding. This can create a problem for antennas which are long relative to the annular distance, such as this optimum length of 0.993. This

means that there would not be sufficient space to introduce the antenna and install it into its hole in the cladding. Therefore a 1 mm reduction in the length to 43.6 mm was incorporated into the antenna design, which was then fabricated.

5.2 Experimental Results from Optimised Array

The signal obtained from the optimised antenna array for a coaxial waveguide with $a = 157.5$ mm, $b = 80$ mm, equivalent to a 6" pipe with 3" insulation, is displayed in Figure 5.4. The antenna reflection appears at 0 m, with the end reflection occurring at 3 m. It can be seen that the level of noise in between these two reflections is dramatically reduced in comparison to the signal displayed in Figure 4.5. This is quantified by the value of the SCNR, for which the preliminary array achieved 14.0 dB, whilst this optimised array achieves 39.4 dB, which is a significant improvement. The IMR value, which quantifies the extent of the impedance mismatch, is also significantly improved with a reduction from 5.67 to 0.525.

The signal from the optimised array for a coaxial waveguide with $a = 140$ mm and

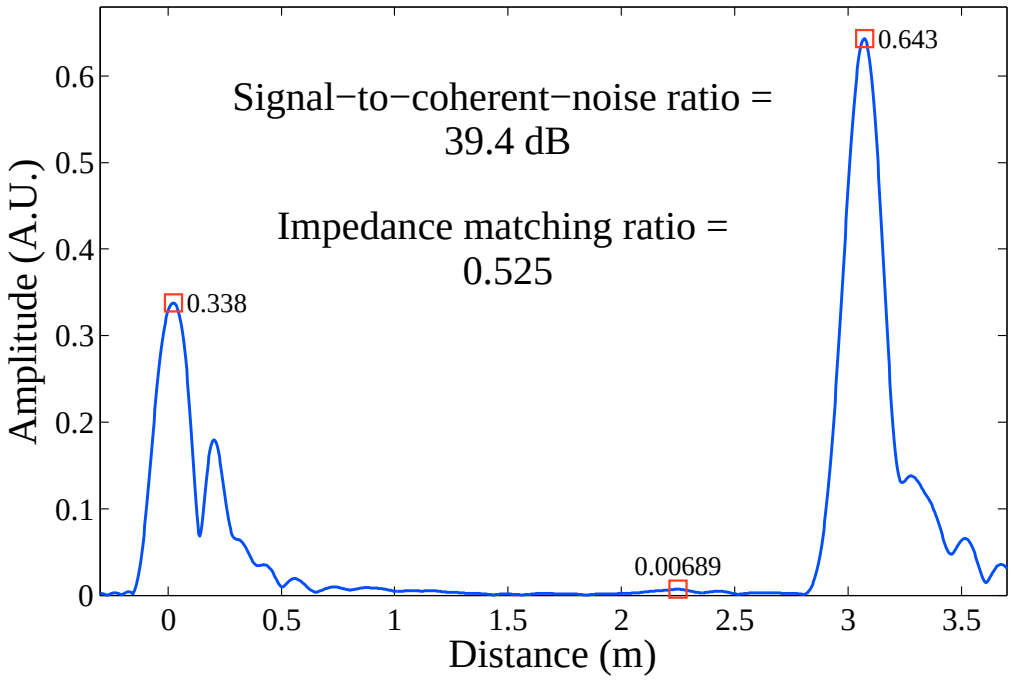

Figure 5.4: Signal from the ducting equivalent to a 6" pipe with 3" insulation.

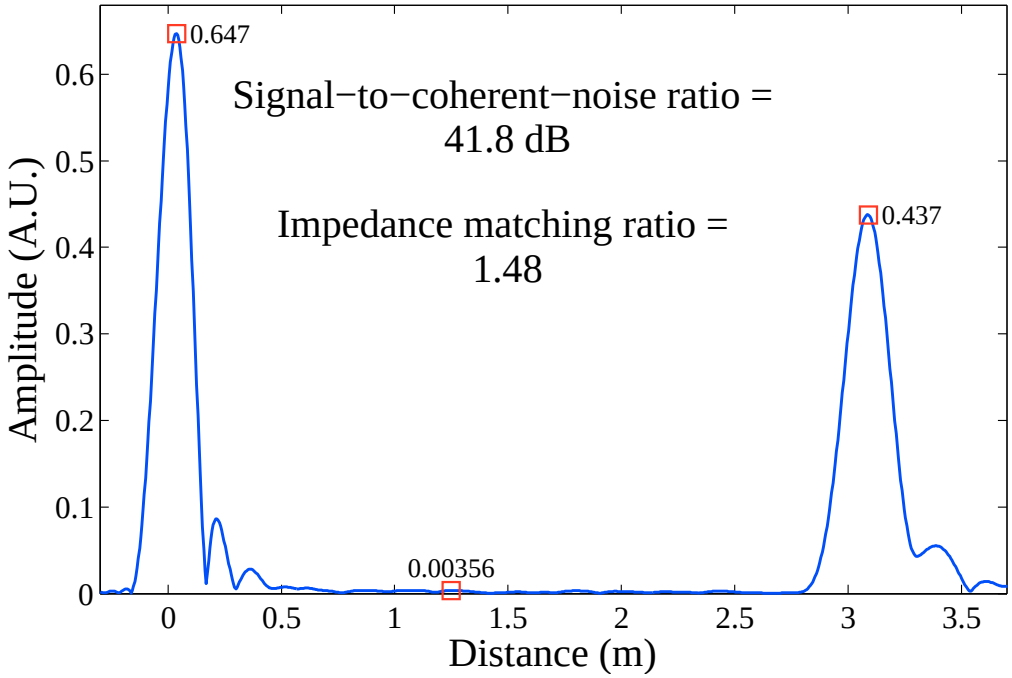

Figure 5.5: Signal from the ducting equivalent to a 6" pipe with 2" insulation.

$b = 80\,\text{mm}$, equivalent to a 6" pipe with 2" insulation, is displayed in Figure 5.5. It can be seen that the IMR of this signal is not quite as good as in Figure 5.4 with a value of 1.48 compared to 0.525. This is due to the necessity to make the antenna shorter than the optimum design due to spatial constraints within the waveguide. Despite the relatively high IMR, the SCNR of this signal is very good, with a value of 41.8 dB. The excellent results obtained from these two experiments provide validation for the use of the Microwave Studio simulation software to optimise the design of the antennas.

5.3 Validation of Array Approach

The use of an array is a fundamental aspect of the design of the excitation system; as such, the array approach warrants validation. This validation was sought by performing an experiment involving the ducting with $a = 157.5\,\text{mm}$ and $b = 80\,\text{mm}$, in which a signal was recorded with only a single antenna exciting the waveguide,

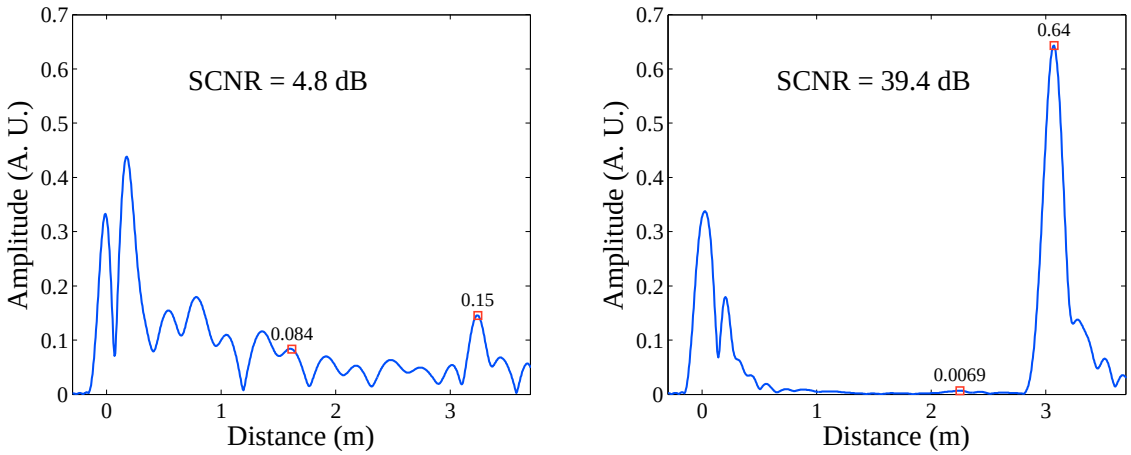

(a) Signal from a single antenna

(b) Signal from eight antenna array

Figure 5.6: Comparison of signals obtained with a single antenna and a complete array of eight antennas. The improvement in the SCNR with the use of an array provides validation for the array approach used in the excitation system.

followed by a signal recorded with all eight antennas in the array being used for excitation. These two signals are displayed in Figure 5.6.

Figure 5.6(a) displays the signal from only a single antenna. It is apparent that there is a lot of coherent noise in this signal, which is quantified with a SCNR of 4.8 dB. This coherent noise is due to the propagation of the unsuppressed modes of the TE_{p1} mode family, which experience interference effects as they propagate. Figure 5.6(b) displays the signal with excitation from the array of eight antennas. This equates to an increase in the SCNR by a factor of 52, and demonstrates the effectiveness of the excitation system, providing experimental validation for the array approach.

5.4 Effect of Insulation

There are two main mechanisms which attenuate the propagation of guided electromagnetic waves. The first of these was mentioned in Section 3.1.2, and is due to the metal which forms the waveguide walls. The magnetic field of the propagating electromagnetic wave induces surface currents which flow in the walls of the waveguide,

these currents experience resistance due to the finite value of the conductivity of the wall material, and this attenuates the passage of electromagnetic waves. The conductivities of the materials from which the pipe and cladding are constructed are high, the values for typical pipeline materials are given in Table 3.1, lying in the range between $1.6 \times 10^6\,\mathrm{S\,m^{-1}}$ and $42 \times 10^6\,\mathrm{S\,m^{-1}}$. Since these pipe materials have high conductivities, then this first form of attenuation is minimal. The second attenuation mechanism is due to the material filling the waveguide and is linked to the interaction of electromagnetic waves with water, which will be discussed in more detail in Section 6.1. The oscillating electric field of the electromagnetic wave causes any polar molecules within the material filling the waveguide to undergo rotation to match the field alignment, which dissipates energy into the material, and attenuates

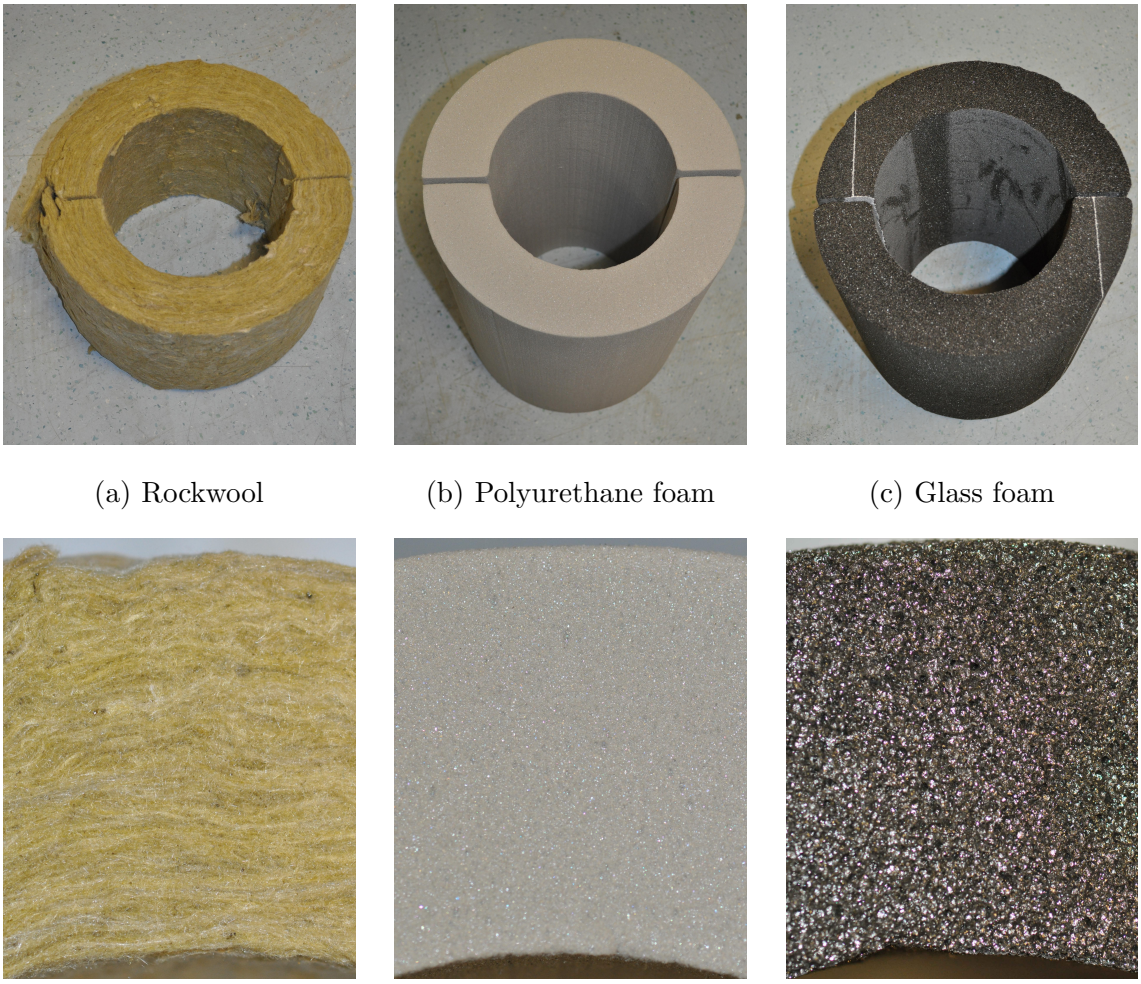

(a) Rockwool (b) Polyurethane foam (c) Glass foam

Figure 5.7: Photographs of three of the main insulation types used industrially: (a) rockwool, (b) polyurethane foam, (c) glass foam.

the electromagnetic wave. As the first attenuation mechanism is minimal, the range of this guided microwave inspection technique will be limited by the attenuation of the insulation materials. As such, the measurement of the attenuation of insulation materials that are commonly used industrially is of great relevance to the practical value of the technique.

These insulation attenuation measurement experiments were all performed using ducting forming a coaxial waveguide with $a = 140\,\text{mm}$ and $b = 80\,\text{mm}$. Due to the differences in the attenuation of the insulation materials, the measurement techniques varied slightly, with low attenuations requiring longer lengths of insulation material in order to obtain an attenuation of the signal which was measurable.

Photographs of samples of three of the main types of insulation that are used industrially are displayed in Figure 5.7: rockwool, polyurethane foam, and glass foam.

5.4.1 Rockwool Insulation

Rockwool is a type of insulation formed from fibres of volcanic diabase rock [73] that is widely used on pipelines at high temperatures. It is hydrophobic over the short-term, with water running off its surface, however, if immersed in water for a period of 7-14 days, it will become saturated, gaining up to ten times its weight in water. The density of rockwool is typically in the region of $120\,\text{kg}\,\text{m}^{-3}$, and it has a thermal conductivity of approximately $\kappa = 0.039\,\text{W}\,\text{m}^{-1}\,\text{K}^{-1}$ [73].

The experiment to measure the attenuation of rockwool involved a waveguide with a length, l, of 6 m. An initial signal was recorded with no insulation present inside the waveguide. Subsequently, the entire length of the waveguide was filled with rockwool insulation, purchased from PAR Group [74], in the form of tubular half-shells with an inside diameter of 170 mm and an outside diameter of 270 mm, in order to fit within the coaxial waveguide. The signal from the insulated waveguide was then recorded, and is plotted alongside the empty waveguide signal in Figure 5.8.

The signals are normalised to the amplitude of the antenna reflection at 0 m. The

reduction in the amplitude of the end reflection with the introduction of the insulation is due to the attenuation of the insulation material. The amplitude of the end reflection from the uninsulated waveguide, A_1, and the amplitude of the end reflection from the insulated waveguide, A_2, can be used to determine the attenuation coefficient, α, using the equation

$$\alpha = \left(\frac{20}{l}\right) \log_{10} \left(\frac{A_1}{A_2}\right). \tag{5.1}$$

This gives an attenuation for rockwool of $\alpha = 0.21\,\mathrm{dB\,m^{-1}}$. It should be noted that since the length used in the attenuation calculation is 6 m (the physical length of the waveguide) rather than 12 m (the distance travelled by the signal), the attenuation coefficient takes into account the loss experienced during the return journey; as such it would more accurately be termed the *pulse-echo* attenuation coefficient.

As with previous signals, the x-axis of the figure, displaying distance, is calculated using c as the velocity of propagation of the TEM mode in air. However, the TEM mode is no longer travelling in air; there is a dielectric material within the waveguide. From Figure 5.8, it can be seen that the reflection from the end of the waveguide is delayed in its arrival by the introduction of the rockwool insulation.

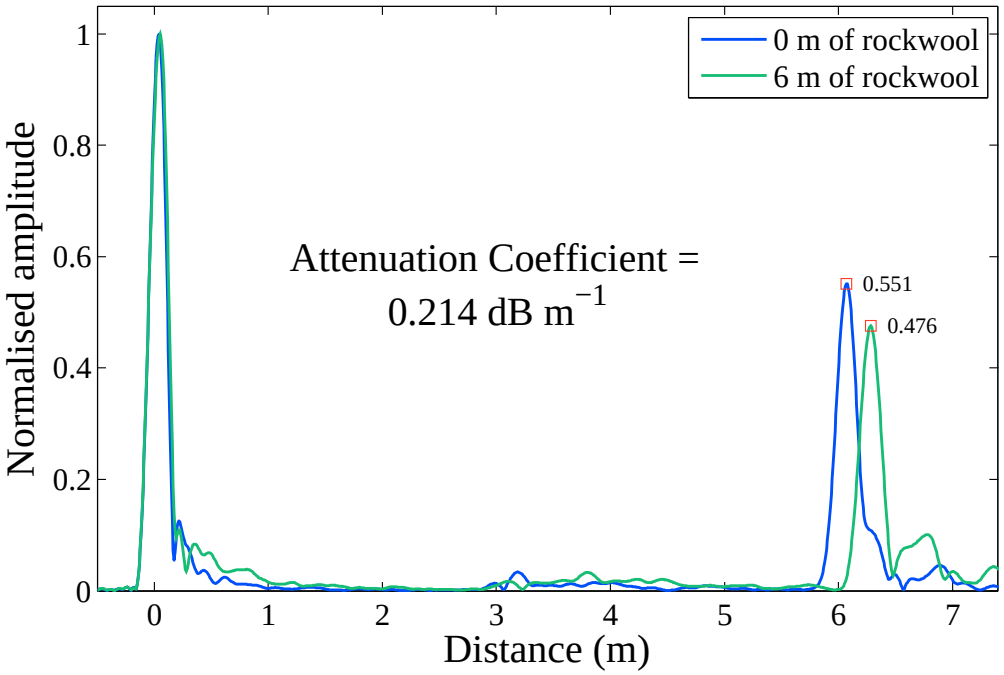

Figure 5.8: Signals measuring the attenuation of rockwool insulation.

The group velocity, ν_g, of an electromagnetic wave in a medium is related to the material properties by

$$\nu_g = \frac{1}{\sqrt{\epsilon_0 \epsilon_r \mu_0 \mu_r}} = \frac{c}{\sqrt{\epsilon_r \mu_r}}. \tag{5.2}$$

The arrival time of the signal with no insulation in the waveguide indicates that the velocity of propagation is $\nu_g = 2.964 \times 10^8\,\mathrm{m\,s^{-1}}$, whilst the velocity of propagation with the rockwool within the waveguide is $\nu_g = 2.863 \times 10^8\,\mathrm{m\,s^{-1}}$. This corresponds to a 3.4 % reduction in velocity due to the rockwool. As dielectric materials usually do not exhibit a magnetic response, it is a safe assumption to let $\mu_r = 1$, therefore, the velocity of propagation in rockwool can be used to obtain an approximate value for the real part of the relative permittivity of rockwool, using Equation (5.2). This gives a value of $\epsilon_r = 1.097$ for rockwool.

5.4.2 Polyurethane Foam Insulation

Polyurethane foam (PUF) insulation is a polymer formed from the combination of two monomers: one containing isocyanate functional groups, the other containing hydroxyl functional groups. The two monomers are combined by mechanical mixing, which creates nucleation sites for the formation of bubbles, causing the mixture to foam. The foam mixture expands as the reaction proceeds, and finally sets rigidly. PUF insulation, like rockwool, is used for high temperature service, but its main geographical regions of employment are in locations such as Alaska. Due to the closed-cell structure of the insulation, it does not easily absorb water, absorbing less than 1.4 % of its weight in water after 96 hours of immersion, though over the course of years industrial observations have shown that it does become saturated. The density of PUF is controlled during manufacture, but the grade typically used industrially has a density of $48\,\mathrm{kg\,m^{-3}}$. The thermal conductivity is approximately $\kappa = 0.026\,\mathrm{W\,m^{-1}\,K^{-1}}$ [75].

The experiment to measure the attenuation of PUF insulation employed a 3 m length of waveguide. Three 400 mm long sections of PUF insulation, in the form of half-shells with an inside diameter of 164 mm and an outside diameter of 276 mm, were

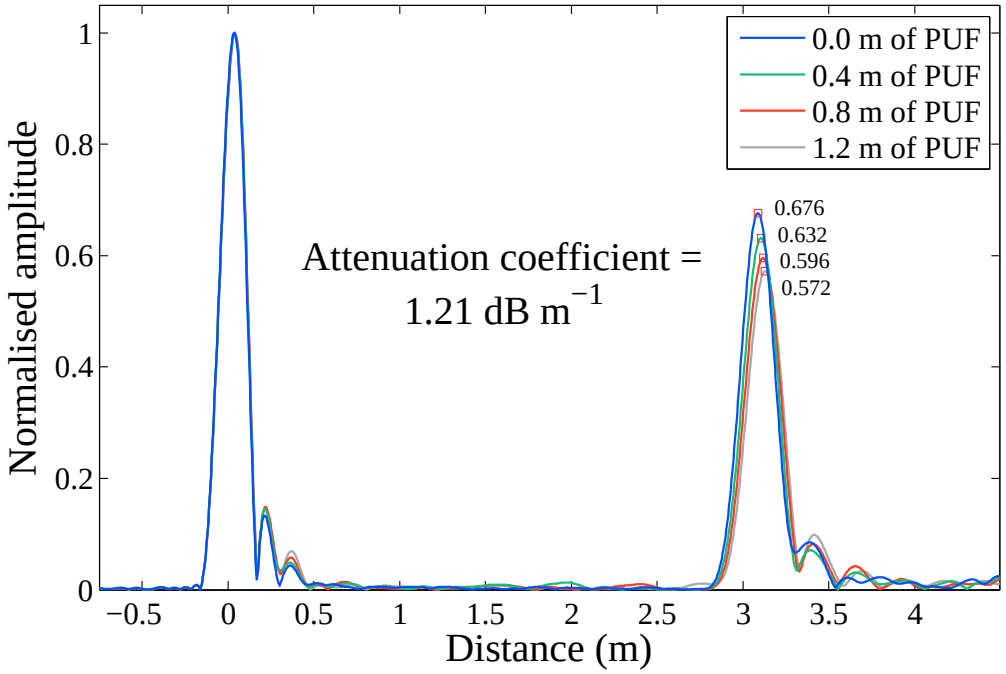

Figure 5.9: Signals measuring the attenuation of polyurethane foam insulation.

obtained from Trident Foams [76]. These were introduced into the waveguide one at a time, from the end distal to the antenna array, with the start of the PUF positioned at the 1.3 m point. Figure 5.9 displays the signal from the empty waveguide, alongside the signals from 0.4, 0.8, and 1.2 m of insulation. It can be seen that as additional lengths of PUF insulation are introduced, the amplitude of the end reflection is reduced, due to the attenuation caused by the PUF insulation. By comparison of the 1.2 m PUF signal with the empty waveguide signal, and using Equation (5.1), the pulse-echo attenuation coefficient is calculated to be $\alpha = 1.2\,\mathrm{dB\,m^{-1}}$. This is an attenuation coefficient which is six times greater than that of rockwool. The presence of increasing lengths of PUF in the waveguide also causes increasing delays in the arrival of the end reflection, however, since the waveguide is not completely filled with the material, measurement of the relative permittivity through the reduction in the velocity of propagation would be inaccurate.

5.4.3 Glass Foam Insulation

The third type of insulation is known as glass foam insulation. This is formed from melting down recycled glass; the addition of carbon results in the production of carbon dioxide which causes foaming to occur. This type of insulation is primarily used for cold-service pipes, where the pipes are carrying liquids at a lower than ambient temperature. This type of pipeline is at risk of water vapour condensing on its cold surface, therefore the glass foam insulation is covered by a vapour-proof barrier, in the form of a butyl wrap backed with foil. The density of glass foam insulation is similar to rockwool, approximately $120\,\mathrm{kg\,m^{-3}}$, and it has a thermal conductivity of approximately $\kappa = 0.042\,\mathrm{W\,m^{-1}\,K^{-1}}$ [77]. A low water absorbance of 0.2 % is recorded for glass foam insulation, which is due to water adhering to the surface cells of the foam [77].

Once again, this experiment involved a 3 m length of waveguide. The glass foam insulation was obtained as a sample from BP's Wytch Farm industrial site. It took the form of a half-shell with an inside diameter of 175 mm and an outside diameter of 270 mm. Three sections were cut from this sample, with lengths of 50,

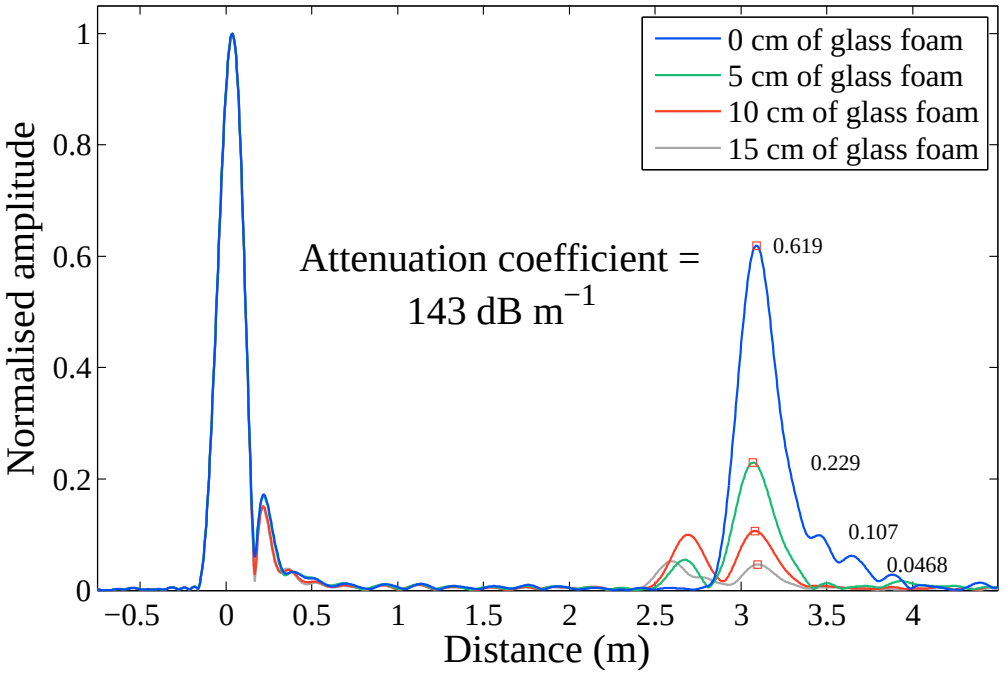

Figure 5.10: Signals measuring the attenuation of glass foam insulation.

100, and 150 mm, which were introduced from the distal end of the waveguide and positioned with a separation of 250 mm from the end-cap. The resultant four signals are displayed in Figure 5.10, from which it can be seen that even short lengths of glass foam insulation cause massive attenuation of the signal. Using the 150 mm glass foam signal, and the empty waveguide signal, the pulse-echo attenuation coefficient is calculated to be $\alpha = 143\,\mathrm{dB\,m^{-1}}$, which is extremely attenuative. This type of insulation could not be inspected with this guided microwave technique.

The use of this guided microwave technique with glass foam insulation would have been more problematic than with the other two types of insulation, regardless of the massive attenuation. The necessity to maintain the integrity of the vapour-proof barrier on the outside surface of the glass foam insulation would have rendered the installation of the antennas almost impossible. In addition, the value of deploying this guided microwave technique on this type of insulation would be minimal, as this type of insulation demonstrates very low water absorbance.

5.5 Field Test to Validate Laboratory Setup

The experiments performed thus far in this chapter were carried out using a model experimental setup, which employed ventilation ducting to simulate a clad and insulated pipeline. From an electromagnetic point of view, a coaxial waveguide formed from ducting should be almost identical to that formed by a real pipeline, however, there are some properties of a real pipeline which are not taken into account by the laboratory setup, such as the conductivity of the actual pipeline materials used, potential corrugations or gaps in the cladding, additional fixings or sealants which may be used during assembly, surface roughness, and any other unforseen complications. Therefore, this section aims to confirm that the guided microwave technique maintains its performance when deployed on a real pipeline in the field, and to validate the model laboratory experimental setup, by comparing experimental results obtained in the laboratory to results obtained in the field.

5.5.1 Experimental Setup

The field test was conducted at BP's Wytch Farm facility in Dorset, UK in November 2011. The section of piping used for the field test was an uncoated 6 m length of carbon steel pipe with a diameter of 6" (NPS6 Sch40). The pipe was elevated off the ground by a truss support at each end. The thermal insulation fitted to the pipe was rockwool, which is the type of insulation predominantly used at Wytch Farm. The pipe was insulated by the facility's insulation contractor in accordance with the facility standard. This involved fitting pre-formed rockwool half-shells around the pipe, each with a length of 1 m. The thickness of the rockwool insulation was 2", which is the standard thickness for the facility. To protect the insulation, cladding was fitted, in the form of galvanised steel sheet, sections of which were placed onto the insulation and secured in place with metallic bands. To facilitate supporting the pipes and to enable transportation, a 0.5 m section of pipe was left exposed at each end of the pipe, therefore only 5 m of pipe was insulated. The exposed ends of the insulation were fitted with metallic capping plates, and sealed to prevent water ingress. Section 6.4 will present results from an experiment in which sections of wet insulation were introduced into the waveguide. To provide access for this experiment, an access window was fitted in the centre of the pipe, consisting of a galvanised steel sheet with clips to allow it to be removed and replaced easily. This section of piping, with the removable cladding section, is shown in Figure 5.11(a).

As this section of piping is a 6" pipe with 2" insulation, the antenna array from the equivalent model experiment was used. The same experimental setup was used as in the laboratory, with the same VNA, splitter, and SMA cables, arranged as shown in the photograph in Figure 5.11(b). The frequency range was also the same as in previous laboratory experiments: 10 MHz to 1.9 GHz.

5.5.2 Validation of Laboratory Results

In order to determine the extent to which the model laboratory experimental setup accurately represents an industrial clad and insulated pipeline, a direct comparison

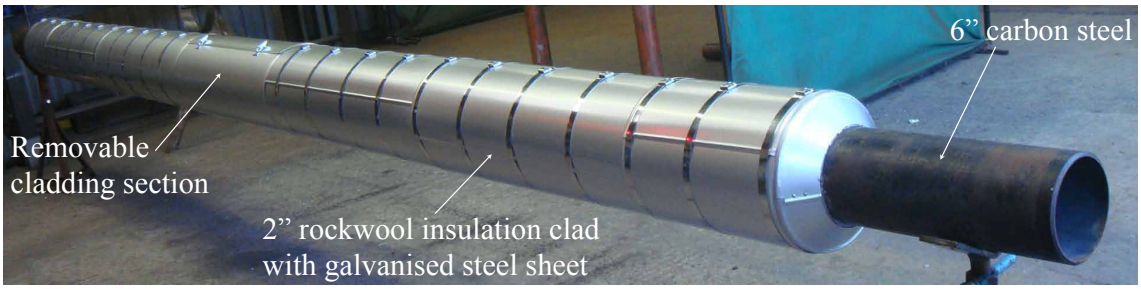

(a) Section of piping used for field test

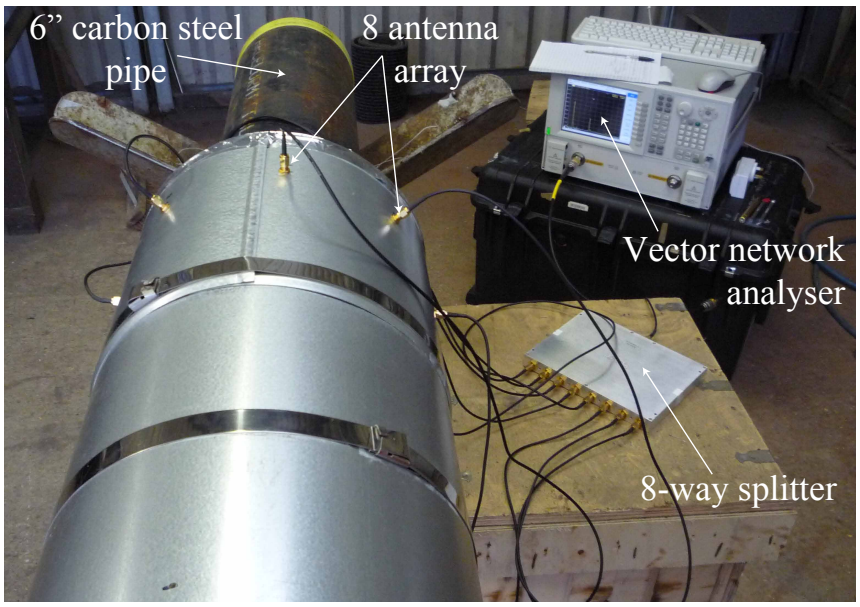

(b) Experimental setup for field test

Figure 5.11: Photos from the field tests: (a) the section of real industrial pipeline, with removable cladding cover to provide access to the insulation; and (b) the equipment used to take the readings.

of two analogous signals was performed. The first signal was obtained from the model ducting experiment in the laboratory with a coaxial waveguide with $a = 140\,\text{mm}$ and $b = 80\,\text{mm}$; the second signal was obtained from this section of real piping. The laboratory ducting waveguide had a length of 6 m, and was completely filled with the same rockwool insulation as was used in Section 5.4.1. The two signals, normalised to their antenna reflections, are plotted in Figure 5.12.

Both of the signals are normalised to the amplitude of the reflection from the antenna at 0 m. The length of the waveguide for the field test was 5 m, but the end reflection appears at 5.39 m. Once again, this is due to the reduction in the velocity

of propagation due to the material properties of the rockwool insulation filling the waveguide. The permittivity of the rockwool inside the field test waveguide caused a 7.2 % reduction in the velocity of the microwave signal relative to its velocity in air. The laboratory waveguide had a length of 6 m, but the end reflection appears at 6.28 m, a 4.5 % reduction in velocity, due to the same effect. The fact that the field test signal shows a greater reduction in the velocity of propagation suggests that the field test rockwool may have a higher relative permittivity than the laboratory rockwool, with values of 1.16 and 1.097, respectively. However, this is not the case; it is merely that the rockwool used at the field test facility is of a higher mass density than the rockwool purchased for the laboratory experiment, with density values of 96.4 $\mathrm{kg\,m^{-3}}$ and 80.7 $\mathrm{kg\,m^{-3}}$, respectively. The permittivity of a dielectric material will increase as the mass density increases, this is caused by the dielectric material

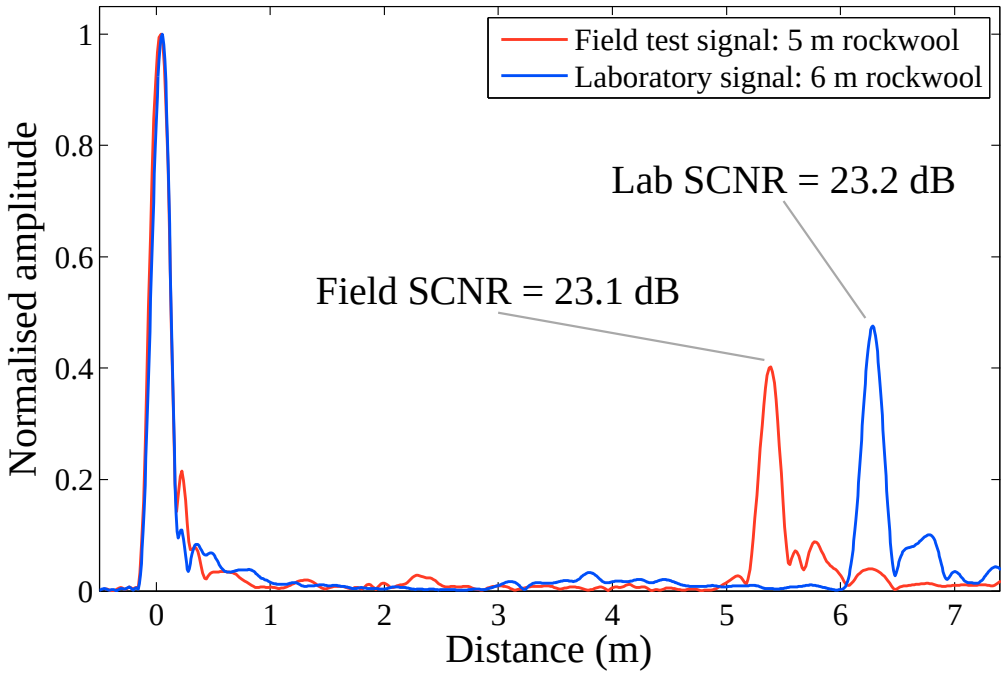

Figure 5.12: Comparison of a signal recorded during the field test on a 5 m length waveguide with a signal recorded using the model laboratory setup of a 6 m length waveguide. The difference in the lengths of the waveguides tested gives rise to the difference in the arrival times of the end reflections. Excellent agreement is demonstrated between the two, providing validation for the accuracy of the laboratory setup in representing the conditions which exist on a real insulated pipeline.

replacing the low permittivity air within the structure of the material. This difference in density also explains why the amplitude of the reflection from the end of the waveguide is lower for the field test result than for the laboratory result; the slight attenuation due to the rockwool, quantified as $\alpha = 0.2\,\mathrm{dB\,m^{-1}}$ for the laboratory density rockwool, is magnified by the higher density of the rockwool used at the facility.

One of the unforeseen complications of using this technique on a real section of pipeline was the discovery that, prior to fitting the cladding, the rockwool insulation shells are fastened to the pipe by lengths of steel wire which are wrapped around the pipe at 300 mm intervals along its length. It might be expected that such metallic reflectors within the waveguide would contribute to the noise level in the signal by giving rise to low amplitude reflections, due to the wire creating an axisymmetric reduction in the radius of the outer conductor and consequently affecting the impedance of the waveguide at that location. However, the SCNR levels for the field test signal and the laboratory signal are given as 23.1 dB and 23.2 dB, respectively, in Figure 5.12. The similarity of the field test SCNR to that obtained in the lab on a waveguide of equivalent dimensions demonstrates the robustness of the technique in the presence of such anomalies, which are inevitable in the industrial environment.

Aside from the differences in velocity of propagation and attenuation due to the variation in the density of the rockwool the signals are very similar, with SCNR values that are in good agreement. This supports the accuracy of the model laboratory experiments in representing the conditions which exist on real industrial insulated pipelines. This result, therefore, validates the use of the model experimental setup, enabling its continued use to investigate other features of industrial pipelines that could affect the guided microwave technique, but would be impossible to investigate in the field; features such as bends and pipe supports. The investigation of bends and pipe supports will be discussed in Chapters 7 and 8, respectively.

5.6 Summary

The previous chapter described the use of simulation software to obtain the optimum design for the antennas in an array. This chapter presents experimental results obtained from two coaxial waveguides and their optimum antenna arrays. The experimental setup is described in detail, including the hardware used to generate the microwave frequency signals, the splitter to obtain the necessary number of channels, and the method of fabricating the antennas. Ventilation ducting was used to represent an insulated pipeline, with the inner duct representative of a 6" pipe. Two different sizes of outer duct were employed: the first with dimensions to represent 3" of insulation, and the second to give an annular distance equivalent to 2" of insulation. The signals obtained from both of these waveguides demonstrated the effectiveness of the simulated optimum antenna designs, obtaining values for the SCNR of 40 dB and 42 dB for the 3" and 2" insulation thicknesses, respectively.

The use of an array approach for the excitation system was validated by comparing the signal obtained from using a single antenna for excitation, to the signal obtained using the full array. The SCNR takes a very low value of 5 dB with a single antenna, and improves by a factor of 52 to 40 dB when the full array is used.

As the insulation material is likely to be the main source of attenuation for this guided microwave technique, experiments were performed to measure the attenuation of three of the most commonly used insulation materials: rockwool, polyurethane foam, and glass foam. The values for the attenuation coefficients for these three insulation materials were measured to be $0.2\,\mathrm{dB\,m^{-1}}$, $1.2\,\mathrm{dB\,m^{-1}}$, and $143\,\mathrm{dB\,m^{-1}}$, respectively. The high attenuation of glass foam renders it impossible to inspect with this inspection technique.

In order to validate the model laboratory experiments using ventilation ducting, a field test was performed on a section of real industrial piping. The validation compared the signal from a 5 m length of 6" diameter industrial piping insulated with 2" of rockwool and clad in galvanised steel, with the signal from a 6 m length of coaxial ventilation ducting with $a = 140\,\mathrm{mm}$ and $b = 80\,\mathrm{mm}$, again insulated with

2" of rockwool. The signals obtained were very similar, with values for the SCNR of 23 dB obtained from both waveguides. There were differences in the extent of the reduction of the velocity of propagation, but it was discovered that this was due to the rockwool being of different densities. The similarity of the signals provided validation for the use of the model laboratory experimental setup, and demonstrated the robustness of the guided microwave technique to operating in the conditions that exist on real industrial pipelines.

Chapter 6

Sensitivity to Water

Chapter 4 described the optimisation of the design of the antenna array to achieve pure-mode excitation of the TEM mode in large coaxial waveguides. Chapter 5 presented experimental results, which demonstrated a SCNR of 40 dB was achievable in coaxial waveguides formed from ventilation ducting with dimensions representative of typical pipeline specifications. This is a promising result as a high SCNR leads to an inspection technique which is very sensitive to the presence of reflecting features in the waveguide. The purpose of this chapter is to investigate the sensitivity of this guided microwave technique to the presence of water, and to determine the minimum cross-sectional extent of water that is detectable. Initially, this will be done with simulations performed in Microwave Studio. Subsequently, experiments will be performed using the model laboratory experimental setup, by gradually introducing water into a tank positioned inside the waveguide. Finally, results will be presented from a field test conducted on a real industrial section of pipeline, to determine if the technique is capable of detecting sections of wet insulation when deployed in the more variable conditions which exist in the field. The laboratory experiments to determine the sensitivity to water were published in a paper in the *Journal of Nondestructive Evaluation* [P4], and in the QNDE 2010 conference proceedings [P2]. The results of the field test investigating the sensitivity of the technique to sections of wet insulation on a real industrial section of piping will be presented in a paper submitted to the journal *Insight* [P6].

6.1 Electromagnetic Wave Interaction with Water

In Equation (3.1) the relative permittivity of a material is described as being complex and frequency dependent. As previously mentioned in Section 3.1.1, the imaginary part of the permittivity, ϵ_r'', controls the dissipation of energy within the material. The absorption coefficient of liquid water as a function of frequency is shown in Figure 6.1, in addition to the index of refraction as a function of frequency. From this figure it can be seen that the interaction of electromagnetic waves with water demonstrates rather complex behaviour; this is the subject of this section.

Water molecules are comprised of two hydrogen atoms and one of oxygen. These three atoms adopt a triangular arrangement with the two hydrogen atoms located at two of the vertices connected to the oxygen atom positioned at the third vertex.

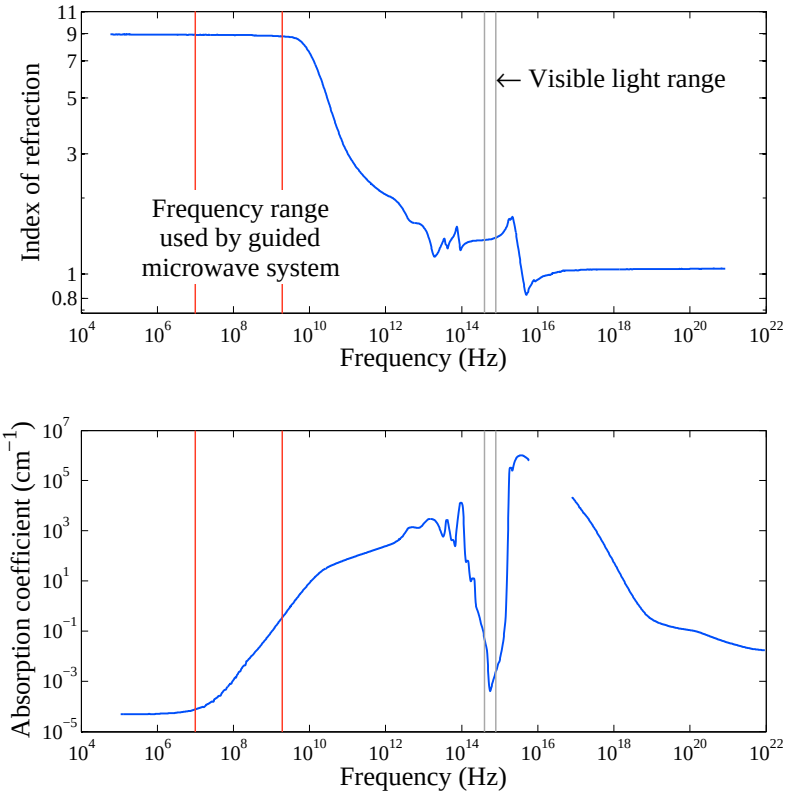

Figure 6.1: Reproduced from Figure 7.9 in Jackson [32, p.315]. Index of refraction (top) and absorption coefficient (bottom) for liquid water as a function of frequency.

This molecular arrangement leads to a partial negative charge on the oxygen side of the molecule, with a partial positive charge at the end of the molecule with the two hydrogen atoms. Such polar molecules are referred to as molecular dipoles. Under the influence of an external electric field, the molecular dipoles will align with the field. If the external electric field is oscillatory in nature then the molecular dipole will undergo regular rotations to maintain alignment with the electric field, giving rise to the high value of the real part of the relative permittivity of water ($n = 9$, therefore, $\epsilon'_r = 81$) at frequencies up to 1×10^{10} Hz, as can be seen in Figure 6.1. At low frequencies, these molecular rotations occur with a speed and infrequency that does not effect the temperature of the water. As such, the absorption coefficient of water takes a very low value for frequencies up to 1×10^{8} Hz. As the frequency increases above this point, the absorption coefficient begins to increase in value. This is because the frequency of the oscillation of the field has reached the point where the molecular dipoles can no longer maintain their alignment to the field without experiencing a resistance to their motion that is analogous to viscosity in fluids. This viscous resistance is due to attractions and interactions between the water molecules, and also due to thermal molecular vibration [78]. This resistance gives rise to a delay in the time taken between the field alignment switching and the molecular dipole matching this new alignment. Debye developed a relaxation model describing this behaviour [79], and he termed the delay in the molecular alignment the relaxation time, τ, which takes a value of $\tau = 2.5 \times 10^{-11}$ s for liquid water [79, p.85]. The resistance experienced by the molecules while they align with the external field is the source of the heating, which enables microwave heating of food (industrial and domestic microwave ovens operate at 915 MHz and 2.45 GHz, respectively), and which also explains the positive gradient of the absorption coefficient of water from 1×10^{8} Hz to 1×10^{13} Hz. At frequencies above 1×10^{10} Hz, the relaxation of the molecular dipoles causes the index of refraction to decrease in value, until $n = 1.34$ in the visible light region. From Figure 6.1, it can be seen that there is a very distinct window in the absorption coefficient between 4×10^{14} Hz and 8×10^{14} Hz, corresponding to the visible light region of the electromagnetic spectrum. This absorption window is due to the energy level structures of the atoms

in water [32, p.314]. As the frequency increases further still, the molecular dipoles can no longer react sufficiently quickly to align with the oscillating field, and are therefore unaffected by it, which explains why the absorption coefficient is low at high frequencies and why the relative permittivity becomes equal to one.

The Debye relaxation model [79], mentioned above, reveals that the behaviour of the permittivity of a material in the intermediate frequency range between the low and high frequency cases can be described by the equation

$$\epsilon(\omega) = \epsilon_\infty + \frac{\epsilon_s - \epsilon_\infty}{1 + j\omega\tau}, \tag{6.1}$$

where ϵ_∞ is the infinite frequency relative permittivity, and ϵ_s is the static relative permittivity. This equation is used to describe the permittivity of water as a function of frequency during numerical simulations with MWS. The index of refraction and the relaxation time of water can be used to calculate the attenuation coefficient for a particular frequency, using the relationship

$$\alpha = -k_i \approx \frac{\omega^2 n\tau}{2c_0}, \tag{6.2}$$

which gives α =117 dB m^{-1} as the one-way attenuation coefficient at the centre frequency of 955 MHz. With such a high attenuation, the amplitude of the reflection from the back of a water volume will be negligible compared to the amplitude of the reflection from the front, therefore only the front reflection is considered in the experiments and simulations performed in this work.

6.2 Simulations of Scattering from Water Volumes

The initial approach to investigating the scattering from water volumes was to perform simulations of water volumes inside a large coaxial waveguide using the Microwave Studio software. A model representing a 6" pipe with 3" insulation was created. The dimensions of the waveguide used were: length of waveguide, $l = 3$ m, radius of outer conductor, $a = 157.5$ mm, radius of inner conductor, $b = 80$ mm, with

vacuum for the annular volume of the coaxial waveguide, and the background material (effectively defining the pipe and cladding) set to PEC. The model was created with 8 antennas at 45° intervals around the circumference, which is the minimum number of antennas required to obtain pure TEM mode excitation according to Table 4.1. The antennas were created such that each had a radius, $r = 5.57\,\text{mm}$, and length $s = 63.8\,\text{mm}$, to match the optimum design obtained in Section 4.4.2. A 100 mm length of coaxial waveguide was placed between the excitation ports of the model and the antennas, in addition to the bends required to align the port with the mesh as described in Section 4.4.1, in order to introduce a slight delay so as to be able to clearly resolve the reflection from the antennas. A mesh discretisation of 10 elements per wavelength was used throughout the majority of the model; however, a conforming mesh was used to model the field in the vicinity of the small antennas; the total number of elements used in the model was 3.9×10^6. The frequency range for the simulation was defined to be from 0 to 1.9 GHz. The time-domain solver

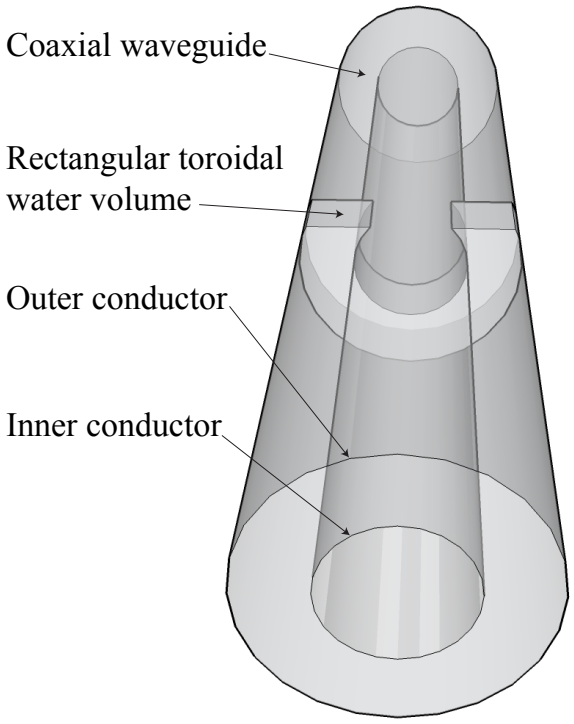

Figure 6.2: Diagram of the rectangular toroidal tank, positioned within the coaxial waveguide, which was used in simulations to assess the strength of reflection from increasing volumes of water.

employed to perform the simulation used a time-step of 4.8×10^{-12} s. The results from the simulation are output in the form of scattering parameters (reflection and transmission coefficients in the frequency-domain); these are then analysed using TDR, to obtain a signal in the time-domain. The water volume was modelled by creating a component with material parameters set to water, described by the Debye model, with a shape equivalent to rotating a rectangle about the waveguide axis, forming a rectangular toroidal tank with the same cross-section as the annulus of the waveguide. The axial extent of the torus was 50 mm (for reference the centre wavelength in air and in water are 315 mm and 35 mm, respectively) and it was positioned in the centre of the length of the waveguide. The height of the water component was parameterised, so that the cross-sectional extent of water could be varied in a parameter sweep, creating the effect of gradually filling the tank with water. A representation of this rectangular toroidal tank, partially filled with water, is displayed in Figure 6.2.

For each volume of water, the reflection coefficient was obtained by normalising the amplitude of the reflection from the water volume with the reflection from the

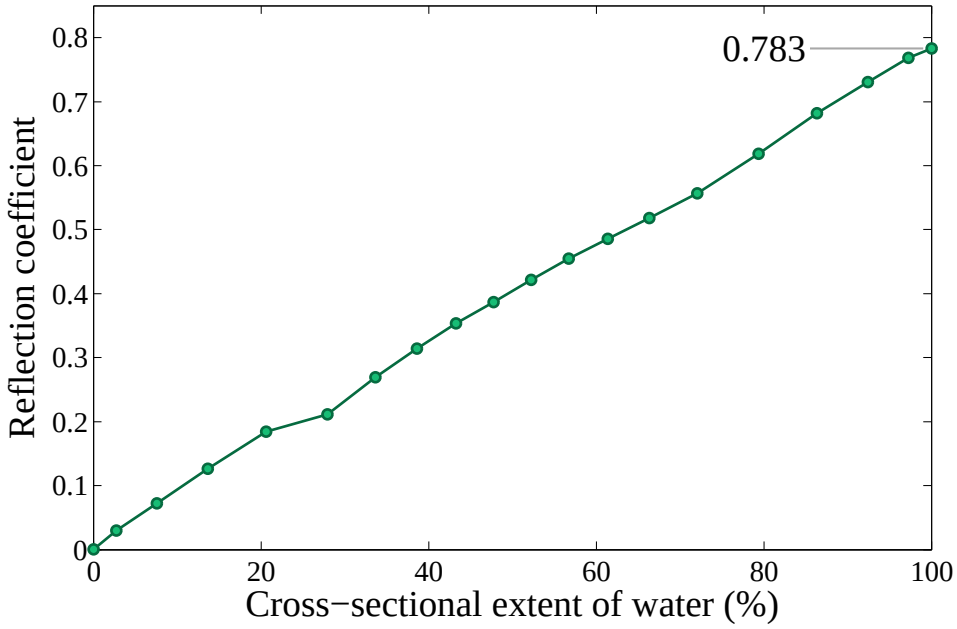

Figure 6.3: Simulated reflection coefficient of the TEM mode, propagating in a coaxial waveguide with $a = 157.5$ mm and $b = 80$ mm, as a function of the cross-sectional area of the waveguide occupied by water. The axial extent of the water volume is 50 mm.

end of the empty waveguide. Figure 6.3 plots the reflection coefficient against the percentage of the cross-sectional area of the waveguide occupied by the water volume. From Figure 6.3, it can be seen that the relationship between the reflection coefficient and the cross-sectional extent of the area of the water volume is approximately linear, with increasing amplitudes of reflection from increasing cross-sectional areas. Also of note, is the fact that the strength of the reflection from the water volume is high, with a fully cross-sectional water volume producing a reflection coefficient of 78.3 %. The theoretical value for this reflection coefficient (see Equation 1.2 and discussion in Section 1.3) is 79.7 %, which is in excellent agreement with the value obtained from these numerical simulations.

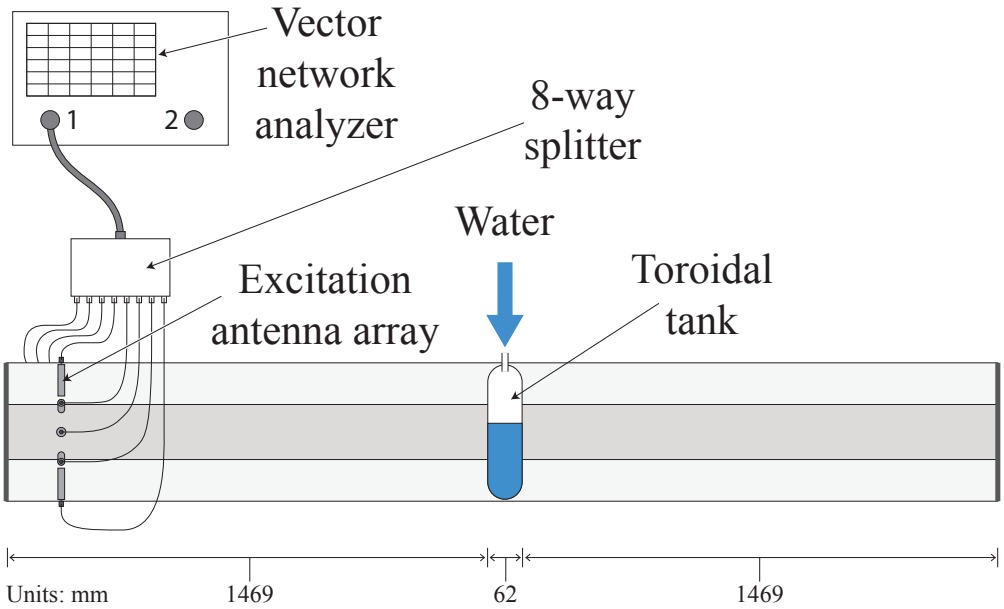

Figure 6.4: Experimental setup. The VNA generates the microwave signal, which is split into eight channels by the splitter to feed the array. The ducting is short-circuited at both ends. The toroidal tank is placed in the centre of the waveguide, with a hose running through a hole in the ducting to introduce discrete volumes of water into the tank.

6.3 Experimental Investigation of Scattering from Water Volumes

An experiment was performed to validate these simulated results by assessing the strength of the reflection from water within the waveguide. The experiment sought to quantify the sensitivity of the guided microwave technique to the presence of water, by determining the minimum cross-sectional extent of water which was detectable. The experimental setup, which is shown in Figure 6.4, was largely the same as described in Section 4.3, with the waveguide formed from ventilation ducting with $a = 157.5\,\text{mm}$ and $b = 80\,\text{mm}$ and a length of 3 m. A frequency range of 10 MHz to 1.9 GHz was used, with the optimised eight antenna array used for excitation. Water was introduced into the waveguide via a hose running through a hole drilled in the outer cladding. A tank was positioned within the waveguide to contain the water. The tank was formed from flexible plastic tubing, as shown in Figure 6.5(a), with an inner diameter of 62 mm. This tubing was bent around the inner conductor, effectively creating a ring torus shape, as shown in Figure 6.5(b), with an inner diameter of 168 mm, and an outer diameter of 294 mm.

Figure 6.6 shows four examples of signals obtained during this experiment. The signals were normalised to the amplitude of the reflection from the end of the empty waveguide. Each of the signals displays a peak at 0 m and another peak at 3 m; these are due to the reflections from the start and end of the 3 m waveguide, respectively. Figure 6.6(a) was recorded with only the empty plastic toroidal tank inside the waveguide; a small reflection from this plastic tank can be seen at 1.5 m. Figure 6.6(b) was recorded with only 200 ml of water inside the toroidal tank (which is equivalent to a cross-sectional extent of 5 % of the waveguide), and the reflection from this amount of water is clearly detectable.

The reflection coefficient from the water volume can be plotted against the cross-sectional extent of the water within the waveguide, as shown in Figure 6.7. To remove the effect of the plastic tank, the amplitude of the reflection from the empty tank was subtracted from the amplitude of the reflection measured from different

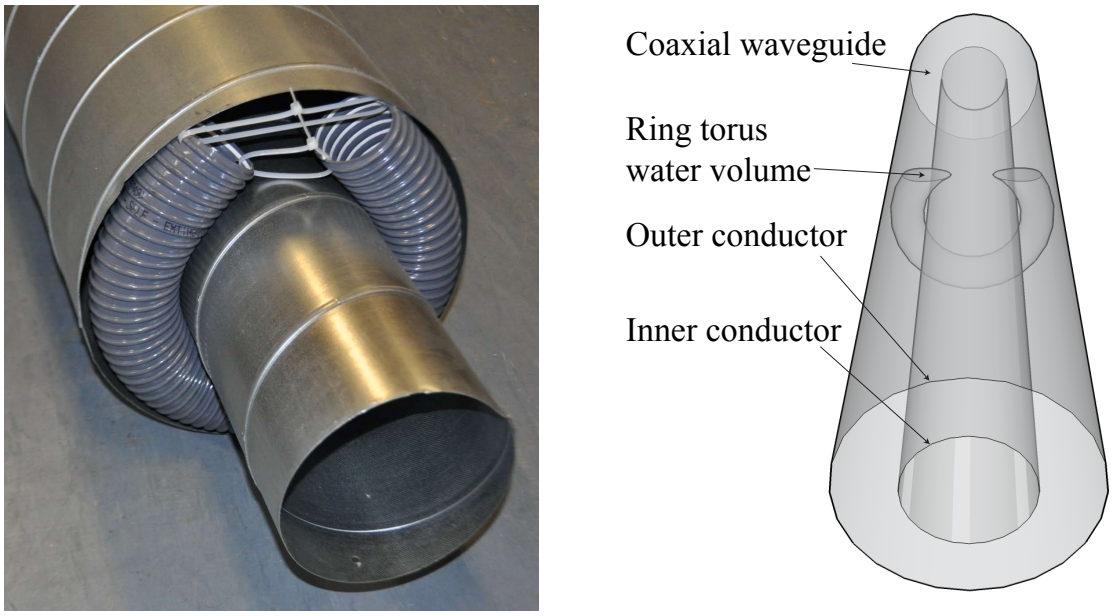

(a) Photograph of toroidal tank

(b) Diagram of toroidal tank inside the waveguide

Figure 6.5: The toroidal tank placed in the centre of the waveguide and gradually filled with discrete volumes of water, in order to determine the sensitivity of the technique to the presence of water within the waveguide.

water volumes. Figure 6.7 also provides a direct comparison with simulated results obtained from a model recreating the ring torus shape of the tank used in this experiment (this is different from the rectangular torus used in Section 6.2). It can be seen from Figure 6.7 that the simulated and experimental results exhibit very good agreement, in the range from 0 % to 60 %. The experimental results were only obtained for cross-sectional extents up to 60 %, as the toroidal tank did not completely fill the cross-section of the waveguide. In order to experimentally investigate the behaviour of a 100 % cross-sectional extent water volume, an experiment was conducted in which the coaxial waveguide was oriented vertically and placed in a large tank. This tank was then gradually filled with water, until the reflection from the water volume was clearly resolved from the reflection from the end of the waveguide. The value of the reflection coefficient from a 100 % cross-sectional water volume recorded by this experiment was 80.9 %, which is in good agreement with

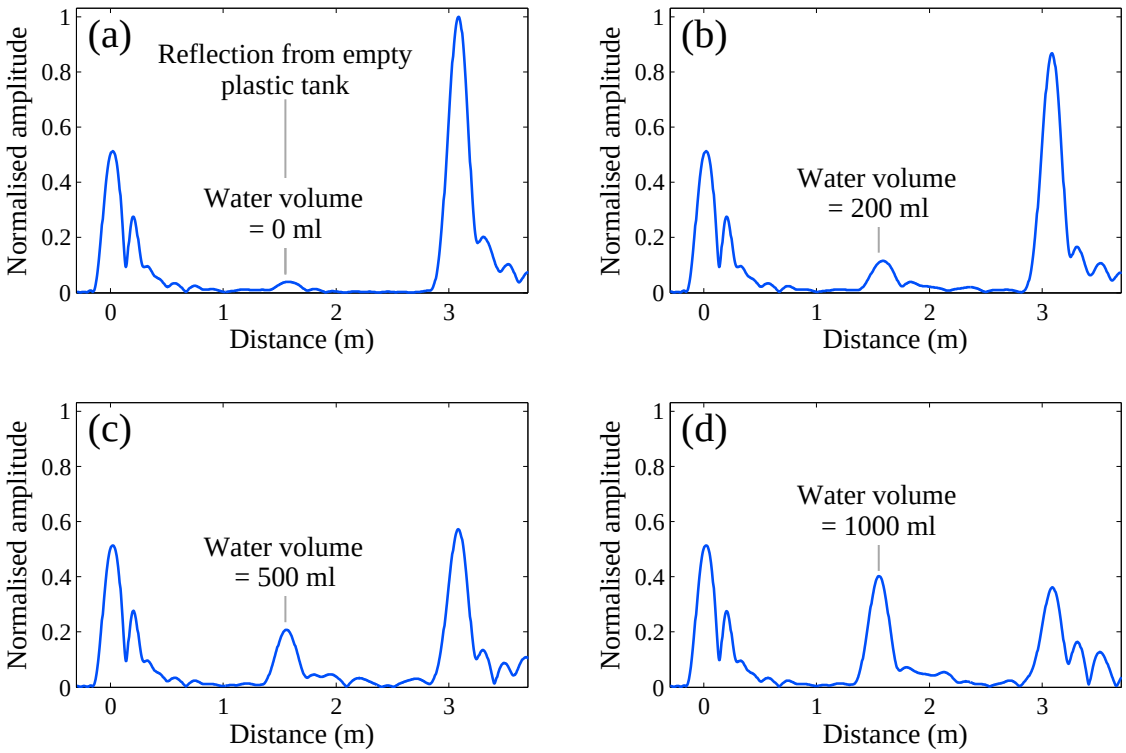

Figure 6.6: Signals measured for four water volumes: (a) 0, (b) 200, (c) 500, and (d) 1000 ml. The water volume is positioned 1.5 m from the array. The signals are normalised to the amplitude of the reflection from the end of the empty waveguide. As the water volume increases, so does the amplitude of the reflection from it, while the reflection from the end of the waveguide decreases by energy conservation and attenuation.

the values obtained from simulation and from the analytical relationship in (1.2), which were 78.3 % and 79.7 %, respectively.

6.4 Field Test Investigation of Scattering from Wet Insulation

The laboratory experiment described in the previous section was designed to detect a volume of water within the waveguide, rather than a section of wet insulation amidst dry insulation, which is the case in reality. In order to investigate the sensitivity of the technique to the discontinuity between wet and dry insulation, an experiment was conducted during the field test, which was described in Section 5.5, involving

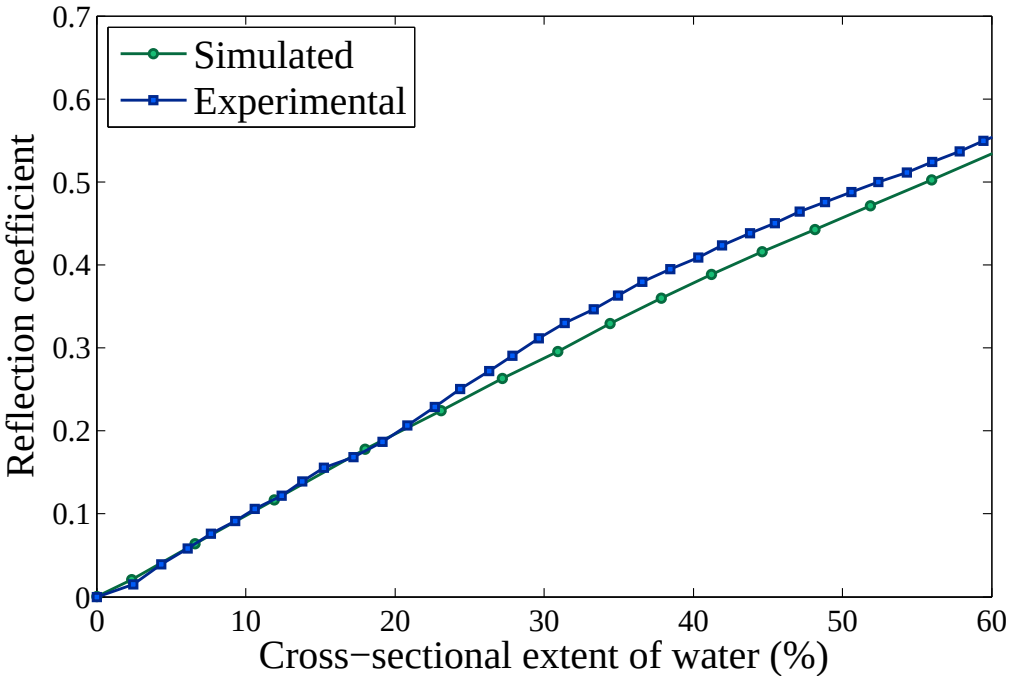

Figure 6.7: Reflection coefficient as a function of cross-sectional extent of the waveguide occupied by water inside a ring torus tank. Experimental results are compared to numerical simulations.

the introduction of sections of wet insulation into the waveguide formed by the section of real pipeline. The field test pipeline section was a 6" pipe fitted with 2" of rockwool insulation.

Over short timescales rockwool is very hydrophobic, with water simply running off its surface. Therefore, in order to recreate the industrial conditions which exist after prolonged periods of exposure to water (field observations have shown that it is not unusual for the insulation cross section to be completely saturated with water) sections of wet insulation were prepared in advance. A sample of rockwool was obtained from the Wytch Farm facility, in order to ensure that the wet and dry rockwool insulation types were identical. From this sample of rockwool, an annular cross-section was cut with a length of 4", and this annulus was then cut into eight equal sections. These sections were then submerged in fresh water for 12 days, by which point they were completely saturated with water, having increased in weight by a factor of ten. These samples were then sealed in plastic film in order to maintain their saturation during transit. After taking readings of the

pipeline with dry insulation, the removable cladding section, which can be seen in Figure 5.11(a), was removed and a section of the dry insulation within was cut out in order to accommodate the wet insulation sample. The cladding section was then replaced and the signal recorded. This was repeated, adding each of the eight wet insulation sections in turn, as shown in Figure 6.8, until the entire cross-section of the waveguide was occupied by wet insulation.

The results from the field test are summarised in Figure 6.9, which shows four examples of the signals recorded during the experiment with the wet insulation sections. Figure 6.9(a) shows the signal from the pipeline with no wet insulation sections, which is the same as the field test signal displayed in Figure 5.12. The peak at 0 m is the reflection from the antennas, and the peak at 5 m is the reflection from the end of the waveguide. Figure 6.9(b) shows the signal recorded with the first wet insulation section placed within the pipeline. The peak at 2.7 m shows that wet insulation occupying only 12.5 % of the cross-section of the waveguide is detectable above the noise floor. Figures 6.9(c) and (d) show the signals for 50 % and 100 % wet insulation and it can be seen that the amplitude of the reflection from the wet insulation increases with cross-sectional extent. In addition, it can be seen that the

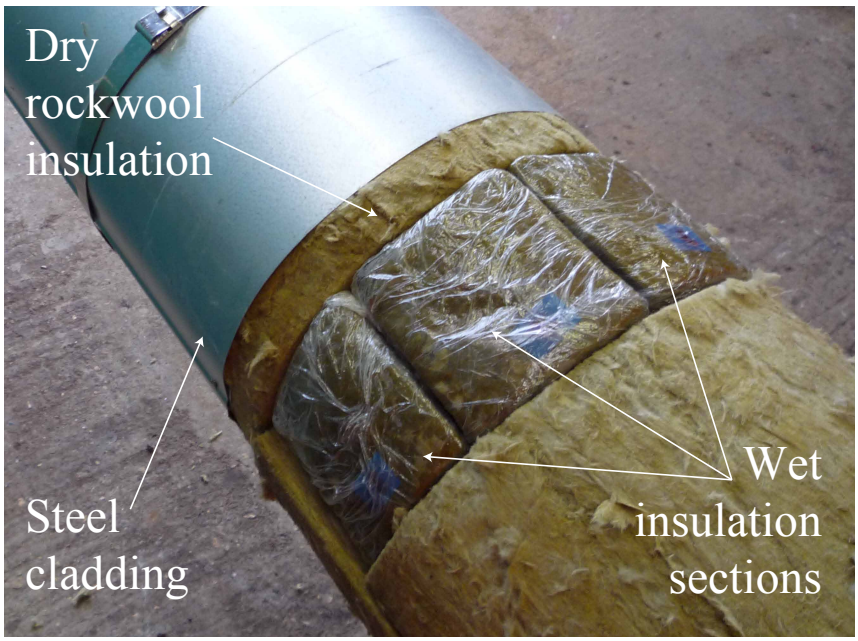

Figure 6.8: Photograph showing three wet insulation sections placed within the waveguide before the removable cover is replaced.

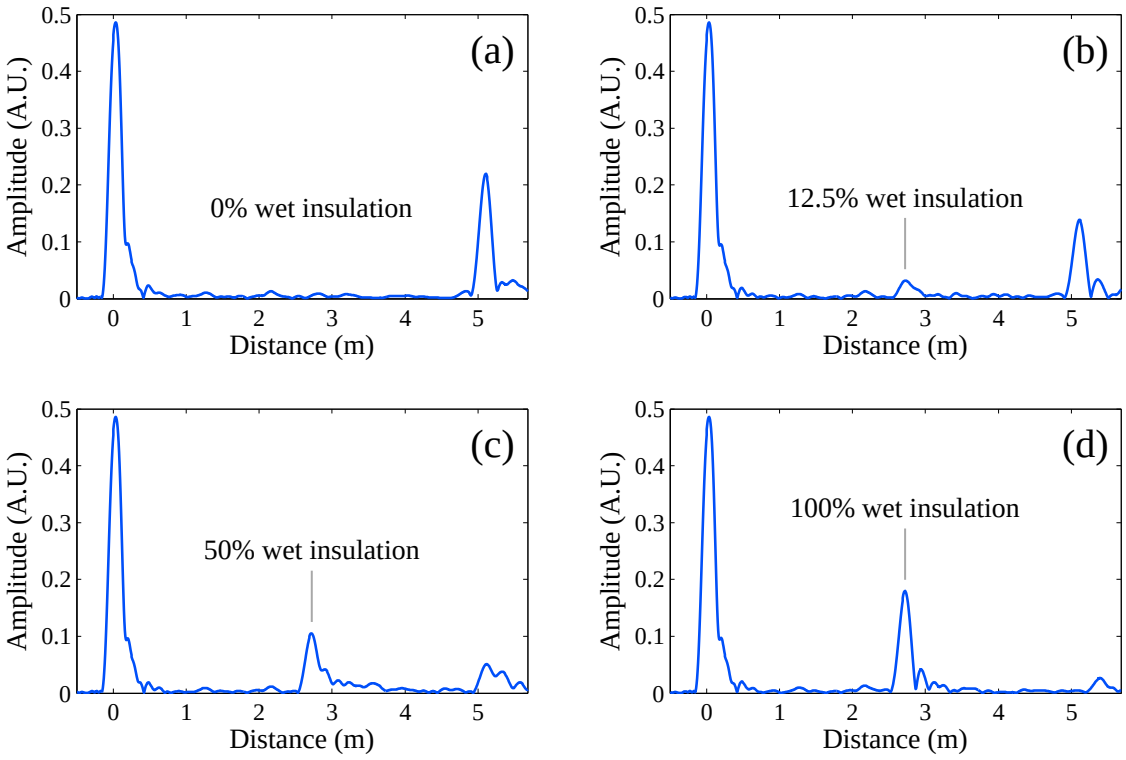

Figure 6.9: Four examples of signals from the field tests: (a) no wet insulation; (b) one section of wet insulation, equivalent to 12.5 % cross-sectional extent; (c) four wet insulation sections, equivalent to 50 % cross-sectional extent; and (d) all eight wet insulation sections, equivalent to 100 % of the cross-section of the waveguide annulus occupied by wet insulation.

amplitude of the reflection from the end of the waveguide is drastically reduced; this is due to attenuation of the microwave signal by the water within the waveguide.

The reflection coefficient of the wet insulation can be plotted as a function of the extent of the cross-section of the pipeline that is occupied by water. This field test data is shown in Figure 6.10 in red, from which it is apparent that the results show a linear relationship between reflection coefficient and cross-sectional extent. A 100 % cross-sectional extent section of wet insulation gives rise to a reflection coefficient of 81.7 %, which is in good agreement with the value of 80.9 % measured in the laboratory. For comparison, simulations were performed in Microwave Studio to reflect the experiment conducted during the field test, and these are plotted on the same figure in green. Also plotted in this figure, in blue, are results obtained from

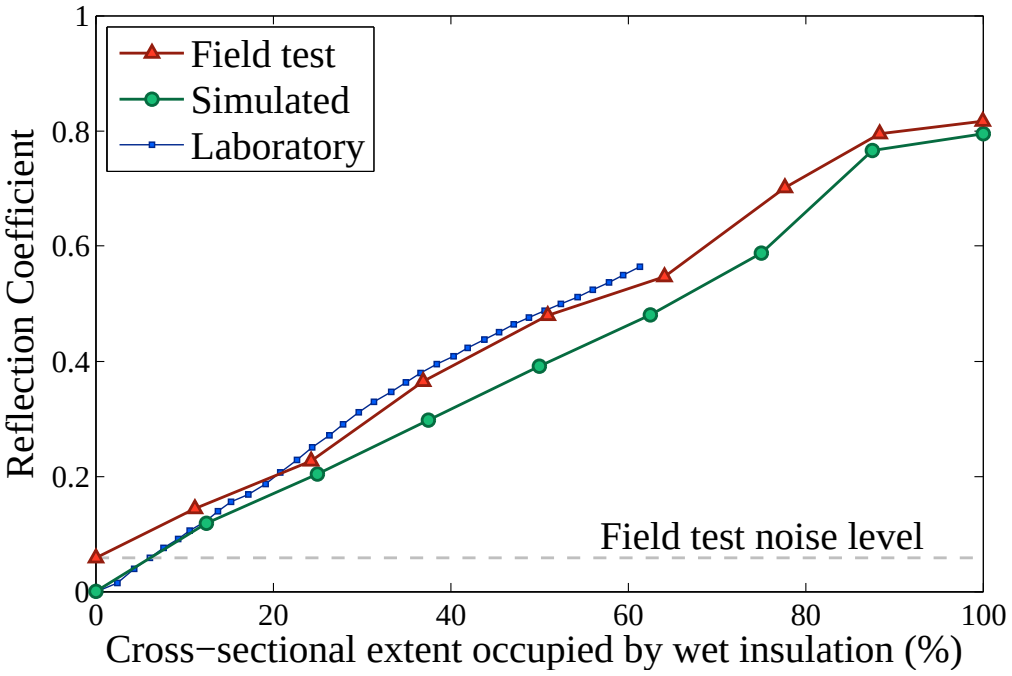

Figure 6.10: The reflection coefficient of the wet insulation as a function of the cross-sectional extent of the insulation annulus that is occupied by wet insulation. Field test data is plotted alongside results obtained from simulations and results from a previous laboratory experiment; the three data sets are in good agreement.

the previous laboratory experiment, described in Section 6.3. It can be seen that there is good agreement between all three sets of data.

6.5 Reflection from Diffuse Water Volumes

The simulated and experimental results presented in the thesis thus far have all considered three-dimensional water volumes that occupy a portion of the insulation annulus, with a sharp transition from dry insulation to wet. The properties of the waveguide change from those of dry insulation to those of wet insulation over a negligibly short distance. No information exists as to the morphology of regions of wet insulation that occur in the field, however, industrial observations record that it is not unusual to find regions of insulation that are saturated with water throughout the cross-section of the waveguide. Other regions of the pipe will have insulation that is completely dry, therefore, there must be a transition from 100 % dry insulation

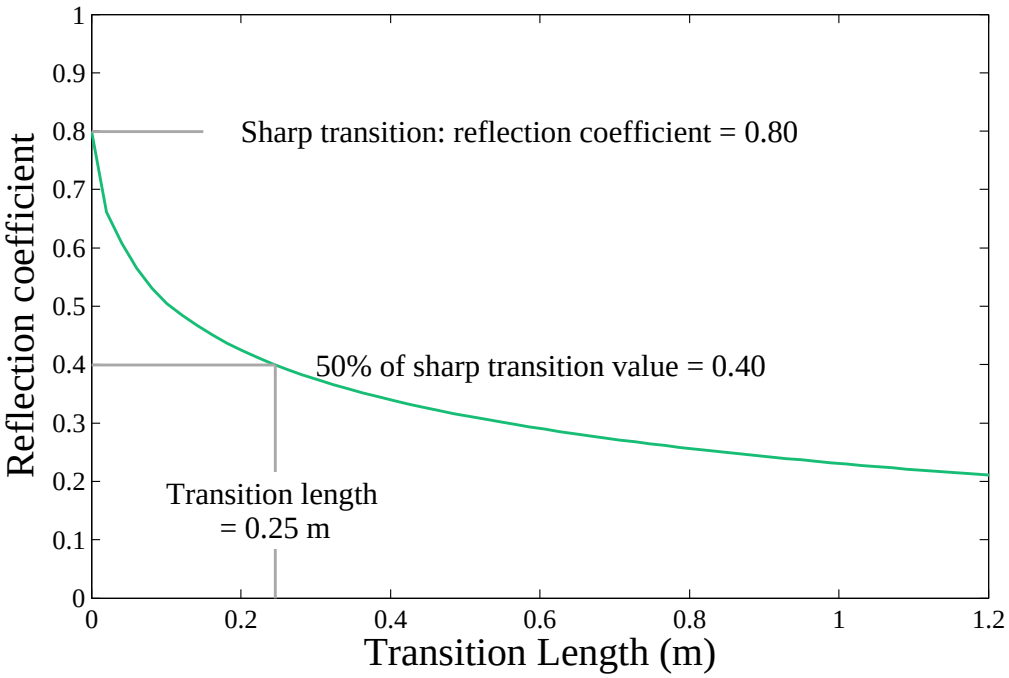

Figure 6.11: The reflection coefficient of the TEM mode from a transition interface between dry and wet insulation, as a function of the length of the transition.

to 100 % wet insulation. The primary factor that will affect the detectability of a region of wet insulation will be the length over which this transition occurs.

To investigate the effect of this morphological parameter of a water volume, we consider an ideal axisymmetric water volume that is tapered over a characteristic transition length such that the properties of the waveguide change linearly from those of dry insulation to insulation that is saturated with water throughout its cross-section [80]. The reflection coefficient from such a tapered water volume will be a function of frequency, with higher frequencies demonstrating lower reflection coefficients. In order to monitor the effect of the transition length, the reflection coefficient at the centre frequency of the operating frequency range of the guided microwave system ($f_m = 955\,\mathrm{MHz}$) is calculated, and plotted as a function of the length of the transition from dry insulation to wet, as shown in Figure 6.11.

The relationship between the reflection coefficient and the transition length demonstrates that a small increase in the length over which the dry-to-wet transition occurs

will result in a significant decrease in the reflection coefficient. This can be quantified by looking at the transition length at which the reflection coefficient decreases to 50 % of its sharp transition value. A sharp transition between dry and wet insulation produces a reflection coefficient of 80 %. A halving of this value of the reflection coefficient to 40 % is caused by a transition length of 0.25 m. This is a result which indicates the difficulty that may arise in using this technique to detect regions of wet insulation in the field, as it is possible that the transition lengths could be significantly longer than 0.25 m under industrial conditions. A long transition from dry insulation to wet corresponds to a smooth variation in the waveguide impedance, and thus, the guided microwaves will experience very little reflection from such a transition.

The transition length is not the only significant parameter; the reflection coefficient will be affected by the shape of the water volume in addition to the water concentration through the affected region of insulation. This is an area that requires further investigation, in particular, additional work is required to understand how water diffuses through the insulation in a real pipeline.

6.6 Summary

This section used the optimised excitation system, developed in the previous section, to investigate the sensitivity of the guided microwave technique to the presence of water within the waveguide. This involved understanding how electromagnetic waves interact with water; the absorption coefficient of water is a complex function of the frequency of the electromagnetic waves, whilst the index of refraction, and hence permittivity, are also frequency dependent. At the frequencies of the microwave regime that this technique is capable of operating in, the permittivity is high, which corresponds to high contrast between wet and dry insulation.

Simulations were performed of the scattering from a water volume of increasing height in a coaxial waveguide. These simulations revealed a linear relationship between reflection coefficient and cross-sectional extent of the waveguide occupied

by water. This was validated by performing an experimental investigation of the scattering from water, which was gradually introduced into a tank within the ducting waveguide. The simulated results were validated as the experimental results were in good agreement with the simulated results. The sensitivity of the guided microwave technique was found to be excellent, with a volume of water presenting only a 5 % cross-sectional extent being readily detectable.

In order to verify that the technique would maintain its sensitivity when deployed in a realistic inspection scenario, of detecting wet insulation amidst dry, a field test was conducted on a section of real industrial pipeline fitted with rockwool insulation. Sections of wet insulation were introduced in turn into this length of pipeline. The technique was capable of detecting the introduction of the first section of wet insulation, which presented a 12.5 % cross-sectional extent patch of wet insulation. This confirmed the sensitivity of the technique during a realistic inspection scenario, and under the variable conditions which exist in the field.

In order to address the issue of the sensitivity of the technique to diffuse water volumes, a model was constructed of a simple, tapered, axisymmetric water volume, and this model was used to investigate the effect on the reflection coefficient of increasing the length of the transition from completely dry insulation to insulation that is fully saturated with water. It was found that the length over which the reflection coefficient drops by a factor of two is 0.25 m. This indicates the difficulties that may arise when implementing this technique in the field if the transition lengths between wet and dry insulation are significantly longer than this.

Chapter 7

The Effect of Bends in Pipelines

In Chapter 4 the development of the excitation system for this guided microwave technique was described, and in Chapter 5, it was demonstrated that a SCNR of 40 dB could be achieved with this excitation system. In Chapter 6, the sensitivity of the guided microwaves to the presence of water within the waveguide was investigated. The results indicated excellent sensitivity, with a water volume presenting only a 5 % cross-sectional extent being detectable with the model setup in the laboratory, whilst a 12.5 % cross-sectional extent section of wet insulation was detected in the field. Experiments conducted during the development of this technique have been confined to straight lengths of waveguide. Bends are a common feature of process pipework, where they are required to achieve directionality; but are also found at expansion loops on transit pipelines, which allow the pipeline to expand and contract with changes in temperature. As the sensitivity of the guided microwave technique to the presence of small water volumes is intrinsically linked to the SCNR of the inspection signal, it is of central importance to determine if the high SCNR of 40 dB can be maintained across the types of bends which are commonly found at industrial facilities.

Work in the early 1950s addressed the problem of bends in circular waveguides, in the context of long-distance communications [81–86]. With reference to the diagram in Figure 7.1(a), it was shown that when the axisymmetric TE_{01} mode (see [39] for

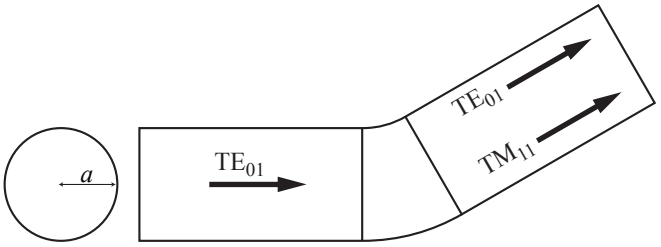

(a) Circular waveguide bend

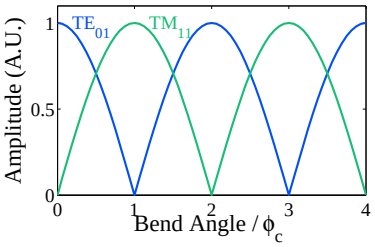

(b) Oscillatory mode conversion

Figure 7.1: (a) Circular waveguide with the low-loss TE_{01} mode in excitation into a bend, which undergoes mode conversion such that a proportion of the energy emerges in the TM_{11} mode. (b) Diagram showing how the extent of the mode conversion in a circular waveguide oscillates sinusoidally as a function of the bend angle, with maximum mode conversion occurring at an angle ϕ_c.

details on the convention of circular waveguide mode nomenclature), which is the preferred mode for transmission due to its very low attenuation, is incident on a bend, the amplitude of the transmitted TE_{01} mode drops and an additional non-axisymmetric TM_{11} mode emerges from the bend. Jouguet [81] recognised that, for shallow bends, complete mode conversion into the non-axisymmetric mode would occur at a bend angle, ϕ_c, given by

$$\phi_c = \frac{\pi\lambda_0}{2.32a} \text{ (radians)}, \tag{7.1}$$

where λ_0 is the wavelength in vacuum, and a is the radius of the circular waveguide. At other angles, the transmitted energy would be divided between the two modes with the amplitude of the transmitted TE_{01} mode varying proportionally to the cosine of the bend angle and that of TM_{11} showing a sinusoidal dependence, so that when the amplitude of TE_{01} is large, that of TM_{11} is small; and vice versa by energy conservation, as shown in Figure 7.1(b). It should be noted that this relationship has no dependence on the bend radius, due to the limitation that it can only be applied to gradual bends.

A similar trend can be expected for the transmission of TEM through a coaxial bend, according to the diagram in Figure 7.2. In particular, it can be observed that the TE_{01} mode of the circular waveguide is analogous to the TEM mode of the

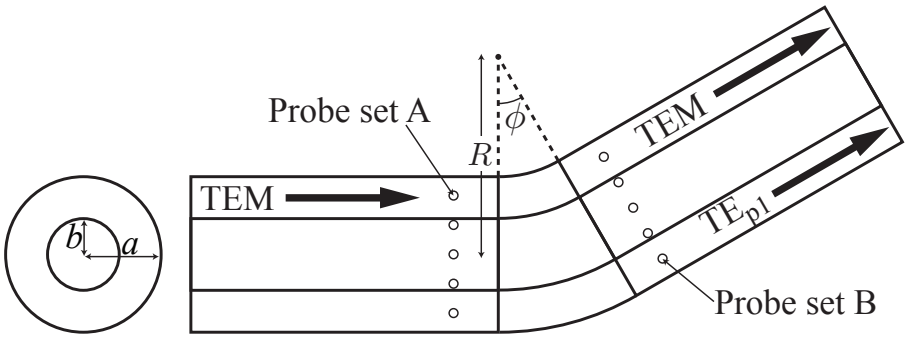

Figure 7.2: Coaxial waveguide with the TEM mode in excitation; it is expected that there will be mode conversion with a proportion of the energy emerging in the modes of the TE_{p1} mode family (TE_{11}, TE_{21}, etc.).

coaxial waveguide, in that both modes are axisymmetric. Similarly, the TM_{11} mode of the circular waveguide is analogous to the TE_{11} mode of the coaxial waveguide, in that both modes are non-axisymmetric with one cycle of variation about the circumference of the waveguide. If coaxial bends behave in a similar manner to circular bends, then it will be expected that both the amplitude and purity of the TEM mode will be affected by the presence of the coaxial bend, thus compromising the overall SCNR.

The objective of this chapter, therefore, is to study the transmission of TEM through a coaxial bend as a function of the bend angle and bend radius to determine whether the transmission coefficient of TEM follows the same trend observed for TE_{01} in the circular waveguide, and if the SCNR past the bend will be sufficient to detect the presence of water. Therefore, this chapter will describe a numerical model used to simulate the scattering of the TEM mode by a bend, followed by a discussion of the results obtained from these simulations. In addition, experimental results will be presented, which provide validation of the simulated results. The results described in this chapter led to a paper in the *Journal of Nondestructive Evaluation* [P5], and are also covered in the QNDE 2011 conference proceedings [P3].

7.1 Numerical Simulations of Bends

7.1.1 The Bend Model

A model was created in Microwave Studio using the same method as described in previous sections. The coaxial waveguide consisted of three coaxial waveguide components formed from vacuum within the PEC background material. The first was a straight section formed from an annular cylindrical shape with dimensions $a = 157.5\,\text{mm}$, $b = 80\,\text{mm}$, and a length $l_1 = 400\,\text{mm}$. The second component was the bend; this was formed from an annular toroidal shape with the same cross-sectional dimensions as the annular cylinder. In order to independently investigate the effects of the bend dimensions, the bend component was parameterised with the angular extent of the bend denoted by ϕ and the radius of curvature denoted by R, as shown in Figure 7.2. The third component was a second straight section, positioned at the distal end of the toroidal bend component, and this had a length, $l_2 = 1000\,\text{mm}$. For excitation, a waveguide port was created at the proximal end of the first straight, with the distal end of the second straight terminating in a short circuit due to the PEC background material. A short circuit termination is used rather than a waveguide port at this end due to the requirement for the ports to be aligned with the hexahedral grid, which is not possible for the majority of bend angles. Once again, a frequency range of 0 to 1.9 GHz was used for the simulation. As the bend was parameterised, the total number of mesh cells in the model increased as a function of both the bend angle and the bend radius, due to the increase in the total volume of the model, with the minimum and maximum number of mesh cells used being 1.2×10^5 and 1.2×10^7, respectively.

To determine the effect of the bend on an incident TEM wave, the electric field was monitored just before the bend and just after the bend. This was done by placing an array of electric field probes (a probe allows the three Cartesian components of the electric or magnetic field at that point to be measured and output) about the circumference of the waveguide at a point 50 mm before the start of the toroidal bend section (probe set A in Figure 7.2), and another array of probes at a point

50 mm after the end of the bend (probe set B). In both cases, the arrays consisted of eight positions at 45° intervals about the circumference. The radial component of the electric field was calculated from the Cartesian components at each of the eight circumferential positions. The eight radial components were then used to study the mode conversion at the bend. Due to the fact that each of the five modes capable of propagating in the waveguide has a different circumferential periodicity in its field distribution, Fourier analysis could be used to separate out the modes. By taking the Fourier transform about the eight circumferential positions, the individual modal contributions were obtained. The TE_{41} mode is the highest order mode that can propagate for these coaxial waveguide dimensions; therefore, eight probes were sufficient to map the total electric field around the circumference whilst avoiding spatial aliasing. Higher-order modes have cutoff frequencies that are above the frequency of operation and are, therefore, evanescent and have no effect on the received signal. These frequency domain modal signals were transformed into the time-domain with TDR. The amplitude of the resultant signal was monitored for each of these modes in order to investigate the process of mode conversion as a function of the bend angle and bend radius parameters. The waveguide port in the simulation model was excited with a pure TEM mode. The modal separation process performed on the electric field at probe set A revealed that all of the energy was in the TEM mode, as expected. The amplitude of the TEM mode recorded at A was used to normalise the amplitude of each of the modes received at probe set B, in order to obtain the transmission coefficient for these modes through the bend.

7.1.2 Numerical Results

The radius of a pipeline bend is typically given as an integer value of the pipe diameter. For instance, a 3D bend is a bend with a radius equal to three times the pipe diameter. It is the inspection of industrial pipelines which is of interest to this investigation; typical industrial pipeline bends have a bend radius of 3D or 5D. For this part of the investigation, a bend radius of 4D is chosen as being representative of the extent of curvature of industrial pipelines. Figure 7.3 shows the amplitude

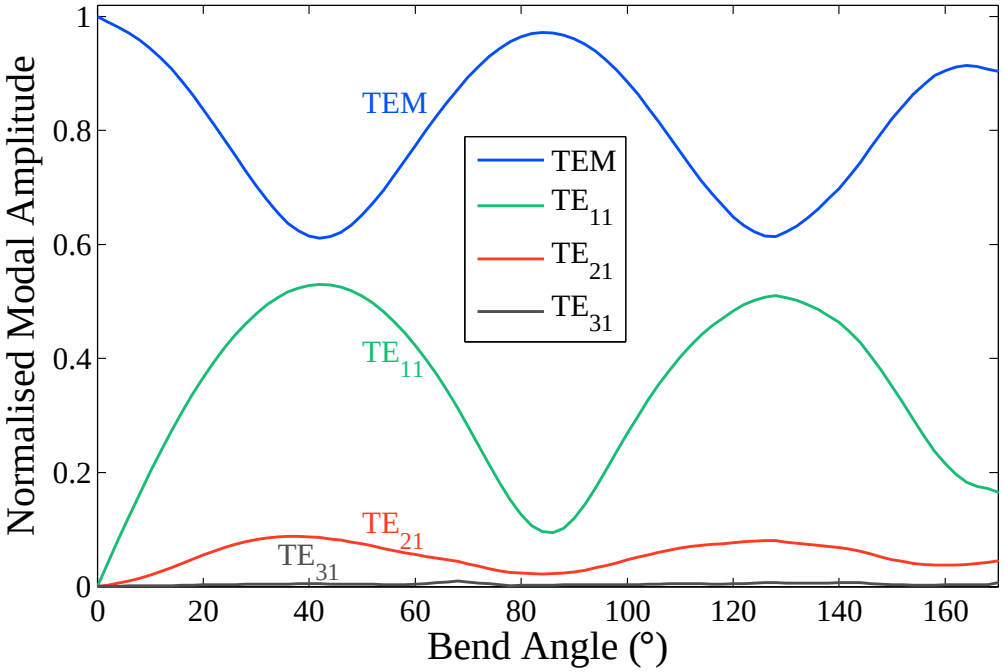

Figure 7.3: Mode conversion in transmission as a function of the bend angle. The amplitudes of the transmitted TEM mode and the first three members of the TE_{p1} mode family are normalized relative to the amplitude of the incident TEM mode. The radius of the outer conductor is, $a = 157.5\,\text{mm}$, and the radius of the inner conductor is, $b = 80\,\text{mm}$. The bend radius is $R = 1260\,\text{mm}$ (4D), which is representative of the curvature of bends found industrially.

of the modes transmitted through a bend with a radius of 1260 mm (4D bend) as a function of the bend angle. There are several modes of the bend which emerge from the end of the bend, and these modes closely resemble the modes of the TE_{p1} mode family, and hence are labelled according to this nomenclature in Figure 7.3. The two major modal components of the transmitted signal are TEM and TE_{11}. As the bend angle increases from 0 to 170°, the TEM transmission coefficient undergoes two cycles of oscillation between 60 and 100 %, with minima occurring at 42° and 128°. These are the angles of maximum mode conversion and lead to maxima in the amplitude of the TE_{11} transmission coefficient by energy conservation. The TE_{21} mode also gains a small proportion of the energy from the TEM mode, with a periodicity similar to that of the TE_{11} mode but with much lower amplitude.

Figure 7.4 shows the transmission coefficient of the TEM mode as a function of

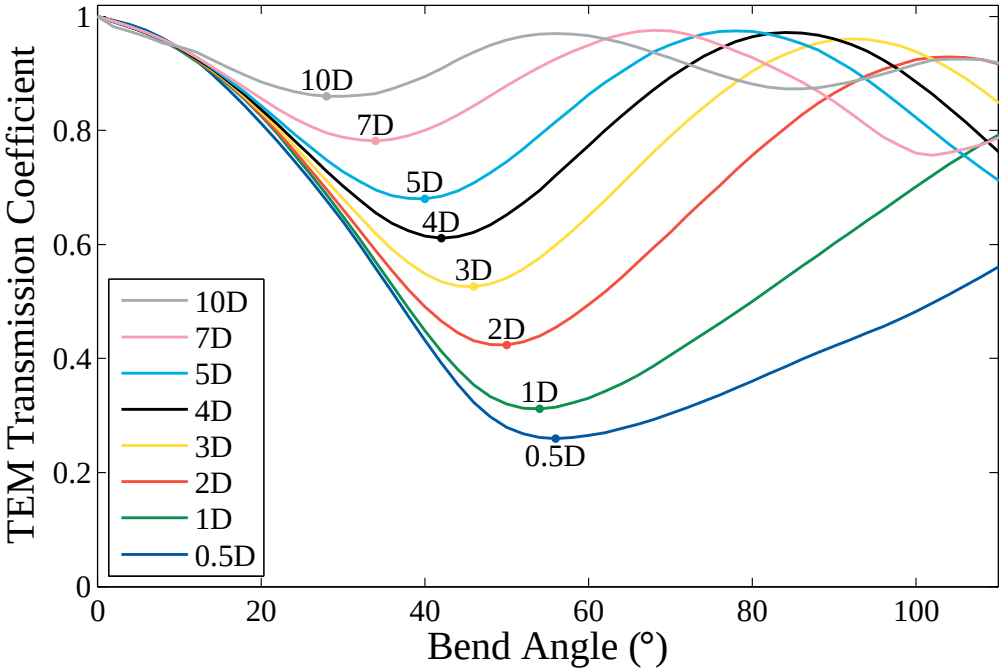

Figure 7.4: Comparison of the modal amplitude of the transmitted TEM mode as a function of bend angle for bend radii increasing from 0.5D to 10D. The extent of mode conversion is greater for sharper bends.

bend angle, for several bend radii ranging from a 0.5D bend to a 10D bend. It can be seen that the extent to which the transmission of TEM is affected by the bend is a function of the bend radius, with sharper bends having a much greater effect than shallow bends. This can be quantified by looking at the minimum transmission coefficient for the two extreme cases: a 0.5D bend and a 10D bend; the values for which are 26 % and 86 % respectively.

In an industrially representative bend with a 4D bend radius, as shown in Figure 7.3, the transmission coefficient of TEM oscillates between 60 % and 100 %, whilst the amplitude of the TE_{11} mode oscillates between 0 % and 50 % and TE_{21} varies from 0 % to 10 %, with the amplitudes of the higher order modes of the TE_{p1} family being too low to be discernible. The most common bend angle found industrially is a 90° bend, and from Figure 7.4 it can be seen that for 3D and 5D bends the transmission coefficients of TEM at 90° are 96 % and 93 % respectively. The high transmission of TEM at representative bend radii of 3D and 5D means that the amplitude of the signal will not deteriorate, whilst the relatively low amplitudes of the TE_{p1} modes,

indicates that the coherent noise level will not increase. Together, this means that a high SCNR can be preserved across such bends and, thus, mode conversion is not a significant problem.

The oscillation of energy between the TEM mode and the modes of the TE_{p1} family is similar to what was described in circular waveguide bends by Jouguet in [81] and Miller in [82]. However, the scattering process is more complex for the case of a coaxial waveguide bend than for circular waveguides. Besides the presence of mode conversion into multiple modes, the transmission coefficients are dependent on the bend radius, as can be seen in Figure 7.4. Note that in Jouguet's relationship, shown in Equation (7.1), the angle of maximum mode conversion, ϕ_c, is independent of the radius of the bend.

The reason for the additional complexity present in the case of coaxial waveguide bends is that, while for circular waveguides there are only two modes travelling in the bend, in the case of a coaxial bend there are multiple modes propagating and the characteristics of these modes vary with the bend radius. To appreciate this complexity one needs to consider the dispersion characteristics of the guided modes travelling in the bend. Chapter 3 described the analytical solution which exists for plotting the dispersion curves of the modes in straight coaxial waveguides; however, no solution exists for the modes in bent coaxial waveguides. Therefore, Microwave Studio was used to obtain data for plotting these dispersion curves; full details of the method used are included in Appendix B.

Figure 7.5(a) provides the dispersion curves for the modes propagating in the bend showing the dependence between frequency and wavenumber. The corresponding phase velocity dispersion curves are shown in red in Figure 7.5(b), with those for a 2D bend plotted alongside in green. The dispersion curves for a straight coaxial waveguide are also plotted, for comparison. The modes in the bend are labelled by analogy with the nomenclature used for the straight coaxial pipe, although it is understood that the modes are different. The colour-scale in Figure 7.5(a), illustrates the relative amplitude of the modes that are actually excited within the bend by the incident TEM. Therefore, from Figure 7.5(a) it is clear that there are at least four

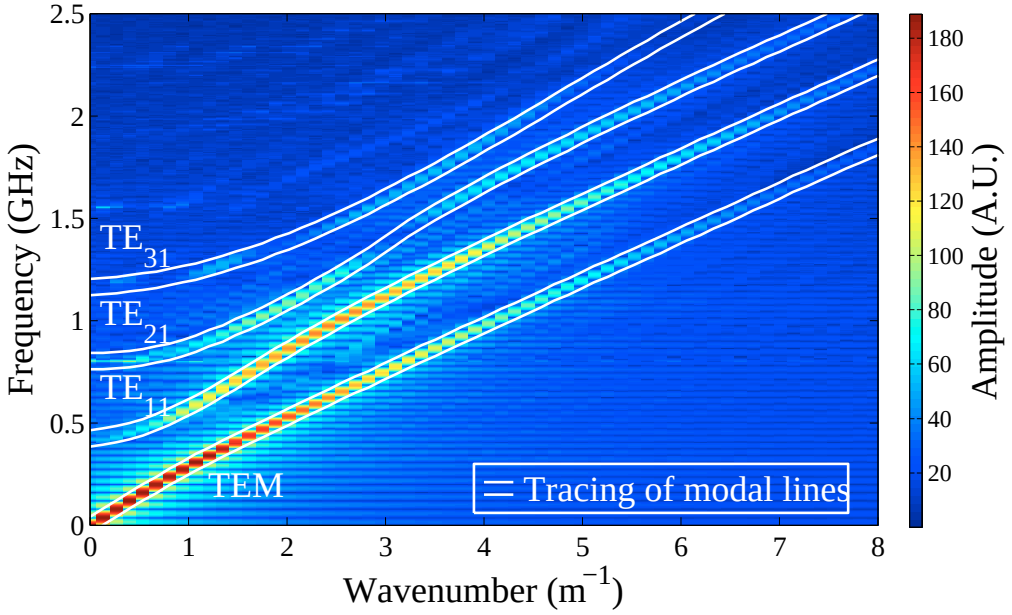

(a) Coaxial waveguide with a 1D bend radius, exciting TEM mode only

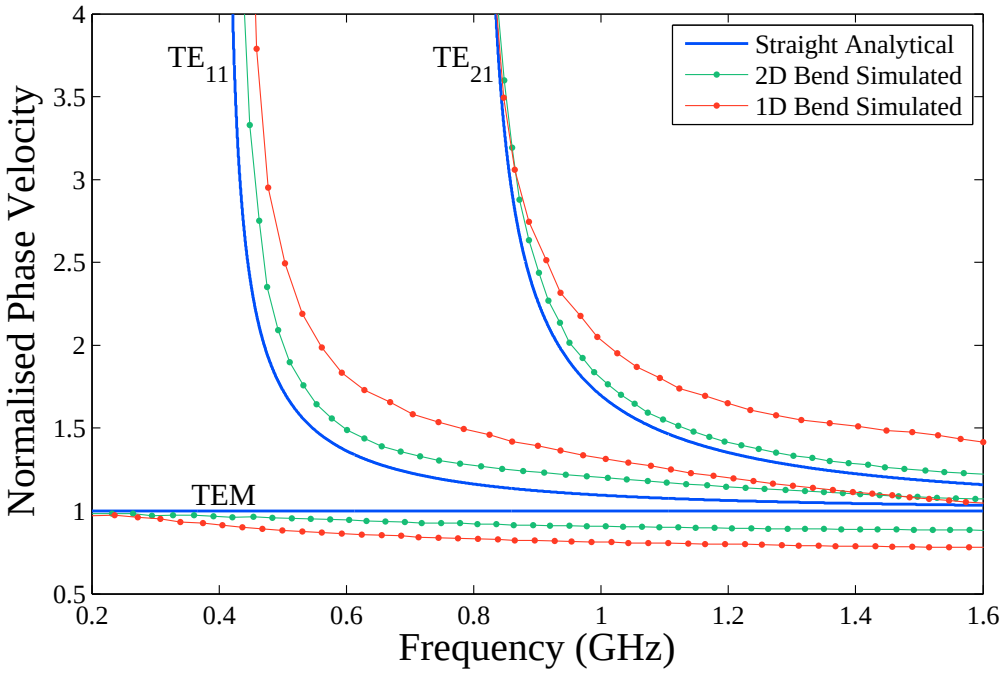

(b) Dispersion curves for modes in coaxial waveguides with bends of 1D and 2D

Figure 7.5: (a) Frequency-wavenumber dispersion curves displaying the modal components which propagate inside a 1D bend, despite only the TEM mode being excited. (b) Dispersion curves for a 1D bend and a 2D bend. From comparison with the dispersion curves for the straight waveguide, it can be seen that phase velocity of the modes is affected by the curvature of the bend, in particular the TEM mode becomes dispersive.

different modes travelling inside the bend, in contrast to the two modes considered by Jouguet in the circular bend. Moreover, the bend alters the phase velocity of each mode. Notably, the TEM mode becomes dispersive, as can be seen in Figure 7.5(b), and the deviation from the straight case increases as the bend becomes sharper.

7.1.3 Effect of Pipeline Dimensions

The simulated results described above were calculated for a coaxial waveguide with $a = 157.5\,\text{mm}$ and $b = 80\,\text{mm}$, which is approximately equivalent to a 6" pipe with 3" insulation; however, there are many other pipeline specifications which could be encountered. Some typical pipeline diameters and insulation thicknesses were used to obtain optimum antenna designs in Section 4.5; the same pipeline specifications will be used here to investigate the effect on the TEM transmission coefficient. Simulations were performed to obtain the TEM transmission coefficient as a function of bend angle for bend radii of 3D and 5D, for pipeline diameters of 4, 6, 8, 12, 18, and 24", and for insulation thicknesses of 1, 2, 3, and 4". The data is summarised by taking the TEM transmission coefficients at 45° and 90° bend angles and plotting these for all pipe diameters and insulation thicknesses, as shown in Figure 7.6.

It can be seen from Figure 7.6 that the insulation thickness does not have a significant effect on the transmission coefficient; however, as the pipe diameter increases, the transmission coefficient of the TEM mode through the bend decreases. For instance, a bend with an angle of 90° and a 3D bend radius, the transmission in a 4" pipe with 4" insulation is 98 %, but this decreases to 68 % as the pipe diameter increases to 24". This effect is more pronounced in the shallower 5D bend than for 3D bends. If we take the example of a 90° bend in a 24" pipe with 4" insulation, the transmission coefficient drops from 68 % to 37 % when the bend radius is increased from 3D to 5D. The transmission coefficient is usually lower for 45° bends than for 90° bends; for example a 45° bend with a radius of 3D in a 24" pipe with 4" insulation has a transmission coefficient of 33 % compared to the 90° value of 68 %. However, this is

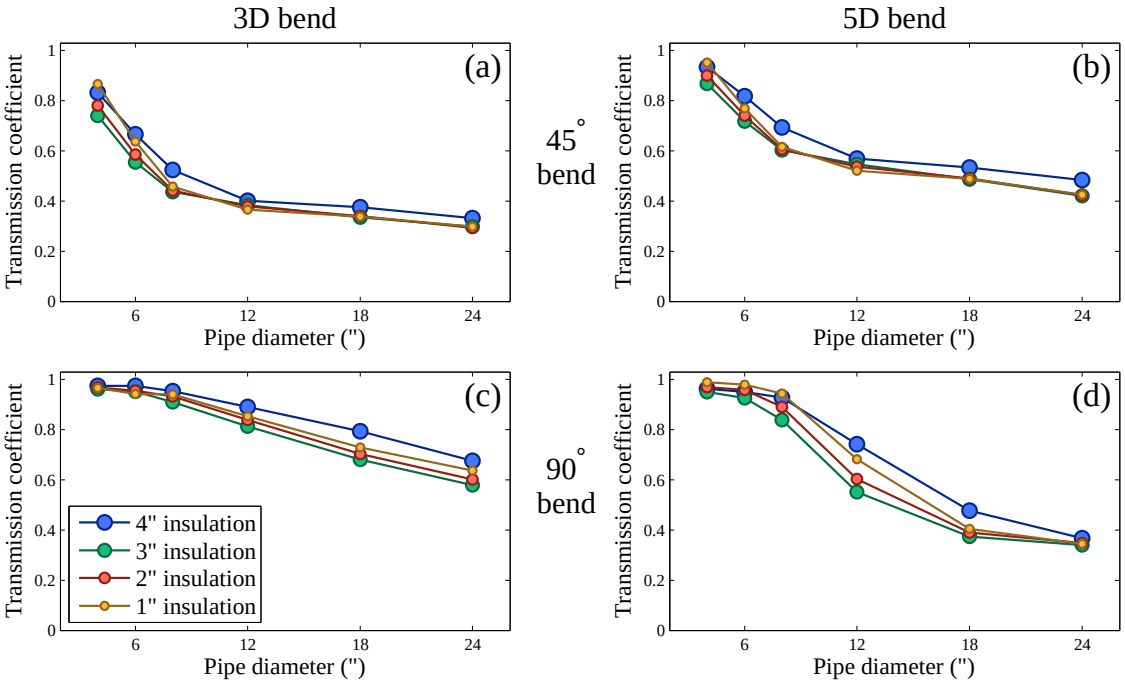

Figure 7.6: The TEM transmission coefficient as a function of pipe diameter and insulation thickness for bend angles of 45° (top plots) and 90° (bottom plots), and for bend radii of 3D (left-hand plots) and 5D (right-hand plots).

not always the case, as a bend with a radius of 5D in the same 24" pipe with 4", has a transmission coefficient of 48 % at 45°, whilst the value is only 37 % at 90°.

In order to understand this behaviour, Figure 7.7 plots the TEM transmission coefficient as a function of bend angle for 3D and 5D bend radii for pipe diameters of 4, 8, and 24" (only three of the six pipe diameters are plotted for clarity) and an insulation thickness of 2" (the insulation thickness does not have a significant effect on the transmission coefficient). If we look at the second maximum in the TEM transmission coefficient, it can be seen that the amplitude of this maximum decreases as the pipe diameter increases, but more significantly, the position of the maximum moves towards lower bend angles as the pipe diameter increases. This can be quantified by looking at the case of 3D bends, the position of the second maximum occurs at 100° in a 4" pipe, 90° in a 8" pipe, and at 80° in a 24" pipe. Whilst this second maximum is located at an angle which is conveniently close to the most common bend angle of 90° for small pipe diameters, as the periodicity

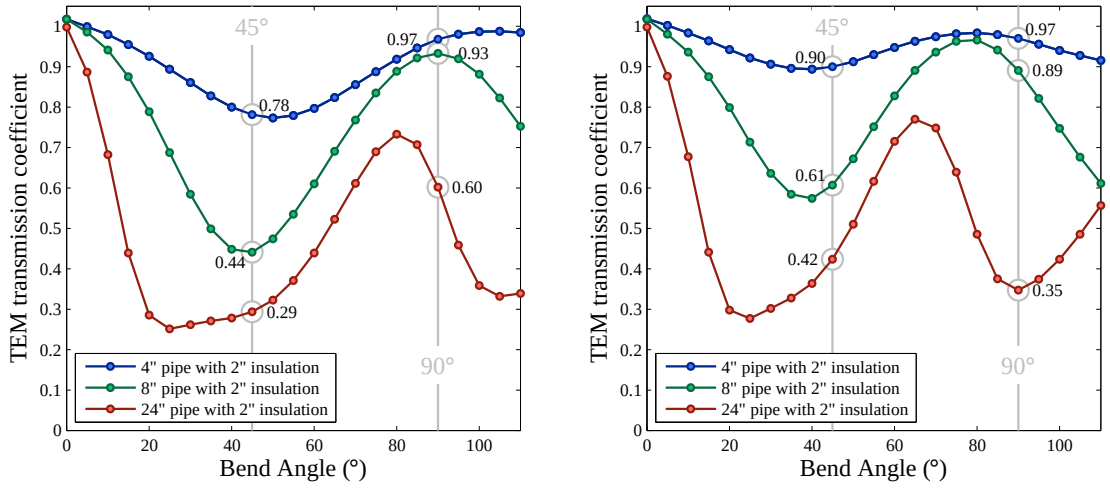

(a) 3D bend radius

(b) 5D bend radius

Figure 7.7: Plots displaying the TEM transmission coefficient as a function of bend angle for 3D and 5D bends in pipes with diameters of 4, 8, and 24" pipes with 2" of insulation. As the pipe diameter increases, the extent of the mode conversion increases, whilst the periodicity of the oscillation of energy between the modes becomes shorter.

decreases the position of the maximum moves further away from 90°, which causes the TEM transmission coefficient at 90° to decrease as the pipe diameter increases.

7.2 Experimental Validation

This investigation has relied on numerical simulations of the behaviour of bends, therefore, validation was sought by performing an experiment involving a coaxial waveguide bend. A photograph of this experimental setup is shown in Figure 7.8(a). The setup used the same ducting as was used in previous experiments to form the straight sections of coaxial waveguide, however, a new component was required to act as the bend. Rigid preformed ducting bends were unsuitable due to the limited range of angles available providing insufficient discretisation of the bend angle. Instead, flexible ducting constructed from thin sheet aluminium (Tecflex 500 from Lindab [72]) was used, the walls of which are manufactured with concertina pleats allowing the duct to be easily bent to any desired angle, as shown in Figure 7.8(b). The setup

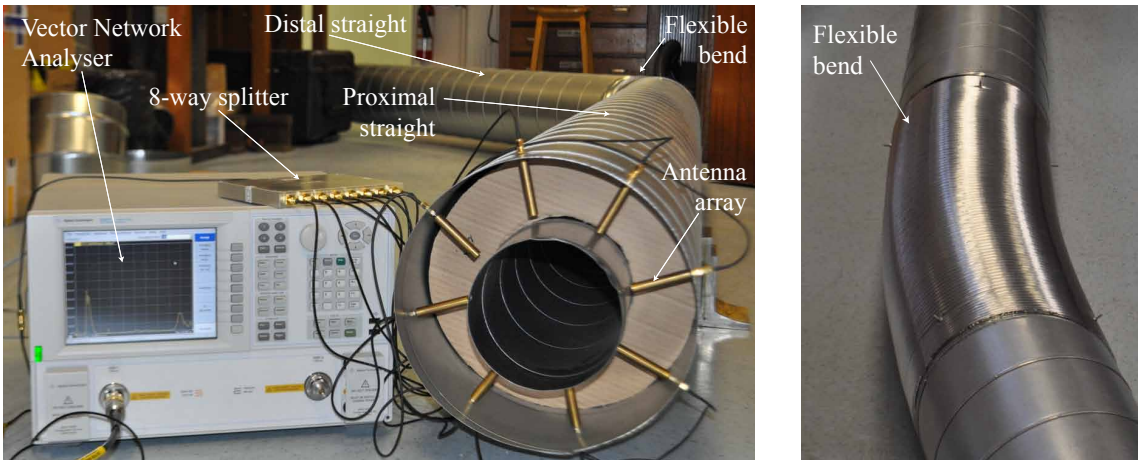

(a) Photograph of the experimental setup

(b) Flexible ducting bend

Figure 7.8: This experimental validation uses the same equipment as in previous experiments. Two straight 3 m lengths of ducting were connected by a 1 m length of flexible metallic ducting, allowing the angle of the bend to be varied.

comprised two 3 m straight lengths of ducting, and in between these two straight lengths, a 1 m length of flexible ducting was connected, as shown in Figure 7.9. This arrangement allowed the second straight length to be moved in an arc, such that the angle of the bend formed by the flexible ducting was varied. Due to the increased degree of movement involved in this experiment, a robust method of supporting the inner ducts concentrically within the outer ducts was employed; this involved a set of four threaded nylon rods positioned at each of the ends of both straight sections. Due to the slight reflectivity of the material, the rods gave rise to a small reflection, as will be seen in the signals from this experiment. In order to be able to monitor the transmission coefficient of the TEM mode in the experiment, a second set of antennas, identical to the first, was installed in the second straight, 500 mm beyond the bend. A separation of 500 mm was required due to the presence of the coupling section connecting the bend to the straight, and the supporting nylon rods, which require the antennas to be installed further from the bend than the 50 mm of separation employed in the simulation model. The eight cables from the antennas in this second array were connected to a second 8-way splitter, the single output from which was connected to port 2 of the VNA, as shown in Figure 7.9. In this manner the S_{21} scattering parameter can be measured by the VNA, and the amplitude of

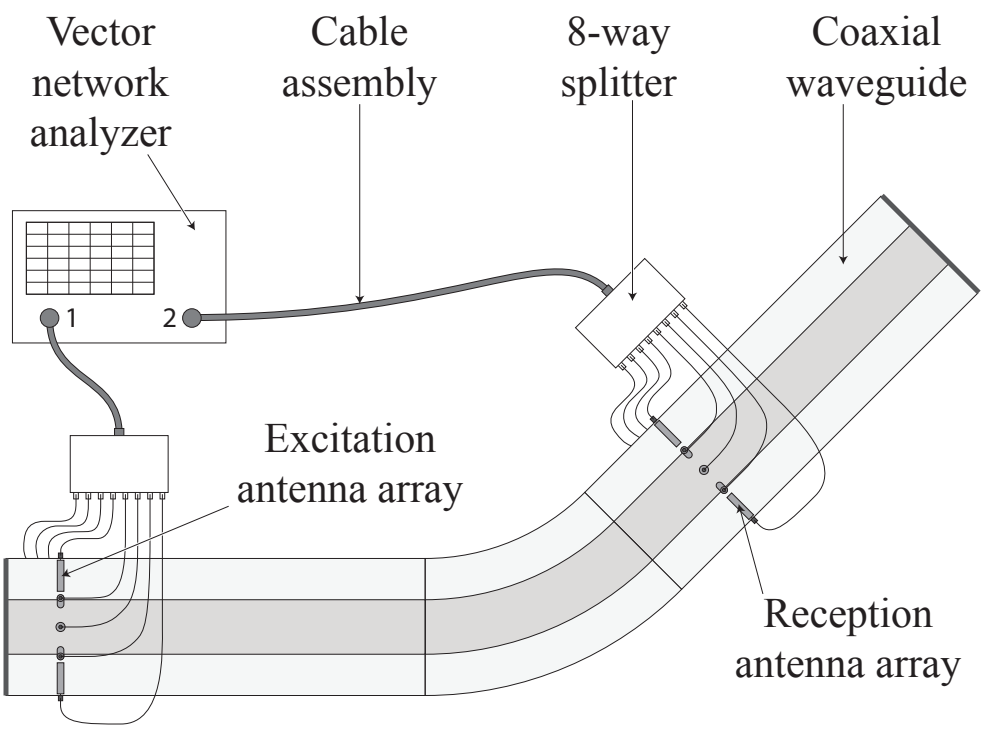

Figure 7.9: Diagram of the experimental setup used to investigate the effect of varying bend angle on the transmission coefficient of the TEM mode.

the pitch-catch signal received at the second set of antennas can be monitored as the angle of the flexible bend is varied.

Example signals obtained from this experiment are shown in Figure 7.10. Figure 7.10(a) is the signal from the first antenna array, received at port 1 (S_{11} scattering parameter), for a bend angle of 0°. At 0 m there is a large reflection, which is due to the impedance mismatch at the antennas caused by the signal propagating from the feeding cables into the large coaxial waveguide. The flexible bend begins at 3 m, and ends at 4 m; there is a higher level of noise in this region, due to the two sets of nylon rods that support the end of the first straight section and the beginning of the second section as well as the small discontinuities caused by the connections between the ducting sections. At 4.5 m there is a peak which corresponds to the position of the second set of antennas. Energy incident on this set of antennas is partially reflected, giving rise to the peak at 4.5 m, and transmitted, going on to reflect from the end of the waveguide causing the peak at 7 m.

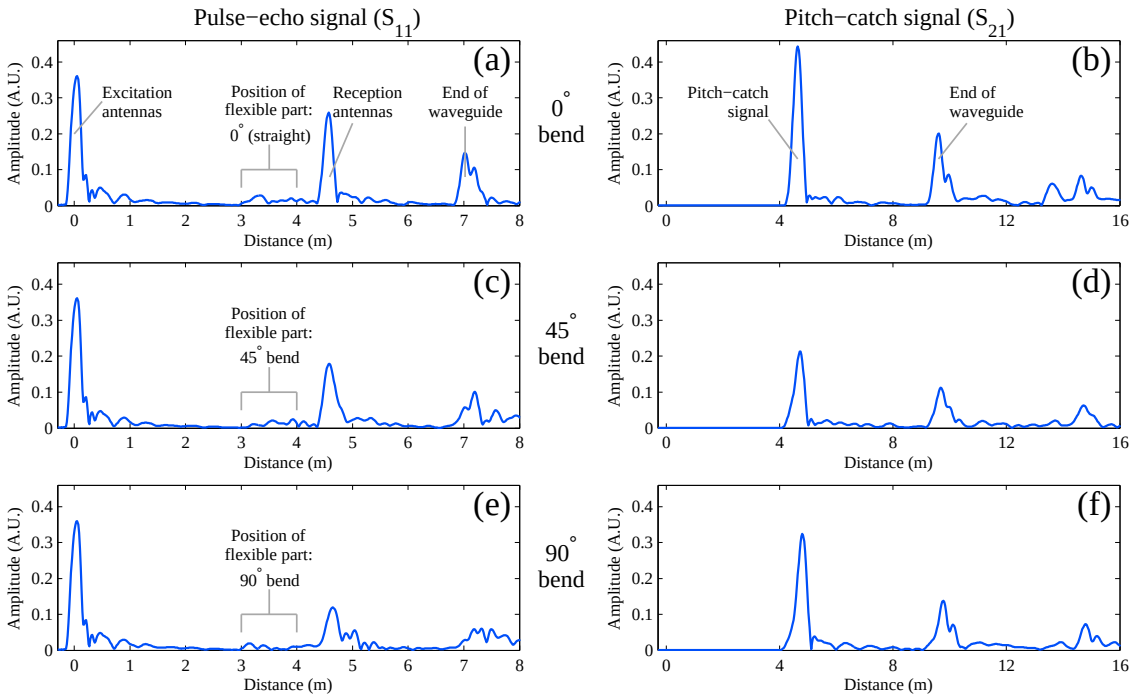

Figure 7.10: Three examples of signals obtained from this experiment; bend angles of 0°, 45°, and 90° are shown. The left-hand plots display the pulse-echo signals obtained from the S_{11} scattering parameter, whilst the right-hand plots display the pitch-catch signals from the S_{21} scattering parameter. It can be seen that increasing the bend angle does not cause peaks to appear in the region of the bend, which means that bends do not cause any significant reflection.

Figure 7.10(c) shows the S_{11} TDR signal for a 45° bend angle, whilst Figure 7.10(e) displays the same signal but for a bend angle of 90°. It can be seen from these three signals that the presence of a bend does not cause any significant reflection, even when the bend angle is increased from 45 to 90°; there are no discernible peaks at the points at which the bend begins and ends, at 3 m and 4 m. This contributes to the value of the technique as an inspection tool, as it means that any water that has accumulated at the bend (and bends are a likely location for water accumulation) will be readily detectable and not masked by a large reflection due to the bend itself.

Figures 7.10(b), (d), and (f) display the TDR signals of the S_{21} scattering parameters, for bend angles of 0, 45 and 90°, respectively. These pitch-catch signals pass through the bend only once, thus enabling the transmission coefficient of the bend to be determined. In Figure 7.10 the peak at 4.5 m is due to the excitation signal from

the first set of antennas directly propagating along the waveguide, through the bend, to be received by the second set of antennas and returned to port 2 of the VNA. The peak at 9.5 m is due to a signal which was transmitted beyond the second set of antennas to be reflected from the end of the waveguide, and received by these antennas on its return. This signal therefore travels a total distance $4.5 + 2 \times 2.5 = 9.5$ m which is different from the true position of the second end-cap at 7 m.

The transmission coefficient of the bend is taken as the amplitude of the pitch-catch signal for a particular bend angle, divided by the amplitude of the pitch-catch signal with the bend in the 0° position, as in Figure 7.10(b). Comparing Figure 7.10(b) to Figure 7.10(d) reveals a reduction in the amplitude of the transmitted signal at 4.5 m to 50 % of its 0° value. This is due to mode conversion at the bend transferring energy from the TEM mode into higher order modes. Despite the mode conversion at the bend, the signal remains clearly discernible, even for this bend angle of 45°, which is in the range of angles at which maximum mode conversion occurs. Increasing the

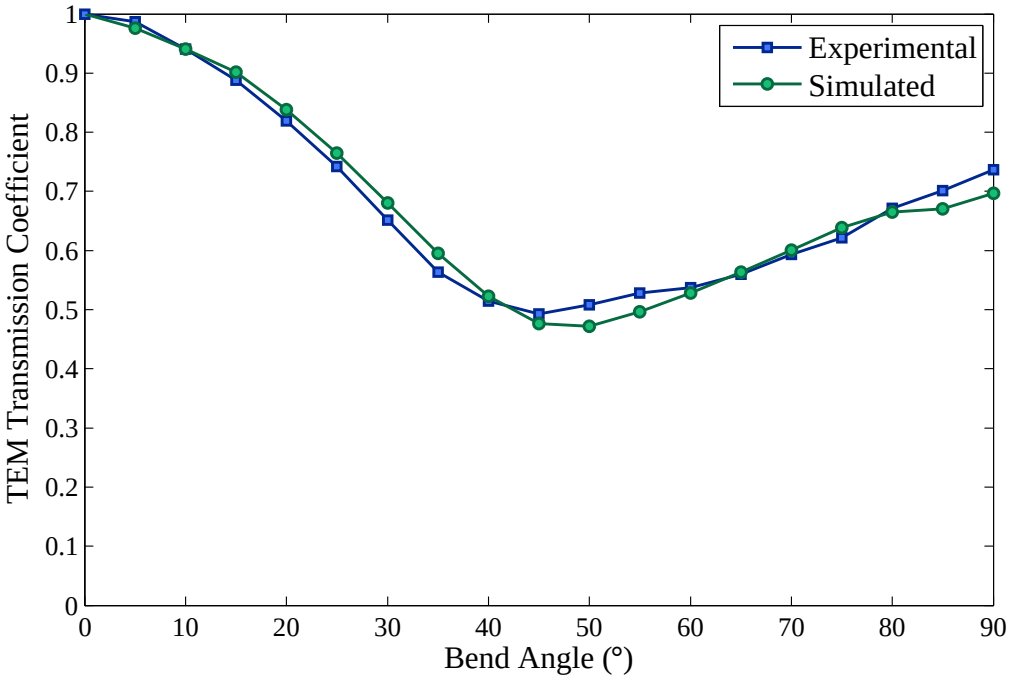

Figure 7.11: Experimentally measured transmission coefficient of the TEM mode versus bend angle, including comparison with numerical simulations. The excellent agreement between the datasets provides validation for the accuracy of the simulations.

bend angle from 45° to 90°, as shown in Figure 7.10(f), causes the amplitude of the transmitted signal to increase once again, back to 75 % of its 0° value. It is worth noting that the flexible bend has a fixed length of 1 m, causing the bend radius to be inversely proportional to the bend angle as $R \propto 1/\phi$. Therefore, increasing the bend angle has the effect of decreasing the bend radius, which means that the amplitude of the transmitted signal at 90° is lower than it would be if it were possible to maintain a constant bend radius throughout the experiment, with a transmission coefficient of 74 %. The fixed length of the flexible bend restricts the outer circumference of the bend to 1 m, causing the bend radius at 90° to reduce to approximately 1.5D. From examination of Figure 7.4, it can be seen that the transmission coefficient for a 1.5D bend radius at 90° would be approximately 75 %, which is in good agreement with the experimental results.

This experimental setup was used to obtain the transmission coefficient for bend angles from 0 to 90° in 5° steps. The results of this experiment are shown in Figure 7.11 as a blue line with square markers. It can be seen that the oscillatory behaviour of the TEM mode is observed again here. This is due to the energy from the TEM mode being converted into higher order modes, with maximum mode conversion occurring at angles between 40° and 60°. The shape of the curve exhibited by these experimental results is slightly different to that observed in the simulations of Section 7.1.2, due to the bend radius decreasing as the bend angle increases. However, if simulations are performed in which the bend radius and angle are varied to match those of the experimental setup for each bend angle, then these simulations (shown as a green line and circular markers in Figure 7.11) display excellent agreement with the experimental results. This agreement between the datasets provides validation for the results obtained in Section 7.1, and also a potential correction method for practical inspection.

7.3 Summary

Having determined that this guided microwave technique is very sensitive to the presence of water in the previous chapter, subsequent development of the technique is focussed on issues regarding implementation of the method on realistic pipelines. Bends are a common feature in industrial insulated pipelines, therefore the practical feasibility of using guided microwaves for pipeline inspection is dependent on the ability of the TEM mode to transmit through bends whilst retaining a sufficiently high SCNR to detect water features. Therefore this chapter has investigated the effect of bends on the transmitted microwave signal.

It was found that the transmission coefficient of the TEM mode through a bend in a coaxial waveguide exhibits an oscillatory behavior as the bend angle increases from 0 to 180°. The oscillations cause transmission minima and maxima, which are due to mode conversion of the incident TEM mode into non-axisymmetric modes of the TE_{p1} mode family. TEM transmission minima correspond to maxima in the amplitude of the TE_{p1} modes emerging from the bend, with the extent of the mode conversion decreasing as the bend becomes shallower (as the bend radius increases). These results are consistent with the scattering theory developed for shallow bends in circular waveguides. However, the coaxial waveguide case shows a higher degree of complexity due to the presence of a larger number of propagating modes that contribute to the mode conversion. By plotting the dispersion curves for modes propagating within bent coaxial waveguides, it is shown that the dispersion characteristics of the modes are affected by the curvature of the waveguide, with sharper bends having a greater effect. In particular, the TEM mode becomes dispersive, with a phase velocity that decreases with increasing frequency, and a group velocity that experiences an even greater decrease as a function of frequency.

It is worth bearing in mind that energy propagating through a bend will spend some of its time in non-axisymmetric modes, such as the TE_{11} mode. The energy of these modes is less evenly distributed than for the TEM mode, resulting in regions of the modal field distribution in which there is very little energy, as can be seen

in Figure 3.4(b). If there is a water volume located in a bend, it is possible that the water could be located in such a minimum of the field distribution, resulting in very low detectability of water volumes at such locations. Conversely, the water volume could be located at a maximum in the field distribution resulting in very high detectability. Further work would be required in order to understand the extent of this effect.

Industrial insulated pipelines have bends with radii that are typically either 3D or 5D; the pipeline itself can have a wide variety of pipe diameters and insulation thicknesses. For a 3D bend, the transmission coefficient of the TEM mode for bend angles of 90° decreases with pipe diameter, but remains above 60 %, whilst for the 5D bend, the transmission coefficient shows a wider range of variation, decreasing from 99 % to 34 % as the pipe diameter increases from 4" to 24", respectively. For small pipe diameters, those that are 8" or less, and for 90° bends (the most commonly encountered bend angle) the transmission coefficient is typically between 99 % and 90 %, indicating that the guided microwave technique will be almost unaffected by the presence of typical industrial bends in pipelines of these dimensions. Larger pipeline sizes, in the range 12" to 24", demonstrate transmission coefficients that are between 90 % and 34 %, the latter of which would cause an attenuation of the microwave signal which would render inspecting beyond such bends impractical.

The simulated results were validated by performing a set of laboratory experiments; excellent agreement was observed. Experimental results indicated that there is very little reflection from the interface between a straight section of waveguide and a bend, which is ideal for the detection of water volumes within a bend itself.

Chapter 8

The Effect of Pipe Supports

Whilst the previous chapter described the effect of bends in the pipeline, this chapter continues the investigation into the effect of common pipeline features that could affect the guided microwave signal, by studying the case of a typical pipe support. The type of support employed on a pipeline depends on the type of insulation that is used. In Section 5.4, some common types of insulation were described. In Alaska, the pipelines are typically insulated with polyurethane foam insulation. This insulation is applied to the pipe during production, with a length of the pipe at each end deliberately left un-insulated. The complete clad and insulated unit is then transported to its service location, where the pipeline sections are girth-welded together (hence the need for exposed pipe ends). After welding, the insulation and cladding system is completed by installing a *field-joint* at the weld locations, which comprises a cladding jacket wrapped around the exposed section, which is then filled-in with foam insulation. The polyurethane foam insulation has a compressive strength which is high enough to support the weight of the inner pipe by itself. Therefore, the clad and insulated pipeline is supported on saddle-supports, or similar, without any intrusion of the external support into the insulation material. From the perspective of using the guided microwave technique, this form of pipeline design is beneficial, as it means that there are no intrusions into the annular space where the microwaves are propagating, therefore pipe supports will not cause any reflection or attenuation.

For pipelines where rockwool is used for insulation, the system is entirely different. The pipe is installed in position with supports, in the form of steel plate welded to the 6 o'clock position, longitudinally along its length, fitted where the loading on the pipe requires them. The rockwool insulation is fitted subsequently, usually by a different contractor, followed by the cladding. This means that the insulation and cladding are required to be fitted around the pipe supports welded to the 6 o'clock position of the pipe. This form of pipe support creates a metallic reflector within the annular space of the waveguide, which makes electrical contact between the inner and outer conductors of the waveguide. It could be expected that such a feature would cause significant reflection and attenuation of the microwave signal. This chapter will investigate the extent of the reflection from, and transmission beyond, pipe supports of this type. The results of this study of pipe supports will be presented in a paper submitted to the journal *Insight* [P6].

8.1 Experimental Setup

The form of pipe support which is found on pipelines with rockwool insulation typically has a thickness of approximately 10 mm, and a length, in the axis of the pipeline, of approximately 500 mm. The same basic experimental setup was used as described for previous experiments. The coaxial waveguide had dimensions of $a = 140$ mm and $b = 80$ mm, formed from ventilation ducting approximating a 6" pipe with 2" insulation. A 6 m length of ducting was used, formed from two 3 m lengths coupled together. A schematic diagram of the experimental setup is shown in Figure 8.1. The excitation antenna array was positioned at one end of the ducting, with a second array of antennas, for reception, positioned 500 mm beyond the joint between the two ducting sections. The metallic component used to represent the support had cross-sectional dimensions of 50×10 mm and a length of 600 mm initially, although the length was reduced in 50 mm steps during the course of the experiment in order to observe the effect of changing the length of the support. The support was introduced into the waveguide by separating the two ducting sections and positioning the support within the first length of ducting, with

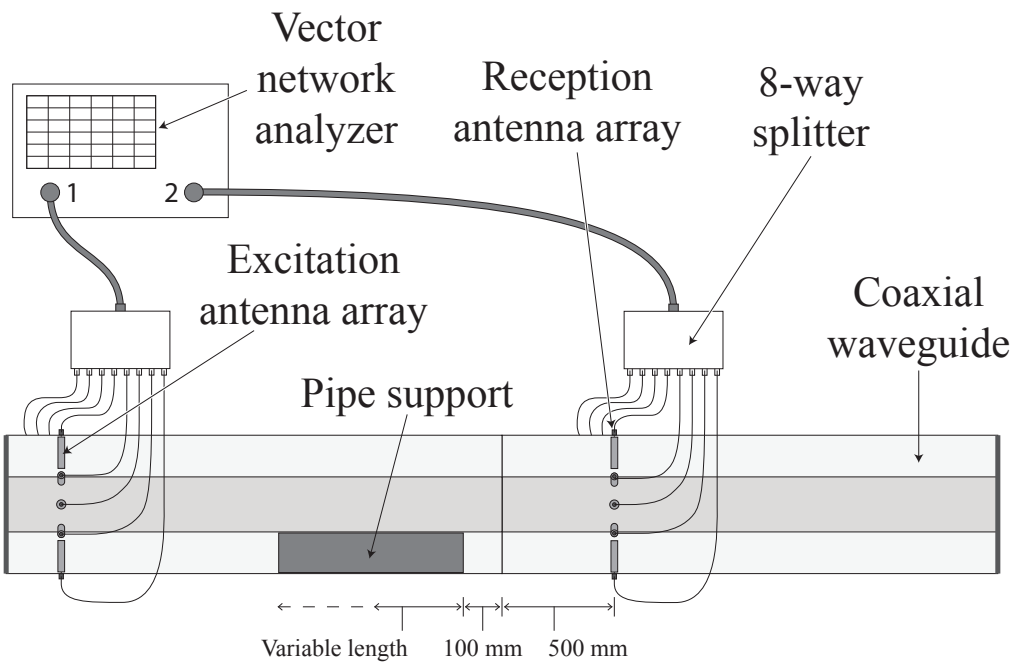

Figure 8.1: Schematic diagram of the experimental setup used to investigate the effect of pipe supports in the waveguide.

a 100 mm gap between the end of the support and the end of the first length of ducting. As the position of the end of the support was fixed, and the length of the support decreased throughout the experiment, the position of the start of the support varied accordingly. Electrical contact of the metallic support with both the inner and the outer ducting was confirmed. Figure 8.2 shows the experiment set up in the laboratory. Using two arrays of antennas enables the measurement of both the S_{11} (pulse-echo) and the S_{21} (pitch-catch) scattering parameters, which allows us to characterise the transmissive properties of the support, in addition to its reflective properties.

8.2 Experimental Results

Three example signals from this experiment are shown in Figure 8.3. The left-hand column of plots displays the pulse-echo signals, whilst the right-hand column of plots displays the pitch-catch signals. Three support lengths are shown in Figure 8.3, with

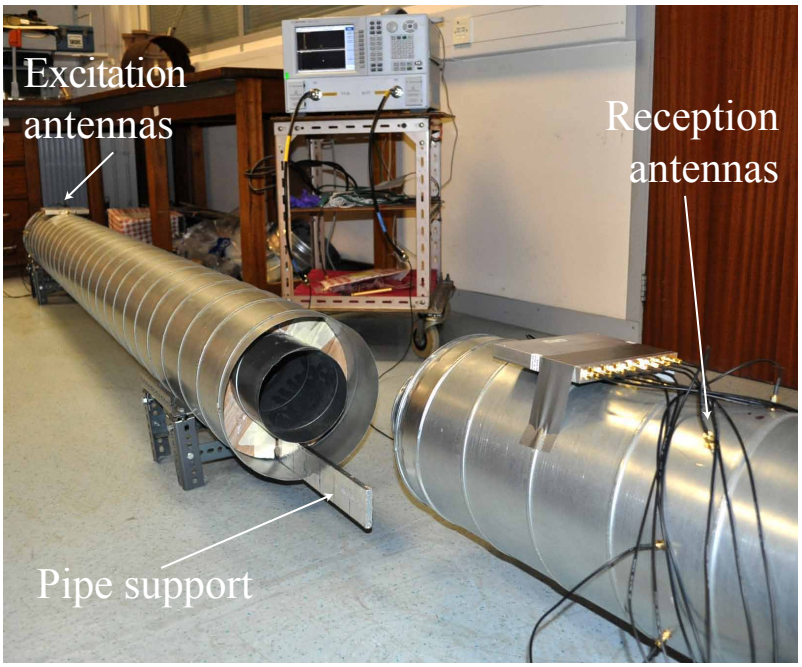

Figure 8.2: Photo of experimental setup used to investigate the effect of pipe supports in the waveguide.

the topmost plots displaying the signal obtained with no support in the waveguide, followed by a support with a length of 300 mm, and finally a length of 500 mm.

Consider Figure 8.3(a): the peak at 0 m corresponds to the reflection from the antennas; the peak at 3.5 m is due to the array of reception antennas which is located at this position; and finally the peak at 6 m is due to the signal reflecting from the short-circuiting metal end-cap terminating the waveguide. The low-amplitude reflection at 3.0 m is due to a component constructed from cardboard, which can be seen in Figure 8.2, which is positioned within the waveguide at this position to maintain the concentricity of the inner duct within the outer, whilst still allowing the metallic support to be introduced into the waveguide. From Figure 8.3(c), it can be seen that there are two small peaks at 2.7 and 3 m which correspond to the reflections from the start and end of the support. Looking now at Figure 8.3(b), the reflection at 3.5 m is due to the signal which propagates directly from the excitation antennas, along the waveguide, to be received at the reception antennas. The second peak at 8.5 m is due to a portion of the signal which propagated beyond the reception

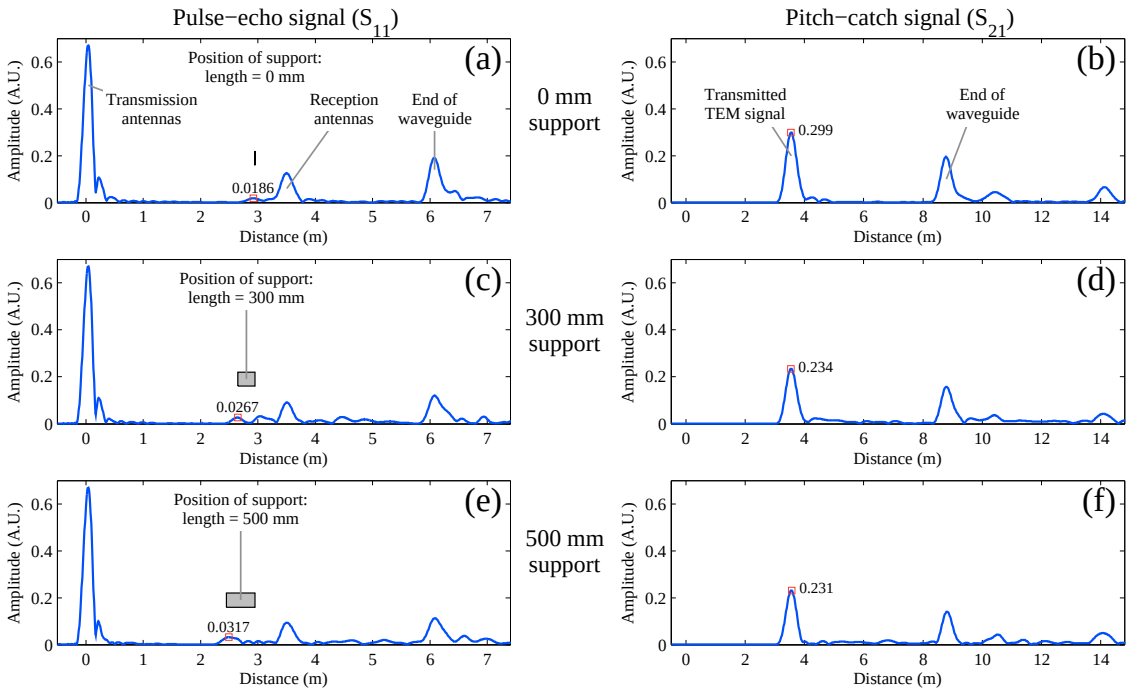

Figure 8.3: Three examples of signals from the experiment in which the length of the pipe support was varied. These signals are for support lengths of 0 mm (empty waveguide), 300 mm, and 500 mm. The left-hand plots display the pulse-echo signals, whilst the right-hand plots display the pitch-catch signals. In the pitch-catch signals, the peak at 3.5 m is used to determine the amplitude of the signal transmitted beyond the support.

antennas, to be reflected from the end of the waveguide and subsequently received at the reception antennas.

The reflection coefficient can be calculated from the amplitude of the reflection from the start of the support (the peak highlighted with a red square in Figures 8.3(a),(c), and (e)) relative to the amplitude of the reflection from the end of an empty 3 m waveguide. Similarly, the transmission coefficient can be obtained from the amplitude of the transmitted TEM signal in Figures 8.3(d) and (f) relative to the amplitude of the same peak in Figure 8.3(b) with no support in the waveguide. These coefficients are plotted in Figure 8.4, alongside data obtained from simulations performed in Microwave Studio.

From Figure 8.4 it can be seen that both the transmission and reflection coefficient

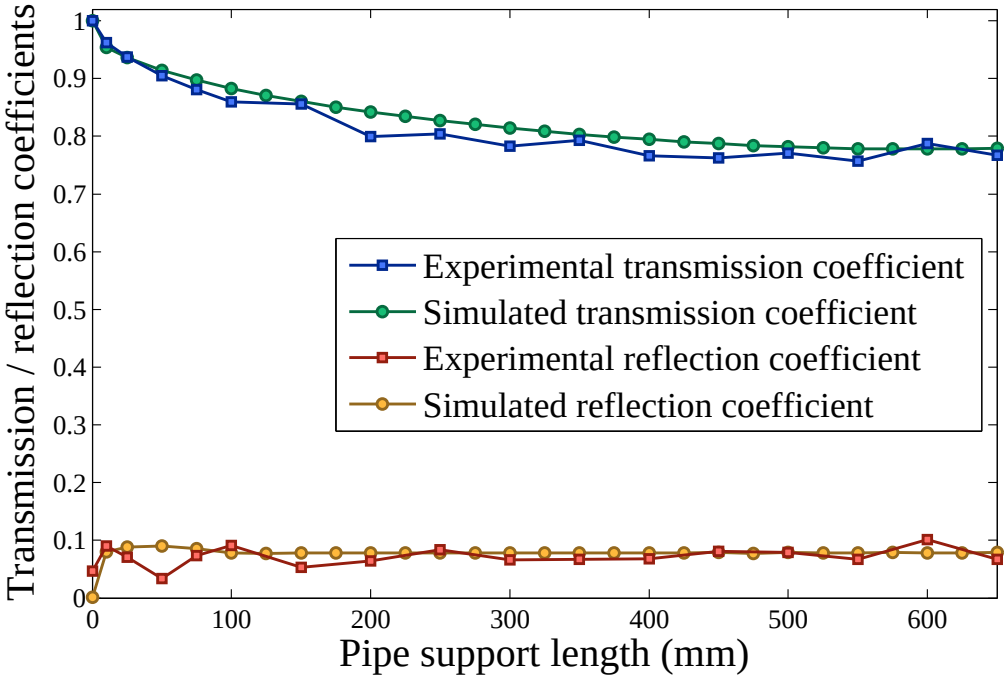

Figure 8.4: The transmission and reflection coefficients of the TEM mode as a function of the length of a pipe support with a thickness of 10 mm and a height equivalent to the annular spacing. Experimental data is compared to results obtained from simulations, and shown to be in good agreement.

data obtained experimentally agree very well with the simulated data, providing validation for the accuracy of the software in simulating this type of waveguide problem. The transmission coefficient decreases as the pipe support increases in length, with the value for a support with a typical length of 500 mm being 77 % measured experimentally, and 78 % according to simulations. The reflection coefficient is primarily determined by the cross-sectional area of the support and is therefore independent of the length of the support. For a support with a length of 500 mm, a value for the reflection coefficient of less than 10 % was calculated for both experimental and simulated results. At the point at which the microwave signal is incident on the non-axisymmetric reflector of the support, partial mode conversion occurs. This causes some of the energy from the TEM mode to be lost to other higher-order modes. This leads to the transmission coefficient being lower than would be expected given the value of the reflection coefficient. From an inspection point of view, a transmission coefficient of just less than 80 % for a pipe support indicates that inspecting

beyond such a feature in the waveguide is feasible. The low value for the reflection coefficient of approximately 10 % for the start of a pipe support indicates that large cross-sectional extents of wet insulation would not be masked by the reflection from the support. In addition, the low reflection coefficient indicates that reverberations between supports should not be significant.

8.3 Summary

This chapter focusses on an investigation into the effect of pipe supports on the guided microwave technique. Some insulation types have sufficient compressive strength that pipe supports are not required, however, for those pipes which do have pipe supports, these are typically in the form of a narrow metallic bridge across the annular space, creating a short circuit between the inner and outer conductors of the coaxial waveguide. The investigation determined the reflective and transmissive properties of this type of support, as a function of its length. It was found that for a typical support length of 500 mm, the reflection coefficient was approximately 10 %, and the transmission coefficient was just under 80 %. Both of these figures indicate the feasibility of inspecting beyond a typical pipe support.

Chapter 9

Conclusions

This thesis has taken the idea of inspecting insulated pipelines with guided microwaves from an initial concept, through to a technique which has demonstrated the feasibility of detecting discontinuities between wet and dry insulation in the conditions which exist on real industrial pipes. The steps that were taken during this development are reviewed in Section 9.1, whilst a summary of the main findings is given in Section 9.2. Finally, a discussion of potential future work to continue the development of this technique is included in Section 9.3.

9.1 Review of Thesis

This thesis has investigated the potential of a guided microwave inspection technique for screening the insulation layer along the length of a pipe to detect the presence of water in the insulation. The value of such an inspection tool lies in the early warning that it would provide of the likely occurrence of corrosion under insulation in the vicinity of the wet insulation, as water is a necessary precursor to corrosion. As discussed in Chapter 1, this form of corrosion is a major cause of pipeline failure, and is very difficult to detect, as the condition of the pipe is obscured by the insulation system. The premise for this guided microwave technique is the use of the structure

of a clad and insulated pipeline as a coaxial waveguide to support the propagation of guided electromagnetic waves.

The theoretical background for the technique is presented in Chapter 2, including an examination of the relatively simple case of electromagnetic waves propagating in a rectangular waveguide in order to introduce some of the concepts of waveguide theory, such as dispersive propagation, and modes of propagation. This chapter also discusses the necessity for numerical simulation software to study complex problems, with an introduction of the Finite Integration Technique. The chapter also provides some background to the Synthetic Time-Domain Reflectometry method, which is used throughout the thesis to transform frequency-domain measurements into the time-domain.

Chapter 3 describes the development of an analytical model to study the propagation of electromagnetic waves within the large coaxial waveguides formed by insulated pipelines. The objective of this model was to obtain sufficient information about the behaviour of microwave propagation in these waveguides to determine the feasibility of inspecting the insulation layer of pipelines with guided microwaves. In determining the feasibility, there are three main requirements of the guided microwave inspection system, which are explained in this chapter: non-dispersive propagation, mode purity, and a broad frequency bandwidth. The latter two of these requirements are conflicting, however, the chapter proposes a technical solution to the problem based on an array of antennas, so that all three of these requirements can be achieved.

The development of the design of the antenna array for the excitation of large coaxial waveguides is covered in Chapter 4. A preliminary experiment was conducted to assess the practical feasibility of the technique. Whilst the results experimentally confirmed that the technique would work, it also revealed that there was a significant impedance mismatch between the coaxial feeding cables and the antenna array. Various methods of impedance matching were investigated, but the most effective technique was found to be the design of the antenna itself. This chapter describes the optimisation of the antenna design with numerical simulations.

Chapter 5 focusses on experimentally validating different aspects of the guided microwave technique. This validation is sought using a model experimental setup that is representative of the coaxial waveguides formed by typical insulated pipelines. Experiments are performed to validate the method of optimising the antenna design using numerical simulations. The model experiment is also used to measure the attenuation coefficients of three types of insulation which are commonly used industrially: rockwool, polyurethane foam, and glass foam. This chapter also describes a field test, which was conducted to validate the accuracy of the model experiments in representing real pipeline conditions.

Determining the sensitivity of the guided microwave technique to the presence of water is crucial in evaluating its effectiveness as an inspection tool, therefore, Chapter 6 presents results from simulations and experiments in which water was gradually introduced into the waveguide. The aim of the experiment is to determine the relationship between the reflection coefficient and the cross-sectional extent occupied by water, and also to determine the minimum amount of water that the technique can detect. This chapter also discusses a field test, in which the technique is used to detect sections of wet insulation on a length of real industrial insulated pipeline.

The value of a long-range, screening inspection tool, such as this guided microwave technique, is linked to the extent to which it is capable of tolerating features in pipelines; features such as bends. Chapter 7 investigates the effect of bends on the microwave signal, by performing simulations of curved coaxial waveguides. Energy that is incident into the bend in the TEM mode undergoes mode conversion to emerge in a combination of higher order modes. This process was characterised for typical industrial pipeline specifications, in order to determine whether the guided microwave technique can be used to inspect beyond bends in such pipelines. Experiments are performed to validate the simulated results.

Pipe supports are another common feature in pipelines fitted with rockwool insulation; pipes insulated with polyurethane foam have supports which exist externally to the cladding. In the case of rockwool insulation, the pipe supports take the form

of a steel plate welded to the bottom of the pipe, which creates a short-circuit between the inner and outer conductors at the 6 o'clock position of the pipe. Chapter 8 describes the measurement of the reflection and transmission coefficients of this type of support as a function of the support length, by performing simulations and experiments.

9.2 Summary of Findings

9.2.1 Achieving a High Signal-to-Noise Ratio

The sensitivity of an inspection technique is dependent on the signal-to-noise ratio. With this guided microwave technique, it is coherent noise which is the limiting factor, so the term signal-to-coherent-noise ratio (SCNR) is used. Whilst a low SCNR results in signals from waveguide features being obscured by the coherent noise, a high SCNR enables low amplitude reflections to be discerned in the signal. This translates into the detection of weakly reflecting features in the waveguide, such as small volumes of water. In order for this guided microwave technique to demonstrate high sensitivity to water volumes in the waveguide, a high SCNR is required. A significant finding of this thesis is that a high SCNR can be achieved in the large coaxial waveguides formed by pipelines.

The first stage of the project was to develop an analytical model describing electromagnetic wave propagation in coaxial waveguides. From this model, it was discovered that there is a mode which propagates non-dispersively: the TEM mode. This mode is the ideal mode to perform an inspection, as the signal will not suffer from temporal spreading due to dispersion. The TEM mode is, therefore, the mode which will allow the SCNR of the technique to be maximised. However, the SCNR will suffer drastically if multiple modes are propagating in the waveguide alongside the TEM mode. From the model, it was found that, for the large coaxial waveguides formed by pipelines, the cutoff frequencies of the lowest modes occur at low frequencies in the range between 60 MHz and 400 MHz. The traditional manner in which

coaxial waveguides are operated, at frequencies below the cutoff of the lowest mode in order to ensure mode purity, would not provide a sufficiently broad bandwidth to obtain good spatial resolution of waveguide features. However, the analytical model also revealed that the modes of the lowest mode family have field distributions which are non-axisymmetric, in contrast to the axisymmetric field distribution of the TEM mode. It was proposed to take advantage of this difference in symmetry to achieve pure-mode excitation of the TEM mode, by using an array of antennas distributed circumferentially about the waveguide to suppress the excitation of higher order modes. In this manner, the SCNR of the guided microwave signal is optimised.

Having devised this approach for the excitation of large coaxial waveguides, an early experiment with a preliminary antenna array design revealed a significant impedance mismatch at the antennas. Through the subsequent investigation of possible means of improving this impedance match, it was discovered that the most effective technique was to vary the length and diameter of the antenna. Numerical simulations of the required number of antennas for exciting a large coaxial waveguide enabled the optimisation of the antenna design for that particular waveguide size.

Two laboratory experiments were performed with coaxial waveguides of different annular thicknesses. These had dimensions representative of a 6" pipe with 3" insulation, and a 6" pipe with 2" insulation. The optimised antenna arrays in these two waveguides demonstrated SCNR values of 40 dB and 42 dB, respectively. That high SCNR values, such as these, can be obtained in large coaxial waveguides operating in a frequency range at which multiple modes are capable of propagating, is a significant result for this guided microwave technique, which is due to thorough design of all aspects of the excitation system, and a comprehensive understanding of the modes of propagation in such waveguides.

9.2.2 High Sensitivity to Water

A further finding of significance described in this thesis is that the guided microwave technique is highly sensitive to the presence of a sharp interface between dry and

wet sections of waveguide. An experiment was conducted in which water was gradually introduced into a plastic tank inside the waveguide. This allowed the smallest detectable volume of water to be determined. The reflection from a 200 ml water volume, equivalent to a 5 % cross-sectional extent of the waveguide, was clearly detectable. The reflection coefficient from a 100 % cross-sectional water volume, was experimentally measured to be 81 %, indicating that a fully saturated section of insulation would give rise to a very strong reflection. Both of these figures indicate that the technique is very sensitive to the presence of water.

A further study of the sensitivity of the technique was conducted during a field test on a section of real industrial insulated pipe. This experiment provided conditions which were more representative of a real inspection, not only because the waveguide was formed from a real pipeline including insulation, but because the water feature being detected was in the form of a section of wet insulation amidst dry insulation, rather than a discrete volume of water in an empty waveguide. The results from this field test experiment revealed that a 100 % cross-sectional section of wet insulation gave rise to a reflection coefficient of 82 %, which is in good agreement with the value measured in the laboratory. The guided microwave technique was capable of detecting the first section of wet insulation which was introduced into the waveguide, which presented a 12.5 % cross-sectional extent of wet insulation, a result which confirms the sensitivity of the technique in the variable conditions which exist in the field.

9.2.3 Robustness to Pipeline Conditions

Having determined the sensitivity of the guided microwave technique to water, the other significant findings described in this thesis focus on investigating aspects of implementation of the technique on real industrial pipelines, such as the effect of common pipeline features. These findings include such issues as: the attenuation of different insulation materials; the effect of bends on the microwave signal; and the reflection and transmission coefficients of typical pipe supports.

By introducing a length of an insulation material into the coaxial waveguide and comparing the amplitude of the reflection from the end of the waveguide relative to the empty waveguide signal, the attenuation coefficient for the insulation material can be determined. This was done for rockwool, polyurethane foam, and glass foam insulations, for which the attenuation coefficients were measured to be $0.2\,\mathrm{dB\,m^{-1}}$, $1.2\,\mathrm{dB\,m^{-1}}$, and $143\,\mathrm{dB\,m^{-1}}$, respectively.

It is worth noting that such attenuation coefficients tend to be strongly frequency-dependent, with higher frequencies experiencing greater attenuation, leading to a reduction in the centre frequency during propagation. The lowering of the centre frequency will consequently alter the overall attenuation experienced by the signal. Due to this complexity, the attenuation of the signal is hard to interpret. The empirical approach adopted here, which was to measure the overall attenuation experienced within the operating frequency range, provides only the attenuation coefficient for that specific frequency range and length of sample. This should be taken into account when using these values to estimate propagation range.

The attenuation experienced in glass foam insulation prohibits the use of this technique on pipes fitted with such insulation; glass foam does not retain water, so this is not a major disadvantage. The attenuation coefficient values for rockwool and polyurethane foam are sufficiently low for the guided microwave technique to be successfully employed on pipes fitted with these types of insulation.

An investigation into the effect of bends on the microwave signal revealed that mode conversion causes energy to be transferred from the incident TEM mode into other higher-order modes. The distribution of energy oscillates from the TEM mode to the higher-order modes, and back again, as a function of bend angle. The most common bend angle is a 90° bend, and the most common bend radii are three and five times the pipe diameter. These common bends were studied for a range of pipe diameters from 4" to 24", and a range of insulation thicknesses. It was found that for small pipe diameters, those that are 8" or less, the transmission coefficient is typically between 99 % and 90 %, which means that the guided microwave technique would be able to inspect beyond such bends without adverse affects to the signal.

However, larger pipeline sizes, in the range between 12" and 24", demonstrate transmission coefficients that are between 90 % and 34 %, the latter of which would cause an attenuation of the microwave signal which would render inspecting beyond such bends impractical. Significantly, it was found that the interface between a straight section and a bend does not give rise to a reflection, which means that any water that has accumulated at a bend will be readily detectable and not masked by a reflection from the bend.

By performing experiments and simulations, the effect of a typical pipe support on a rockwool-insulated pipeline was characterised as a function of length. It was found that for supports with a typical length of 500 mm, the reflection coefficient was approximately 10 %, and the transmission coefficient was approximately 80 %, with part of the energy of the incident TEM mode being converted into higher-order modes. The low value for the reflection coefficient means that the presence of a large accumulation of water will not be masked by the reflection from the support.

Pipeline conditions in the field will rarely be the ideal conditions found in the laboratory. For example, the cladding may tend towards ovality rather than maintaining a circular cross-section, particularly if the insulation becomes wet, as the additional weight of the water will cause the insulation and cladding to sag underneath the pipeline. It is not expected that this would be a major problem for the technique, as the ducting used in the laboratory also experienced this problem of ovality to some extent, without adversely affecting the performance of the technique. Another deviation from the ideal scenario that is found in the field is that the outer cladding is found to be non-concentric with the inner pipe. Again, this was experienced in the laboratory when using cardboard supports to maintain concentricity; on occasion the cardboard would crumple leading to a lowering of the inner conductor. The SCNR would decrease slightly when this happened, but otherwise the technique maintained its performance and continued to produce meaningful results. Dents are another common feature on cladding in the field, due to the actions of personnel on site. This was not experienced in the laboratory, but it is well documented in the microwave engineering literature that denting a waveguide will affect its impedance

at that point, a fact which was often exploited in order to fine tune an impedance match. Under field conditions it is possible for there to be breaks in the cladding, which would result in electrical discontinuity in the waveguide walls. This would cause a significant reflection of the microwave signal, rendering it impossible to inspect beyond such a feature. This would be beneficial to the technique as such a break in the cladding will invariably lead to water ingress and should be addressed as a matter of urgency; the microwave technique would highlight such areas in need of attention. In order to describe the limitations of the technique in relation to these different operating conditions, further work would be required. Convincing evidence would be obtained if the operation of the technique could be demonstrated in field conditions subject to deviations such as dents, ovality, and non-concentricity.

9.2.4 Implementation of the Guided Microwave Technique

It is envisaged that for the field deployment of this technique the antennas would be fitted to a pipe in the first instance and subsequently left permanently installed for future inspections, an approach facilitated by the fact that the antennas are very simple and inexpensive, and do not make contact with the inner pipe. Permanently installed antennas would have the combined benefits of enabling the intrusions through the cladding to be thoroughly sealed against water ingress to ensure the antenna array position does not become a site of CUI, and would also enable regular monitoring of the pipe, which would allow the use of baseline comparison methods leading to greater sensitivity to the first ingress of water. It is worth noting that this technique provides real-time monitoring of the condition of a pipeline; with no time-consuming signal analysis, data can be collected as often as required.

The laboratory setup employs a quarter-wavelength separation ($\lambda_m/4 = 78$ mm) between the antenna array and the metallic ducting end-cap, to create constructive interference in the desired direction of propagation. Whilst in some circumstances the configuration of the cladding in the field includes a suitable end-cap, typically, no such convenient termination would exist. However, directional discrimination could be achieved through one of two methods: installing a reflective feature in

the pipeline alongside the antenna array; or exciting a second array of antennas positioned proximally to the first with a suitably phased input signal to achieve directionality, as is routinely done with guided ultrasonic testing [12]. In either case, the technique would be capable of inspecting in either direction from the site at which the array is installed, providing significantly increased inspection range.

In order to gauge the range of the guided microwave signals, it is possible to estimate the total attenuation that would be experienced over a certain distance. In Section 5.4, the pulse-echo attenuation coefficients of rockwool and polyurethane foam insulation were determined to be $0.2\,\mathrm{dB\,m^{-1}}$ and $1.2\,\mathrm{dB\,m^{-1}}$, respectively. In Section 8.2 the transmission coefficient of a typical support was found to be approximately 80 %, which equates to an attenuation of 2 dB. With these values it is possible to estimate the attenuation experienced over certain distances, for pipelines with each type of insulation.

For a pipeline with polyurethane foam insulation, there are no pipe supports within the waveguide, therefore the only attenuation is due to the insulation material. Pulse-echo propagation to a distance of 25 m from the inspection location would lead to 30 dB of attenuation due to the insulation material. However, from this inspection location, an additional 25 m can be interrogated by inspecting in the opposite direction, giving an inspection range of 50 m for a total attenuation of 30 dB. To reach a distance of 50 m from the inspection location (equivalent to a total inspection range of 100 m) a total attenuation of 60 dB would be experienced.

For a pipeline with rockwool insulation, it is more difficult to quantify the attenuation because the main contribution to the attenuation is from the pipe supports. The distance between supports is not standardised, but is determined on a case-by-case basis during the design of the plant. However, if we take an example of a support every 10 m, and look at the case of propagating a signal to a distance of 25 m, then there would be two supports in this length, giving rise to 4 dB of attenuation on the outward journey and 4 dB on the return journey. When this is combined with the pulse-echo attenuation coefficient of $0.2\,\mathrm{dB\,m^{-1}}$ for rockwool, then the total attenuation to reach a distance of 25 m (or 50 m of inspection range if both directions are

interrogated) is 13 dB. To inspect a distance 50 m away from the array location, the signal would encounter up to five supports resulting in 20 dB of pulse-echo attenuation due to the supports, and 10 dB due to the rockwool insulation. Therefore, the total attenuation to reach a distance of 50 m, which is equivalent to an inspection range in both directions of 100 m, is 30 dB.

9.3 Future Work

During the course of the development described in this thesis, the operational parameters of this guided microwave technique have been defined. The experimental setup employed for these initial stages of development included a Vector Network Analyser (VNA) to generate the microwave frequency signals and perform the signal analysis. Whilst this hardware is extremely capable, with a very wide frequency range of 10 MHz to 67 GHz, now that the operational parameters of the technique have been defined, alternative hardware could be designed or procured (simplified designs for VNAs have emerged recently [87, 88]), which incorporates only the features and the frequency range that the technique requires to operate, thereby increasing portability and decreasing cost.

Currently, the technique employs a splitter component to obtain the required number of channels to feed the array. Whilst this achieves the objective of pure-mode excitation, it also discards potential information about non-axisymmetric defects in the waveguide. If a multiplexer were used instead of the splitter, then the antennas could be excited sequentially in order to capture this non-axisymmetric information. The effect of simultaneous excitation of all antennas in the array can be recreated by summing the individually excited channels. The additional information from each antenna would allow water volumes to be imaged using synthetic focussing [89].

In the initial stages of the development of this technique a procedure was implemented to perform a calibration procedure at the ends of the cables where they are connected to the antennas, in order to reduce the coherent noise in the signal. This mathematically eliminates reverberations within the feeding cable system and

was a good solution to the problem within the scope of work of this project; however, a more robust and effective technique for future implementation would be to eliminate the physical source of the reverberations within the feeding cable system. The antennas act as a strong reflector at the end of the feeding cables, despite the optimisation of the antenna design to match the impedance of the feeding cables to the waveguide. In order for the microwave energy to reverberate in the feeding cable system, there has to be an additional reflector, and in this case the splitter is the second reflector. The microwave energy reverberates between the antennas and the splitter, contributing to the coherent noise in the signal; referring to Figure 4.5, the four peaks between 0.5 m and 1.5 m are due to the splitter, whilst the noise between 4.5 m and 5.5 m is due to a reverberation from the splitter. By performing some future work into the design of the splitter with the objective of minimising the amount of reflection obtained from this component, the primary physical source of the feeding cable reverberations would be eliminated, leading to an improvement in the signal-to-coherent-noise ratio.

Rather than aiming to inspect exclusively with the TEM mode, there could be value in exciting with other modes, in particular those of the TE_{p1} mode family. In this manner, energy could be focussed to regions of particular concern, such as the 6 o'clock position of the pipe. Although these modes propagate dispersively, there are algorithms that can be implemented to account for and reverse the effects of such dispersion [90]. Future work would be concerned with determining the potential value in exciting alternative modes, and the extent of any enhanced detectability, together with implementing a system to selectively excite modes other than the TEM mode.

Further work needs to be conducted on the design of the antennas. From a practical implementation point of view, the antennas should be able to be installed from the outside of the pipe, rather than requiring access to the insulation layer, as is currently the case. The antenna design is also required to achieve a water-tight seal with the cladding, so that the site of the antenna array does not become a location for water ingress.

One aspect of the technique that is relevant to its future application, but was not possible to investigate on the limited waveguide lengths available in the laboratory, is the inspection length which can be achieved by guided microwaves. Although values for the total attenuation experienced have been estimated, the only practical and accurate method of determining the inspection length would be to install an excitation antenna array on a long length of pipeline in the field, with a second antenna array for reception. By moving the reception array further from the excitation array, the transmission coefficient as a function of pipeline length could be obtained. From this information, the inspection length from a single position could be determined, which would inform the decision as to the recommended intervals between antenna arrays on a pipeline.

As mentioned in Section 6.5, further work is needed to understand the behaviour of water in a real insulated pipeline; in particular, how water diffuses through the insulation to reach the inner pipe, which it must if corrosion is to occur. It is thought that capillary action due to the interface between the cladding and the insulation is responsible for water travelling along the length of the pipeline and occasionally causing corrosion some distance away from the site of water ingress. If this is the case, then it could be expected that water will puddle at some low-point along the pipeline, leading to a localised saturation of the insulation at this point, resulting in a detectable water volume. As these insulations are quite hydrophobic in the short-term it is thought that an additional route through which the water reaches the inner pipe are the joints in between insulation sections. If water exists at the bottom of these joints, then the close proximity of these two surfaces may result in water moving upwards under capillary action to reach the inner pipe; again, this would result in a detectable water volume.

If it is found that wet sections of insulation are very diffuse with long transition regions between wet and dry, then the premise for detecting water by receiving reflections from water volumes will not be sufficiently effective to be implemented on a large scale. However, there are some alternative approaches that could be

used to augment the detecting abilities of the guided microwave system. If a pitch-catch configuration with two sets of antennas is employed, then the amplitude of the signal recorded at the reception antenna array will be very sensitive to the presence of water in between the two arrays, due to the high attenuation of water. In a similar manner, a pulse-echo configuration requires some form of reference reflectors along the interrogated length in order to determine the signal strength, and the loss of the reflections from these references would serve to indicate the presence of attenuative water in the waveguide. It is thought that pipe supports (for rockwool insulation systems) or field-joints (for PUF insulation systems) could act as these reference reflectors, however, the effectiveness of these features as reference reflectors would also require further research.

Appendix A

Optimisation of an Antenna in a Rectangular Waveguide

With several impedance matching techniques discounted due to their inapplicability to this particular problem, and with two techniques demonstrating poor performance in impedance matching over a wide frequency range, the problem of improving the impedance match of the antenna array to the coaxial feeding cables was not easily solved. In the microwave engineering literature, there was some reference to the impedance match being affected by the length and radius of the rod of the antenna. As this would be the ideal solution to the problem, from a practical implementation point of view, this approach was investigated.

As the coaxial waveguide array is a complicated system, involving mutual coupling between individual antennas, the investigation of matching with antenna design focussed initially on the simpler case of a single probe antenna exciting a rectangular waveguide. The experiments employed a rectangular waveguide with dimensions of $w = 95.3\,\text{mm}$ and $h = 44.7\,\text{mm}$. The dimensions of this rectangular waveguide lead to a pure-mode operating frequency range from 1.6 to 3.1 GHz, therefore this was the range that was used in the experiments. The antenna was positioned centrally across the x-axis of the waveguide, and at $\lambda_m/4 = 24.5\,\text{mm}$ from a short-circuiting metal end-plate in the z direction. Two experiments were performed: the first varied

the length of the probe antenna whilst keeping the radius constant at 0.6 mm; the second varied the radius whilst keeping the length constant at 27.3 mm (equivalent to 0.6 of the height of the waveguide), with the performance of the antenna being determined by calculating the IMR for each antenna design. The results can be seen in Figure A.1.

The experiment conducted to vary the length of the antenna produced some very promising results, which are displayed in Figure A.1(a). It was found that varying the length of the antenna had a very significant effect on the IMR, with the maximum and minimum values calculated to be 470 and 0.32, respectively. The optimum length was found to be 0.64 of the waveguide height, equivalent to 28.6 mm. The experiment to vary the radius demonstrated that changing the radius also had an effect on the IMR of the antenna, with the optimum radius determined to be 1.75 mm, achieving an IMR of 0.22. Contrary to the port-matching and triple-stub tuner techniques, this technique of varying the length and diameter of the antenna rods achieves a very good impedance match for a signal with a bandwidth of 1.5 GHz, which is comparable to the bandwidth of 1.9 GHz required by the guided microwave technique. Therefore, this impedance matching technique shows great promise for this application.

In both of the plots in Figure A.1 the experimental data is plotted alongside simulated results. These simulated results were obtained with Microwave Studio, using a model created to reflect the experimental setup. It can be seen that there is excellent agreement between experimental and simulated data in both Figures A.1(a) and (b). This provides validation for the accuracy of the software in simulating the behaviour of antennas radiating within waveguides, which is crucial in the continued use of the software for the development of an antenna array for the excitation of large coaxial waveguides.

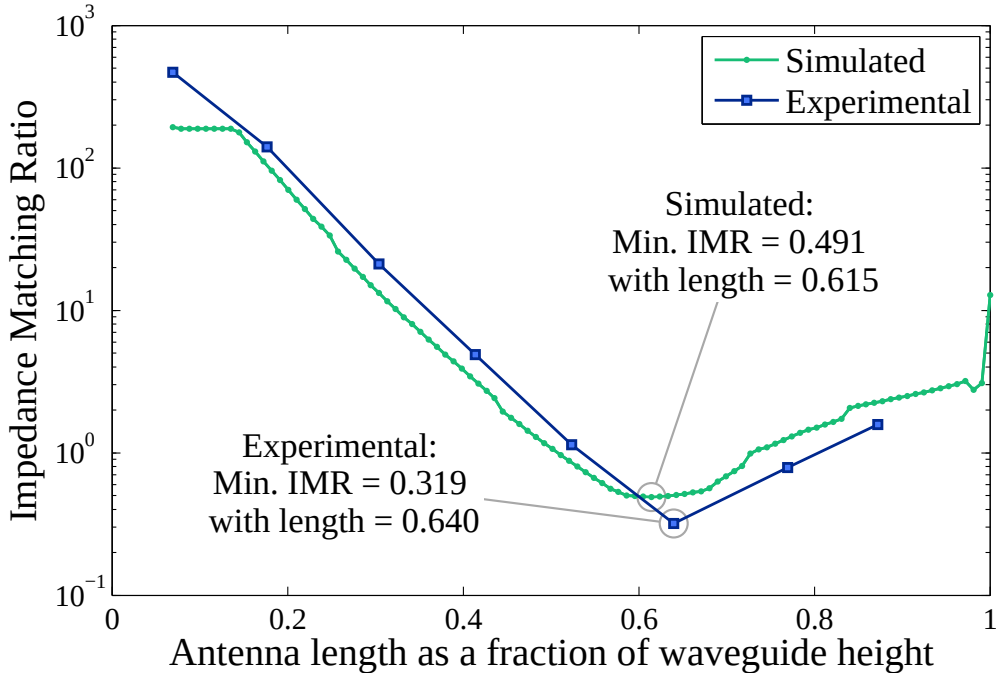

(a) Varying antenna length

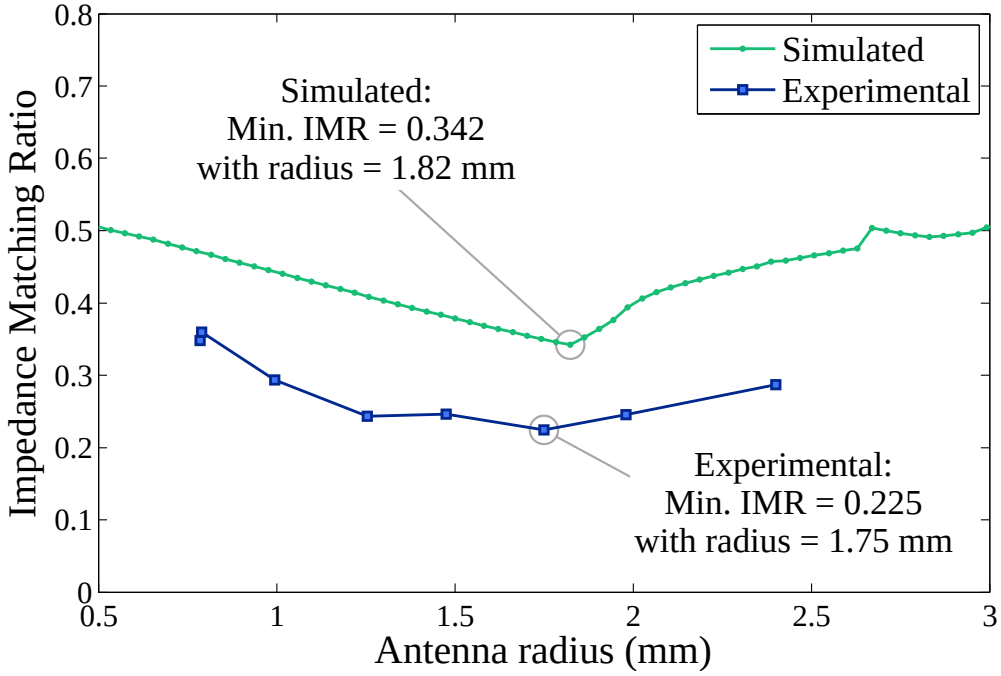

(b) Varying antenna radius

Figure A.1: Results from two experiments conducted using rectangular waveguide, to determine whether the design of the antenna could be used to improve the impedance matching at the junction between a coaxial cable and a waveguide.

Appendix B

Calculation of Dispersion Curves for Modes in Bends

In Section 7.1, the necessity to consider the dispersion characteristics of the guided modes travelling in curved coaxial waveguides was recognised. To this end, a method was devised that would allow Microwave Studio to be used to calculate the data required for plotting the dispersion curves of curved coaxial waveguides. The method was employed initially on straight coaxial waveguides, so that the results could be validated by comparison with the dispersion curves obtained from the analytical solution described in Chapter 3.

A coaxial waveguide with $a = 157.5\,\text{mm}$ and $b = 80\,\text{mm}$ was created in Microwave Studio, with ports 1 and 2 defined on the two ends of the waveguide. In order to record the data required for plotting the dispersion curves, a set of probes was created to record the x component of the electric field at a point halfway between the inner and outer conductors, along the entire length of the waveguide. The simulation was performed with an excitation signal spanning a frequency range from 0 to 1.9 GHz applied to port 1.

The time signals recorded at the electric field probes were output from the simulation software and used to produce a two dimensional data set of amplitude as a function of time and distance around the toroid. By taking the two dimensional Fast Fourier

Transform (2D FFT) of this data set, the time-domain becomes the frequency-domain and the spatial dimension becomes the wavenumber, k. The resultant data matrix can then be imaged to produce a plot of frequency against wavenumber, with the colour-scale corresponding to the amplitude. The image in Figure B.1(a) displays these frequency-wavenumber dispersion curves for the straight coaxial waveguide with the following modes excited: TEM, TE_{11}, TE_{21}, TE_{31}, and TE_{41}. By tracing the modal lines in this figure, the wavenumber as a function of frequency can be extracted from the image and used to plot the dispersion curves. This data is plotted in Figure B.2 as the blue circles. The analytical solution is displayed as the blue lines. It can be seen that there is excellent agreement between the two data sets, providing validation for this method of calculating the dispersion curves of modes. If the TEM mode alone is excited, in the straight coaxial waveguide, then the resultant frequency-wavenumber image lacks the lines corresponding to these higher order modes, as shown in Figure B.1(b).

Having validated this method of calculating dispersion curves, it was applied to curved coaxial waveguides. A coaxial waveguide with $a = 157.5\,\text{mm}$ and $b = 80\,\text{mm}$ was curved to form a toroid, with the radius of curvature of the toroid parameterised as R. The angular extent of the toroid was 270° with ports 1 and 2 defined on the two ends of the toroid. The electric field probes were positioned halfway between the inner and outer conductors, all the way around the torus. The excitation signal was applied only to the TEM mode. The resultant frequency-wavenumber dispersion curves are displayed in Figure B.1(c). As the TEM mode propagates around the torus, mode conversion transfers energy from the TEM mode into higher order modes, this is the reason why the high order modal lines are visible in the image, despite the fact that only the TEM mode was excited.

The technique was used successfully to plot the dispersion curves for large bend radii, but whilst employing it on curves with small bend radii a problem was encountered involving the resolution of the images along the wavenumber axis. To be able to accurately trace the modal lines, it is important to achieve high resolution along the frequency and wavenumber axes. The former increases with the length

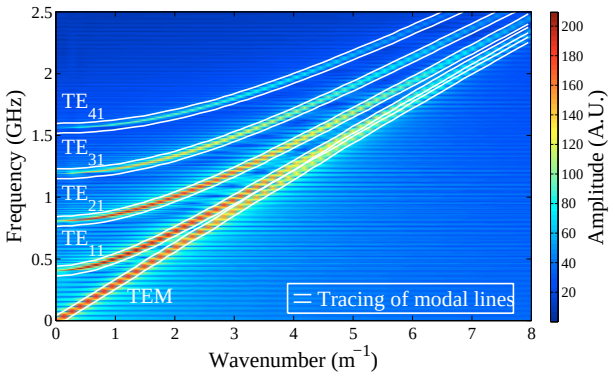

(a) Straight coaxial waveguide, exciting TEM, TE_{11}, TE_{21}, TE_{31}, and TE_{41}

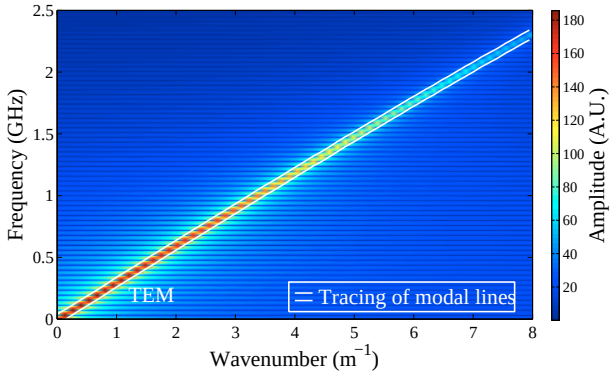

(b) Straight coaxial waveguide, exciting TEM mode only

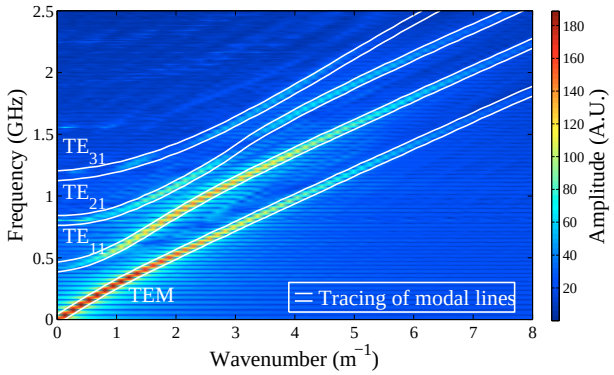

(c) Bent coaxial waveguide with a 1D bend radius, exciting TEM mode only

Figure B.1: Modal components propagating inside the bend. The frequency-wavenumber dispersion curves are obtained by measuring the total electric field along the bend length and performing a 2-D Fourier transform in time and space. The curves refer to a sharp 1D bend and the gray scale provides an indication of the modal amplitude. Only the TEM mode was excited; the presence of three additional modes indicates that there are multiple modes propagating in a coaxial toroid.

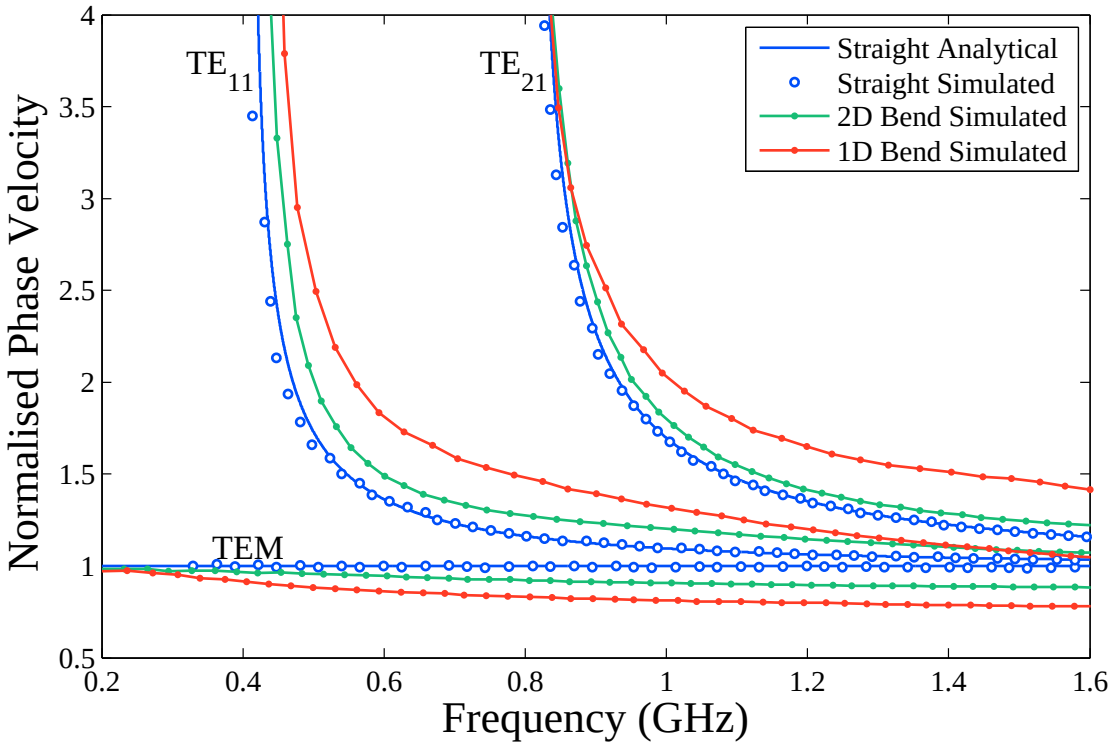

Figure B.2: Effect of the bend radius on the dispersion characteristics of the modes propagating in a coaxial toroid with inner and outer radii 80 mm and 157.5 mm, respectively.

of the temporal window of the signals; thus maximising the frequency resolution is easily achieved. However, the wavenumber resolution depends on the length of the model (the distance from the first probe to the last). With large bend radii, this length is large enough to achieve sufficient wavenumber resolution; however, for small bend radii, which are particularly interesting, the length is insufficient for adequate wavenumber resolution. A solution to this problem, which was successfully implemented, was to extract the time signals of all the propagating modes where they are output at port 2, and use these to form the excitation signals for the various modes at port 1 in a second simulation, thereby doubling the length of the model. For a torus with a 1D bend radius, performing the simulation a total of five times provides a total length which is sufficient for wavenumber resolution. The results of this 1D bend simulation are those that are displayed in Figure B.1(c), with the corresponding phase velocity dispersion curves plotted in red in Figure B.2. The dispersion curves for a 2D bend are also plotted in Figure B.2 in green.

References

[1] E. Bluemink. High-pressure BP gas line blows at Prudhoe Bay field. Online: http://www.adn.com/2008/10/03/544567/high-pressure-bp-gas-line-blows.html, [accessed 13 July 2011], October.

[2] H. Alford. The spill in the Gulf may be over but Congress must tackle BP's terrible safety record next. Online: http://www.foxnews.com/opinion/2010/08/20/harry-alford-bp-gulf-spill-disaster-thunder-horse-texas-prudhoe-bay, [accessed 13 July 2011], August 2010.

[3] Prudhoe Bay pipeline explosion (images). Online: http://www.adn.com/2009/02/24/v-gallery2/701489/prudhoe-bay-pipeline-explosion.html, [accessed 13 July 2011], October 2008.

[4] L. Garverick, editor. *Corrosion in the Petrochemical Industry*. ASM International, 1994.

[5] S. Winnik. *Corrosion-under-insulation (CUI) guidelines*. Woodhead, 2008.

[6] F. De Vogelaere. Corrosion under insulation. *Process Safety Progress*, 28(1):30–35, March 2009.

[7] D. McNaughtan and M. Najami. Practical considerations for effective corrosion under insulation (CUI) management from a North Sea perspective. In *Corrosion 2009 Conference & Expo*, number 09135. NACE, 2009.

[8] T. H. Erickson, L. C. Dash, J. J. Murali, and C. R. Ayers. Predicting the progression of wetness and corrosion under insulation damage in aboveground pipelines. In *Corrosion 2010 Conference & Expo*, number 10373. NACE, 2010.

[9] R. Heidersbach. *Metallurgy and Corrosion Control in Oil and Gas Production*. Wiley, 2011.

[10] M. Twomey. Inspection techniques for detecting corrosion under insulation. *Materials Evaluation*, 55(2):129–132, February 1997.

[11] D. Fruge and K. Bishop. Corrosion under insulation. In *2008 AIChE Spring National Meeting*. AIChE, April 2008.

[12] D. N. Alleyne, B. Pavlakovic, M. J. S. Lowe, and P. Cawley. Rapid long range inspection of chemical plant pipework using guided waves. *Insight*, 43(2):93–96, February 2001.

[13] P. Mudge. Field application of the Teletest long range ultrasonic testing techniques. *Insight*, 43(2):74–77, February 2001.

[14] M.J.S. Lowe and P. Cawley. Long range guided wave inspection usage – current commercial capabilities and research directions. Online: http://www3.imperial.ac.uk/nde/publications, [accessed 28 June 2011], March 2006.

[15] K. Mubarak, K. J. Bois, and R. Zoughi. A simple, robust, and on-site microwave technique for determining water-to-cement ratio (w/c) of fresh portland cement-based materials. *IEEE Transactions on Instrumentation and Measurement*, 50(5):1255–1263, October 2001.

[16] K. J. Bois, A. D. Benally, P. S. Nowak, and R. Zoughi. Cure-state monitoring and water-to-cement ratio determination of fresh portland cement-based materials using near-field microwave techniques. *IEEE Transactions on Instrumentation and Measurement*, 47(3):628–637, June 1998.

[17] K. J. Bois, A. D. Benally, and R. Zoughi. Near-field microwave non-invasive determination of NaCl in mortar. *IEE Proceedings Science, Measurement and Technology*, 148(4):178–182, July 2001.

[18] U. C. Hasar. A microcontroller-based microwave measurement system for permittivity determination of fresh cement-based materials. In *Instrumentation*

and Measurement Technology Conference Proceedings, pages 1–6. IEEE, March 2007.

[19] H. M. A. Al-Mattarneh, D. K. Ghodgaonkar, and W. M. B. W. A. Majid. Determination of compressive strength of concrete using freespace reflection measurements in the frequency range of 8-12.5 GHz. In *Asia-Pacific Microwave Conference Proceedings*, pages 679–682. APMC, 2001.

[20] S. N. Kharkovsky, M. F. Akay, and U. C. Hasar C. D. Atis. Measurement and monitoring of microwave reflection and transmission properties of cement-based specimens. *IEEE Transactions on Instrumentation and Measurement*, 51(6):1210–1218, December 2002.

[21] C. Yeh and R. Zoughi. A novel microwave method for detection of long surface cracks in metals. *IEEE Transactions on Instrumentation and Measurement*, 43(5):719–725, December 1994.

[22] N. Qaddoumi, S. Ganchev, and R. Zoughi. A novel microwave fatigue crack detection technique using an open-ended coaxial line. In *Conference on Precision Electromagnetic Measurements*, pages 59–60. CPEM, 1994.

[23] M. Saka, Y. Ju, D. Luo, and H. Abé. A method for nondestructive evaluation of crack depth on metal surface by microwaves. In *25th International Conference on Infrared and Millimeter Waves*, pages 423–424. IRMMW, 2000.

[24] R. J. Hruby and L. Feinstein. A novel nondestructive, noncontacting method of measuring the depth of thin slits and cracks in metals. *Review of Scientific Instruments*, 41(5):679–683, May 1970.

[25] S. N. Kharkovsky, M. F. Akay, and U. C. Hasar C. D. Atis. A linear sampling approach to crack detection in microwave imaging. In *IEEE International Workshop on Imaging*, pages 222–226. IEEE, 2008.

[26] R. Zoughi and S. Bakhtiari. Microwave nondestructive detection and evaluation of disbonding and delamination in layered-dielectric-slabs. *IEEE Transactions on Instrumentation and Measurement*, 39(6):1059–1063, December 1990.

[27] S. I. Ganchev, N. Qaddoumi, E. Ranu, and R. Zoughi. Microwave detection optimization of disbond in layered dielectrics with varying thickness. *IEEE Transactions on Instrumentation and Measurement*, 44(2):326–328, April 1995.

[28] M. Abou-Khousa and R. Zoughi. Disbond thickness evaluation employing multiple-frequency near-field microwave measurements. *IEEE Transactions on Instrumentation and Measurement*, 56(4):1107–1113, August 2007.

[29] S. Reyes-Rodríguez, N. Lei, R. J. McGough, S. Udpa, and L. Udpa. Application of time reversal signal processing to microwave NDE. In *IEEE International Symposium on Signal Processing and Information Technology*, pages 225–229. IEEE, 2009.

[30] N. Qaddoumi, M. Abou-Khousa, and W. M. Saleh. Near-field microwave imaging utilizing tapered rectangular waveguides. *IEEE Transactions on Instrumentation and Measurement*, 55(5):1752–1756, October 2006.

[31] Microwave monitoring for corrosion under insulation (CUI). BP University Meeting, Stapleford Park, March 2007.

[32] J. D. Jackson. *Classical Electrodynamics*. Wiley, 3rd edition, 1999.

[33] R. A. Waldron. *Theory of Guided Electromagnetic Waves*. Van Nostrand-Reinhold, 1970.

[34] E. H. Grant, T. J. Buchanan, and H. F. Cook. Dielectric behavior of water at microwave frequencies. *Journal of Chemical Physics*, 26(1):156–161, January 1957.

[35] D. M. Pozar. *Microwave Engineering*. Wiley, 3rd edition, 2004.

[36] G. D. Burnett and C. A. Frost. Systems and methods for nondestructively testing conductive members employing electromagnetic back scattering, November 2004. International Patent - World Intellectual Property Organization (WO 2004/102056 A2).

[37] G. D. Burnett and C. A. Frost. Systems and methods for testing conductive members employing electromagnetic back scattering, May 2007. International Patent - World Intellectual Property Organization (WO 2007/062221 A2).

[38] J. M. Galbraith. A new inspection technology for detecting corrosion under insulation. In *Corrosion 2000 Conference & Expo*, number 00101. NACE, 2000.

[39] S. Ramo. *Fields and Waves in Communication Electronics*. Wiley, 1994.

[40] H. J. Reich. *Microwave Theory and Techniques*. Van Nostrand, 1953.

[41] N. Marcuvitz. *Waveguide Handbook*. Peregrinus on behalf of The Institution of Electrical Engineers, 1986.

[42] C. S. Lee, S. W. Lee, and S. L. Chuang. Plot of modal field distribution in rectangular and circular waveguides. *IEEE Transactions on Microwave Theory and Techniques*, 33(3):271–274, March 1985.

[43] R. Collin. *Field Theory of Guided Waves*. IEEE Press, 1991.

[44] T. Weiland. A discretization method for the solution of Maxwell's equations for six-component fields. *International Journal of Electronics and Communications (AEÜ)*, 31(3):116–120, 1977.

[45] Computer Simulation Technology, CST, Bad Nauheimer Str. 19, 64289 Darmstadt, Germany. *CST Microwave Studio Electromagnetic Simulator*, 2011. Online: http://www.cst.com, [accessed 9 February 2011].

[46] M. Clemens and T. Weiland. Discrete electromagnetism with the finite integration technique. *Progress in Electromagnetics Research*, 32:65–87, 2001.

[47] R. Marklein. The finite integration technique as general tool to compute acoustic, electromagnetic, elastodynamic, and coupled wave fields. In W. R. Stone, editor, *Review of Radio Science: 1999-2002*, pages 201–244. IEEE Press, Piscataway, 2002.

[48] G. H. Bryant. *Principles of Microwave Measurements*. Peter Peregrinus Ltd. on behalf of the Institution of Electrical Engineers, 1993.

[49] M. Borsero, G. Vizio, D. Parena, and V. Teppati. Synthetic TDR measurements for TEM and GTEM cell characterization. *IEEE Transactions on Instrumentation and Measurement*, 56(2):271–274, April 2007.

[50] S. Lucyszyn. RFIC and MMIC measurement techniques. In R. J. Collier, editor, *Microwave Measurements*, chapter 11, pages 217–262. Institution of Engineering and Technology, 2007.

[51] M. E Hines and H. E. Stinehelfer. Time-domain oscillographic microwave network analysis using frequency-domain data. *IEEE Transactions on Microwave Theory and Techniques*, 22(3):276–282, March 1974.

[52] G. W. C. Kaye and T. H. Laby. *Tables of Physical and Chemical Constants*. Longman, 16$^{\text{th}}$ edition, 1995.

[53] B. P. Iliev and G. C. M. Meijer. An impedance-measurement system for electrical characterization of rockwool substrates. In *Sensors for Industry Conference*. The Instrumentation, Systems and Automation Society (ISA) and the IEEE Instrumentation and Measurement Society, 2004.

[54] S. B. Bibikov, O. N. Smolnikova, S. B. Menshova, M. V. Prokof'ev, and V. V. Orlov. Some approaches to the development of absorbing materials for ultrawideband systems. In *5th International Conference on Ultrawideband and Ultrashort Impulse Signals (UWBUSIS)*, pages 262–265, 2010.

[55] O. M. Nofal and A. M. Zihlif. Dielectric and ac conductivity of rockwool fibers-polystyrene composites. *Journal of Reinforced Plastics and Composites*, 29(17):2636–2646, 2010.

[56] Electrolube. Ur5528 polyurethane resin technical data sheet. Online: http://www.electrolube.com/products/tds/UR5528.pdf, [accessed 10 June 2012], 2012. Electrolube, Ashby Park, Coalfield Way, Ashby de la Zouch, Leicestershire, LE65 1JF.

[57] R. E. Jones, F. Simonetti, M. J. S. Lowe, and I. P. Bradley. Use of microwaves for the detection of water as a cause of corrosion under insulation. *Journal of Nondestructive Evaluation*, 2011.

[58] M. J. S. Lowe, D. N. Alleyne, and P. Cawley. Defect detection in pipes using guided waves. *Ultrasonics*, 36:147–154, 1998.

[59] A. Demma, P. Cawley, M. Lowe, A. G. Roosenbrand, and B. Pavlakovic. The reflection of guided waves from notches in pipes: a guide for interpreting corrosion measurements. *NDT&E International*, 37:167–180, 2004.

[60] C. A. Balanis. *Advanced Engineering Electromagnetics*. Wiley, 1989.

[61] K. R. Demarest. *Engineering Electromagnetics*. Prentice Hall, 1998.

[62] S. R. Pennock and P. R. Shepherd. *Microwave Engineering with Wireless Applications*. McGraw-Hill, 1998.

[63] R. Collin. *Foundations for Microwave Engineering*. IEEE Press, 2001.

[64] Agilent Technologies. *Agilent PNA Series Network Analyzer Manual*, 2010.

[65] Agilent Technologies. *Agilent De-embedding and Embedding S-Parameter Networks Using a Vector Network Analyzer*, 2004. Application Note 1364-1.

[66] E. K. Yung, Z. M. Xie, and R. S. Chen. Input impedance of a coaxial-line fed probe in a thick coaxial-line waveguide. *IEE Transactions on Microwave Theory and Techniques*, 48(10):1707–1711, 2000.

[67] J. G. Davis and A. A. P. Gibson. Input impedance of an overmoded coaxial line fed coaxial waveguide. *IEE Microwave and Wireless Components Letters*, 15(10):658–660, 2005.

[68] B. Krietenstein, R. Schuhmann, P. Thoma, and T. Weiland. The perfect boundary approximation technique facing the challenge of high precision field computation. In *Proc. of the XIX International Linear Accelerator Conference (LINAC '98), Chicago, USA*, 1998.

[69] R. B. Keam and A. G. Williamson. Analysis of coaxial-line/rectangular waveguide junction with dielectrically sheathed probe. *Electronics Letters*, 28(3):240–241, 1992.

[70] R. B. Keam and A. G. Williamson. Analysis and design of coaxial-line/rectangular waveguide junction with a dielectrically sheathed centre probe. *Asia-Pacific Microwave Conference, Adelaide*, 38(4):845–848, 1992.

[71] R. Hooke and T. A. Jeeves. 'Direct search' solution of numerical and statistical problems. *Journal of the Association for Computing Machinery (ACM)*, 8(2):212–229, 1961.

[72] Lindab. Online: http://www.lindab.co.uk, [accessed 16 February 2011], 2010. Unit J5 Lower Road, Northfleet Industrial Estate, Northfleet, Kent DA11 9BL, UK.

[73] Rockwool Limited. Online: http://www.rockwool.co.uk, [accessed 2 March 2011], 2011. Pencoed, Bridgend, CF35 6NY, UK.

[74] PAR Group. Online: http://www.par-group.co.uk, [accessed 2 March 2011], 2011. Bridge House, Chorley North Industrial Park, Drumhead Road, Chorley, Lancashire, PR6 7BX, UK.

[75] BPXA Site Technical Practice. *Specification for Preformed Insulation*, 2010. SPC-AK-52-103.

[76] Trident Foams Limited. Online: http://www.tridentfoams.co.uk, [accessed 2 March 2011], 2011. BKB House, Goyt Valley Industrial Estate, Furness Vale, High Peak, SK23 7SN, UK.

[77] Foamglas. Physical and thermal properties of Foamglas One insulation. Online: http://www.foamglas.com/industry/en/products_product_information/technical_data_foamglas_one, [accessed 2 March 2011], 2011. Pittsburgh Corning Europe, Albertkade 1, 3980 Tessenderlo, Belgium.

[78] K. S. Cole and R. H. Cole. Dispersion and absorption in dielectrics I. alternating current characteristics. *Journal of Chemical Physics*, 9(4):341–351, 1941.

[79] P. Debye. *Polar Molecules*. Dover, 1929.

[80] F. Yu and P. B. Nagy. Simple analytical approximations for eddy current profiling of the near-surface residual stress in shot-peened metals. *Journal of Applied Physics*, 96(2):1257–1266, 2004.

[81] M. Jouguet. Effects of the curvature on the propagation of electromagnetic waves in guides of circular cross-section. *Cables et Transmission*, 1(2):133–153, 1947.

[82] S. E. Miller. Notes on methods of transmitting the circular electric wave around bends. *Proceedings of the IRE*, 40(9):1104–1113, 1952.

[83] S. E. Miller and A. C. Beck. Low-loss waveguide transmission. *Proceedings of the IRE*, 41(3):348–358, 1953.

[84] W. J. Albersheim. Propagation of TE_{01} waves in curved waveguides. *Bell System Technical Journal*, 28(1):1–32, 1949.

[85] H. E. M. Barlow. Propagation of the circular H_{01} low-loss wave mode around bends in tubular metal waveguide. *Proceedings of the IEE - Part B: Radio and Electronic Engineering*, 104(16):403–409, 1957.

[86] G. D. Sims. The influence of bends and ellipticity on the attenuation and propagation characteristics of the H_{01} circular waveguide mode. *Proceedings of the IEE - Part III: Radio and Communication Engineering*, 100(64):115–116, 1953.

[87] M. A. Abou-Khousa, M. A. Baumgartner, S. Kharkovsky, and R. Zoughi. Novel and simple high-frequency single-port vector network analyzer. *IEEE Transactions on Instrumentation and Measurement*, 59(3):534–542, March 2010.

[88] M. A. Abou-Khousa, M. A. Baumgartner, S. Kharkovsky, and R. Zoughi. Ka-band vector reflectometer based on simple phase-shifter design. *IEEE Transactions on Instrumentation and Measurement*, 60(2):618–624, February 2011.

[89] J. Davies and P. Cawley. The application of synthetic focusing for imaging crack-like defects in pipelines using guided waves. *IEEE Transactions on Ultrasonics, Ferroelectrics, and Frequency Control*, 56(4):759–771, April 2009.

[90] P. Wilcox. A rapid signal processing technique to remove the effect of dispersion from guided wave signals. *IEEE Transactions on Ultrasonics, Ferroelectrics, and Frequency Control*, 50(4):419–427, April 2003.

List of Publications

[P1] R. E. Jones, F. Simonetti, M. J. S. Lowe, and I. P. Bradley, "Use of Microwaves for the Detection of Corrosion Under Insulation", in *29th Review of Progress in Quantitative Nondestructive Evaluation*, Kingston, Rhode Island. Volume 29B, Pages: 1378-1380, Edited by D. Chimenti, D. Thompson, 2010.

[P2] R. E. Jones, F. Simonetti, M. J. S. Lowe, and I. P. Bradley, "Use of Microwaves for the Detection of Corrosion Under Insulation: A Sensitivity Study", in *30th Review of Progress in Quantitative Nondestructive Evaluation*, San Diego, California. Volume 30B, Pages: 1714-1721, Edited by D. Chimenti, D. Thompson, 2011.

[P3] R. E. Jones, F. Simonetti, M. J. S. Lowe, and I. P. Bradley, "Use of Microwaves for the Detection of Corrosion Under Insulation: The Effect of Bends", in *31st Review of Progress in Quantitative Nondestructive Evaluation*, Burlington, Vermont, 2012. Volume 31B, Pages: 1665-1672, Edited by D. Chimenti, D. Thompson, 2012.

[P4] R. E. Jones, F. Simonetti, M. J. S. Lowe, and I. P. Bradley, "Use of Microwaves for the Detection of Water as a Cause of Corrosion Under Insulation," *Journal of Nondestructive Evaluation*, Volume 31, Number 1, Pages: 65-76, DOI: 10.1007/s10921-011-0121-9, 2012.

[P5] R. E. Jones, F. Simonetti, M. J. S. Lowe, and I. P. Bradley, "The Effect of Bends on the Long-Range Microwave Inspection of Thermally Insulated Pipelines for the Detection of Water," *Journal of Nondestructive Evaluation*, Volume 31, Number 2, Pages: 117-127, DOI: 10.1007/s10921-011-0127-3, 2012.

[P6] R. E. Jones, F. Simonetti, M. J. S. Lowe, and I. P. Bradley, "Guided Microwave Inspection Technology: From the Lab to the Field," *Insight*, To be submitted.